VISUALIZING CROSS-COUPLED ORDERS IN MULTIFERROIC HEXAGONAL MANGANITES WITH SCANNING FORCE MICROSCOPIES

By

YANAN GENG

A dissertation submitted to the

Graduate School—New Brunswick

Rutgers, The State University of New Jersey

in partial fulfillment of the requirements

for the degree of

Doctor of Philosophy

Graduate Program in Department of Physics and Astronomy

written under the direction of

Weida Wu

and approved by

_____

_____

_____

_____

_____

New Brunswick, New Jersey

January, 2015

ABSTRACT OF THE DISSERTATION

Visualizing cross-coupled orders in multiferroic hexagonal manganites with scanning force microscopies

By YANAN GENG

Dissertation Director:

Weida Wu

This thesis covers the study of multiferroics and magnetoelectrics by utilizing a collection of scanning force microscopy to investigate the cross-coupled phenomena. We mainly focus on the multiferroic hexagonal REMnO$_3$ (RE = rare earth), an improper ferroelectrics with the coexistence of ferroelectricity (T_C = 1200 - 1500 K) and antiferromagnetism (T_N = 70 - 120 K), and explore in depth the magnetoelectric effect of this system microscopically. Using cryogenic magnetic force microscope (MFM), we observed uncompensated magnetic moment along antiferromagnetic domain walls, which coincides with the ferroelectric domain boundaries. This magnetism presents an alternating feature around the multiferroic vortex, and correlates with each other through the vortex network. The study of the magnetic field dependence of domain wall magnetism also provides a way to probe the intrinsic bulk domain state.

To directly image the magnetoelectric domains, we developed a novel mesoscopic technique, namely, magnetoelectric force microscopy (MeFM), to probe the local electric field-induced magnetization based on MFM. The detail of the novel technique will be presented

in Chapter 2. With the application of MeFM in hexagonal manganities, we observed that the magnetoelectric response changes sign at each structural domain wall, which provides compelling evidence for a lattice-mediated magnetoelectric coupling. More interestingly, the magnetoelectric effect diverges when approaching the tri-critical point in $T - H$ phase diagram, where critical fluctuation plays a crucial role. Our study suggests the phase competition as a possibility to enhance magnetoelectric coupling. The systematic study of hexagonal manganites, including $ErMnO_3$ and $YbMnO_3$, disentangles the contribution from Mn and rare earth sublattices, suggesting that the $3d - 4f$ coupling and the Ising anisotropy of rare earth spins are the key ingredients to understand the re-entrant spin-reorientation phase boundary and the emergence of a tri-critical point.

Acknowledgments

My impression for Rutgers is distant at first, like a maid in the mist. Time marches on, and so is my affection for it. For whatever life I am going to sail to, Rutgers is always my second home, for every piece of knowledge I have grasped and every drop of memory I have collected in here.

My special thanks goes to my advisor, Prof. Weida Wu. His enthusiasm and curiosity for physics has been inspiring me all the time. He has instructed me generously and patiently to be a qualified physicist from every aspect. His dedication and diligence will always be the lighthouse of my career.

I would like to thank my thesis committee, Sang-Wook Cheong, Piers Coleman, Ronald Ransome, Mohan Kalelkar. Their advices and comments guided me through my research towards this thesis. I benefitted from the discussions with David Vanderbilt, Karin Rabe, Premala Chandra, Valery Kiryukhin, Yochi Horibe, Girsh Blumberg, Seongshik Oh, Michael Gershenson, Yuanzhen Chen, Sergey Artyukhin and Tzen Ong.

It is a very pleasant experience to cooperate with Craig J. Fennie of Cornell, Maxim Mostovoy of Zernike and J. W. Freeland of Argonne. I enjoyed the internship in Yi-Qiao Song's group in Schlumberger. Without the help and constant supply of high-quality samples from Sang's group, my work has not been possible. I would like to thank his group members: Xueyun Wang, Nara Lee, Bin Gao, Feiting Huang, Fei Fan, Younghun Jo, Y-oungJai Choi, Seung Chul Chae, Hee Taek Yi, Rongwei Hu, Yoon Seok Oh.

I am very grateful to the folks in our SPM lab: Jixia Dai, Soonyong Park, Quantong Shen, Wenbo Wang, Jing Chen, Wenhan Zhang, Edward Lochocki, Tomer Nawrocki. Their accompanies delight my research life. With them and other poker-card fellows: Jianpeng

Liu, Huijie Guan, Yue Liu, Yazhong Wang, Yi Zhang, Yue Zhao, it is an amazing experience to dig up gourmet in NYC.

I appreciate the continuous service provided by "LoudClear". Over six years, I only visited my parents and sister for three times, and 21,900 minutes international calls have been dialed. I thank it for not bankrupting and not rising in price.

Finally, it's my great fortune to meet my wife Qing at Rutgers. I admire her as a talented singer, a pianist, a calligrapher and a chemist.

Dedication

This thesis is dedicated to my parents.

For their endless love, support and encouragement.

Table of Contents

List of Figures

x

Chapter 1

Introduction

1.1 Multiferroics

The coupling between magnetic and electric phenomena, microscopically, has a long-lasting history. As described by the Maxwell's equations, the changing electric field generates magnetic field, and vice versa [1]. Macroscopically, the presence of multiple ferroic orders in a single-phase material is called multiferroics. For instance, the most common multiferroics possess magnetism and ferroelectricity simultaneously. The coexistence of multi-ferroic orders may result in strong cross coupling, as described in Fig. 1.1, which can be harnessed in various modern technologies [2, 3, 4, 5, 6]. The potential of manipulating magnetization with electric field, or controlling electric polarization with magnetic field, is promising for high sensitivity AC magnetic sensors, and electrically tunable microwave devices, like filters and oscillators. This mutual control between magnetic and electric orders results in emergent degree of freedom that is useful for material design and spintronics industry.

The search for multiferroics can be traced back to the pioneering studies in 1950s, though there was less success in terms of coexistence of ferromagnetism and ferroelectricity, as these two order parameters turned out to be mutually exclusively [7, 8]. One way to understand the exclusivity is that most ferroelectricity prefers empty d-orbital, while ferromagnetism requires it partially-filled (otherwise spins add to zero). In the compound $BiFeO_3$, the only known existing system with antiferromagnetism and ferroelectricity at room temperature, it is the Bi ion with lone pair ($6s$-orbital) that leads to spontaneous electric polarization, while the magnetism originates from the Fe site [9]. However, the magnetoelectric coupling
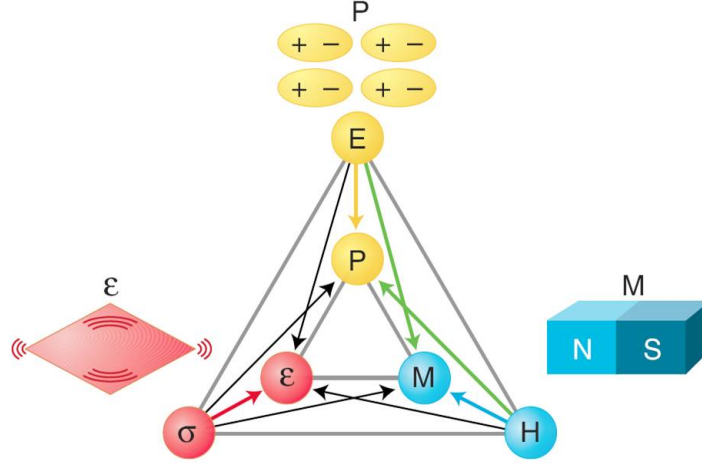
Figure 1.1: The electric polarization P, magnetization M, and strain ε are controlled by their conjugate fields electric field E, magnetic field H, and stress σ, respectively. In multiferroics, cross-coupling may be present, e.g., P (M) can be controlled by H (E). [5]

is relatively weak [9, 2]. Therefore, the concept of multiferroics has later been generalized to any magnetic and electric orders, and attention has been diverted to mechanism of strong coupling rather than the presence of the two ferroic orders. For the last twenty years, there has been a resurgence of interest in this field, which is driven by the development of advanced theoretical and experimental techniques [10, 11, 12, 7].

Depending on the mechanism of inversion symmetry breaking, there are proper and improper ferroelectrics. In proper ferroelectrics, like $BaTiO_3$, $BiFeO_3$, and $Pb(Fe_{2/3}W_{1/3})O_3$, the polar instability is the main driving force of the transition [2]. On the contrary, the polarization is only the by-product of some other ordering (i.e., magnetic transition) in improper ones. For instance, in the orthorhombic rare-earth manganites $TbMnO_3$ and $TbMn_2O_5$, the onset of ferroelectricity clearly correlates with the appearance of spiral magnetic ordering [13, 14, 15]. Generally, improper ferroelectrics show complex magnetic structures and phase diagrams.

1.2   Linear Magnetoelectric Effect

The linear magnetoelectric (ME) effect, initially discussed by Landau and Lifshits [16], is characterized as the induction of a magnetization by electric field, or that of an electric polarization by magnetic field [17]. The coupling coefficient is often described as a second rank tensor α. For instance, α_{zz} denotes the z-direction response by applying the stimulus along the same orientation. The linear ME effect has potentially technological impacts on memory devices, high sensitivity sensors, and spin valve effects [2, 6, 4]. The measurement of the components of α tensor is also crucial for fundamental science, e.g., for determining the magnetic point groups.

1.2.1   Magnetic Symmetries
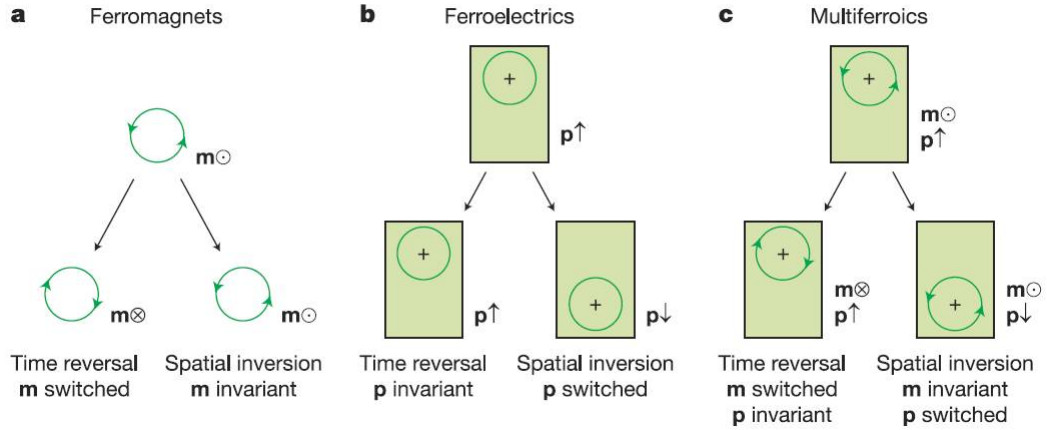
Figure 1.2: The responses under time reversal and spatial inversion operations for ferromagnet (**a**), ferroelectrics (**b**), and multiferroics (**c**). [3]

Intensive studies have been focused on the linear ME effect ever since the seminal work on Cr_2O_3 done by Dzyaloshinskii and Astrov [18, 19, 20]. Phenomenologically, the linear ME response originates from the lowest order bilinear term in the Landau free energy expansion:

$$F = F_0 - \frac{1}{2}\varepsilon_{ij}E_iE_j - \frac{1}{2}\chi_{ij}H_iH_j - \alpha_{ij}E_iH_j \tag{1.1}$$

Taking the partial derivative of free energy F with respect to E_i, and keeping only the cross

Figure 1.3: Table of 18 possible tensor forms of the linear ME effect. [17]

term, we obtained:

$$P_i = -\frac{\partial F}{\partial E_i} = \alpha_{ij} H_j \qquad (1.2)$$

From the point view of symmetry consideration, magnetic spins reverse sign under time reversal operation and remain invariant under spatial inversion symmetry. On the contrary, electric polarizations need the broken spatial inversion symmetry while the time symmetry can be invariant. Therefore, the linear ME tensor α_{ME} has to break time reversal and spatial inversion symmetries simultaneously [3], as shown in Fig. 1.2. Moreover, magnetic point groups admit the physical properties of the system, suggesting the crystal to possess certain magnetic point groups with broken time and space symmetries to have non-zero α. This leaves us only 58 magnetic point groups allowing the linear ME α, summarized in Fig. 1.3 [21, 22, 23]. Although this table doesn't provide information in terms of the ME amplitude, symmetry analysis is a powerful tool to place constrains on linear ME effect based on its magnetic structures. For example, Cr_2O_3, the prototype linear ME material,

belong to the magnetic point group $\bar{3}'m'$, which falls into the category #14 in Fig. 1.3. Astrov measured the linear ME effect in Cr_2O_3, and found that $\alpha_{xx} = \alpha_{yy} \neq \alpha_{zz}$, which agrees with the symmetry consideration [19].

1.2.2   Measurements of linear ME effect

Linear ME response is a secondary effect compared with magnetic and electric susceptibilities, and occurs mostly at low temperatures. The elements of the tensor α in single-phase crystals are thermodynamically limited by

$$\alpha_{ij} < 4\pi\sqrt{\xi_{ii}\chi_{jj}} \tag{1.3}$$

though it is far from reaching this limit in most of the situations [24, 25]. For instance, the maximum linear ME response in Cr_2O_3 is only ≈ 4 ps/m at 263 K [23], corresponding to 0.4 Oe magnetic field induced by applying 100 kV/cm electric field. Therefore, it's a technical challenge to directly measure the linear ME effect, either magnetization induced by electric field, ME_E, or electric polarization induced by magnetic field, ME_B. In fact, ME_B method is better than ME_E one, for the reasons that a high energy density can be generated with a magnetic field, and that ME_E measurement always has the risk of electrical breakdown due to the crystal defects. In any case, the so-called ME annealing, a process of applying both electric and magnetic fields when cooling the sample, is mandatory for obtaining the single ME domain state. Otherwise, the α_{ME} from different ME domains, usually has opposite sign, would cancel out and render the result to be less than the intrinsic value [17, 23, 22].

The pioneering measurement of ME effect was done by Astrov [19]. In his apparatus, a high AC electric field was applied to the sample, which is sandwiched by the two parallel capacitor plates, then the magnetic AC response was measured from the induced voltage amplitude in surrounding pickup coil. As the development of superconducting quantum interference device (SQUID) magnetometer, the Astrov's approach was improved by taking advantage of SQUID's high sensitivity [26]. Both DC and AC measurements of the ME effect were investigated by using the modified SQUID setup, as illustrated in Fig. 1.4, in which the
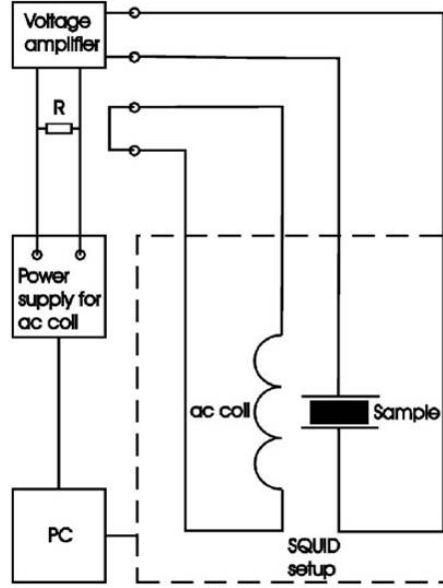
Figure 1.4: The schematic plan of a modified commercial SQUID magnetometer for ME susceptibility measurement. [26]

minimal ME susceptibility of 0.01 ps/m was achieved. However, the drawback for the bulk measurement is the requirement of ME annealing, which is difficult for systems with strong pinning effect. For example, in hexagonal manganites, where the defects are protected by the topological vortices, it's nearly impossible to fully polarize the crystal in ME annealing, as the electrical breakdown may occur under large electric field [27]. On the contrary, some local probe state-of-the-arts can map out the physical properties microscopically, which requires no ME annealing. For instance, magnetic second harmonic generation (SHG) is a powerful complementary method for imaging domains based on symmetry consideration [28, 29]. It may also be implemented for visualizing ME domains under certain circumstances. However, SHG is an indirect measurement with poor spatial resolution. Therefore, the mesoscopic technique with nanometer resolution and direct measure for the ME domain structure is urgently needed. We have successfully developed a novel technique, called magnetoelectric force microscopy (MeFM), to directly image ME domain pattern, which will be elaborated in Chapter 2.

1.3 Hexagonal REMnO$_3$
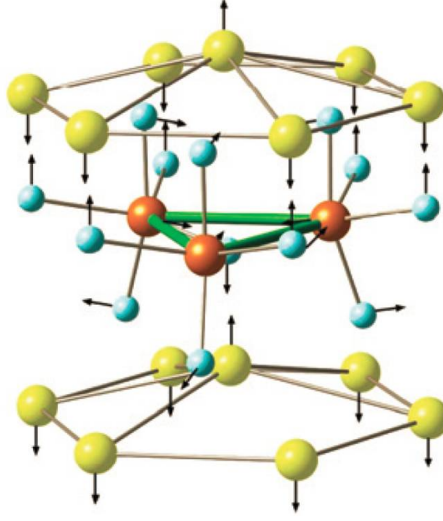
Figure 1.5: Schematic structure of hexagonal REMnO$_3$, the yellow, brown, and blue spheres denote the RE, Mn, and oxygen atoms, respectively.

Hexagonal manganites REMnO$_3$ (RE = Sc, Y, Ho, ... Lu) are multiferroics with coexistence of ferroelectricity ($T_\mathrm{C} \approx 1200$ - 1500 K) and antiferromagnetism ($T_\mathrm{N} \approx 70$ - 120 K) [30, 31, 32, 33]. Five oxygen atoms form a trigonal bipyramid cage, which contains the Mn ion at the center. The layer of MnO$_5$ polyhedra, forming close-packed planes, is separated by the layer of RE ions. Schematic structure is shown in Fig. 1.5. Tremendous studies have been focused on this topic due to its profound and complex magnetic interactions, including inter and intra Mn sublattice interaction, RE-RE interaction, and the interplay between Mn ($3d$) and RE ($4f$) sublattices [34, 28, 35]. The magnetic ordering of Mn spins, below T_N, is dominated by antiferromagnetic in-plane Mn-O-Mn superexchange, and supplemented by a 2 orders of magnitude weaker interplane Mn-O-O-Mn exchange interaction. Mn spins are confined in the basal plane due to the geometrical anisotropy, which overwhelms the magnetic frustration, resulting in the 120° arrangement [35]. The Ising-like rare earth spins, if any, are polarized by the Mn sublattice through $3d - 4f$ non-collinear interaction, while the RE-RE dipolar one may be responsible for the additional rare earth ordering below 5 K [36, 37, 38]. As for the ferroelectricity, it couples intimately to the lattice vibration mode,

for which the coupling mechanism was under debate for decades. In short, hexagonal manganites provide a fruitful playground for the interplays among lattice, charges, and spins, which are discussed in detail in the following subsections.

1.3.1 Origin of the ferroelectric transition
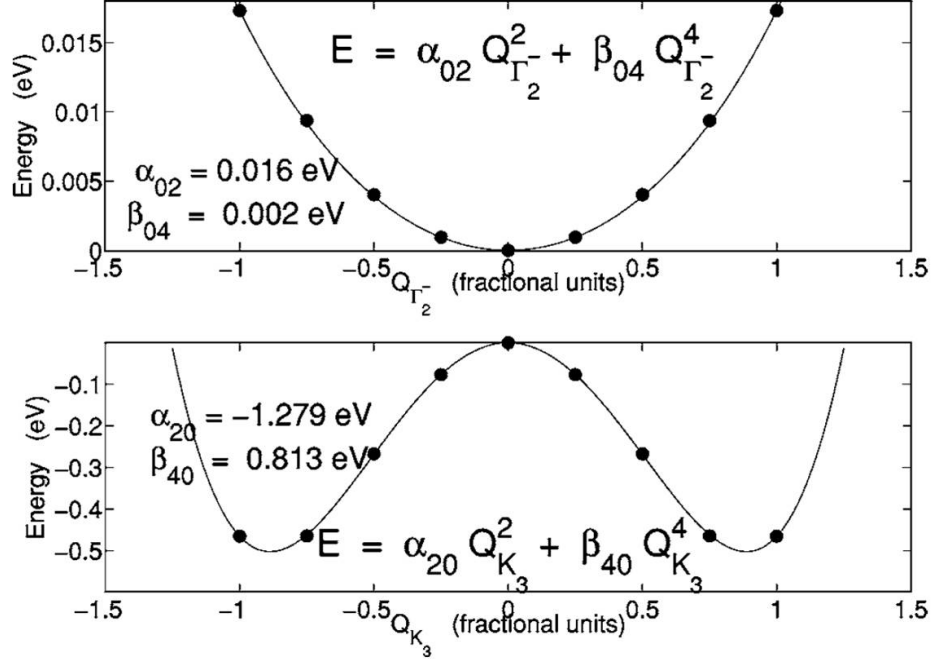
Figure 1.6: The energy as a function of $Q_{\Gamma_2^-}$ polar mode (top) and Q_{K_3} trimerization mode (bottom). [32]

Hexagonal REMnO$_3$ has large electric polarization below T_C, e.g., the polarization in YMnO$_3$ is 6 μC/cm^2 [39]. The ferroelectricity is characterized by the buckling of the MnO$_5$ polyhedra, and the displacements of the RE ions. Unlike perovskite oxides, e.g., BaTiO$_3$, where the Born effective charge induces the polarization [40, 41], a structural instability, known as trimerization mode, induces the ferroelectricity in hexagonal manganites. The sequence of the transition from high-temperature paraelectric phase (P6$_3$\mmc) to low-temperature ferroelectric phase (P6$_3$cm) has been the subject of debate [42, 43, 44, 30], and it is suggested, by using group-theoretical analysis and first-principles calculations, the polarization is strongly coupled to a single instability at the zone boundary [32].
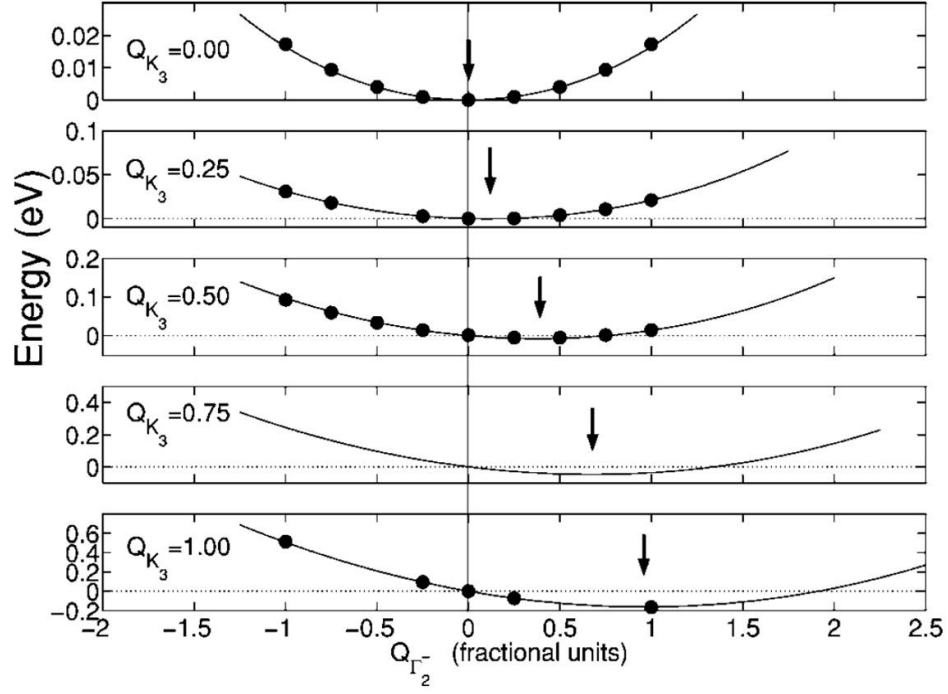
Figure 1.7: The energy landscape against the $Q_{\Gamma_2^-}$ mode as increasing the strength of Q_{K_3} mode. [32]

In the paraelectric P6$_3$\mmc phase, all the ions are confined in the same ab plane, whereas this mirror plane symmetry is broken in ferroelectric P6$_3$cm phase. First-principles density-functional calculations found that the K_3, zone-boundary mode at $q = (1/3, 1/3, 0)$, has the largest amplitude. This mode is also called trimerization, i.e., the unit cell triples and forms a $\sqrt{3} \times \sqrt{3}$ superstructure. The zone-center polar mode (Γ_2^-), which is responsible for the ferroelecticity, is a by-product of the primary trimerization mode, stemming from the cross-coupling term between Q_{K_3} and $Q_{\Gamma_2^-}$ [32]. By expanding the free energy to the fourth order in Q_{K_3} and $Q_{\Gamma_2^-}$ including all symmetry-allowed terms, it is:

$$F(Q_{K_3}, Q_{\Gamma_2^-}) = \alpha_{20}Q_{K_3}^2 + \alpha_{02}Q_{\Gamma_2^-}^2 + \beta_{40}Q_{K_3}^4 + \beta_{04}Q_{\Gamma_2^-}^4 + \beta_{31}Q_{K_3}^3 Q_{\Gamma_2^-} + \beta_{22}Q_{K_3}^2 Q_{\Gamma_2^-}^2 \quad (1.4)$$

As shown in Fig. 1.6, the polar mode is stable due to the positive α_{02} coefficient, showing a single well potential. On the contrary, the negative α_{20} coefficient results in the double-well shape energy in expansion of Q_{K_3}. Therefore, the primary ordering is the lattice tripling, i.e., the buckling of the MnO$_5$ polyhedra, and the polarization cannot emerge
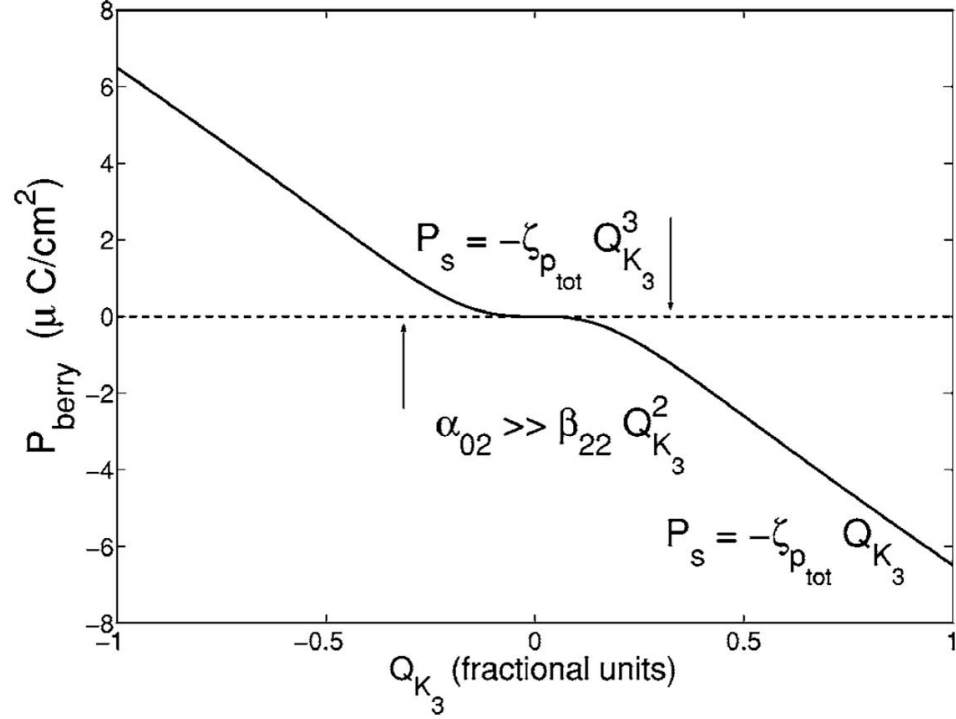
Figure 1.8: The emergence of the electric polarization as the primary order parameter Q_{K_3} grows. [32]

spontaneously with the $Q_{\Gamma_2^-}$ mode only. In the presence of the cross coupling terms, the equilibrium position of $Q_{\Gamma_2^-}$ starts to shift to a positive value with nonzero Q_{K_3}, resulting in a polarization, and it grows with increasing Q_{K_3}, as shown in Fig. 1.7. The polarization is characterized as downward distortion of two thirds of RE ions and upward distortion of the rest RE ions, as illustrated in Fig. 1.5.

Since the polarization is linearly proportional to the amplitude of $Q_{\Gamma_2^-}$, a relation between polarization and Q_{K_3} can be obtained by minimizing free energy with respect to $Q_{\Gamma_2^-}$, and the dependence is plotted in Fig. 1.8. The polarization firstly increases slowly, then turns into a linear increase with Q_{K_3}. The K_3 mode plays a role of kicking the polarization to nonzero equilibrium position, which is analogous to a crystal field. This coupling mechanism suggests that hexagonal manganites are improper ferroelectrics.
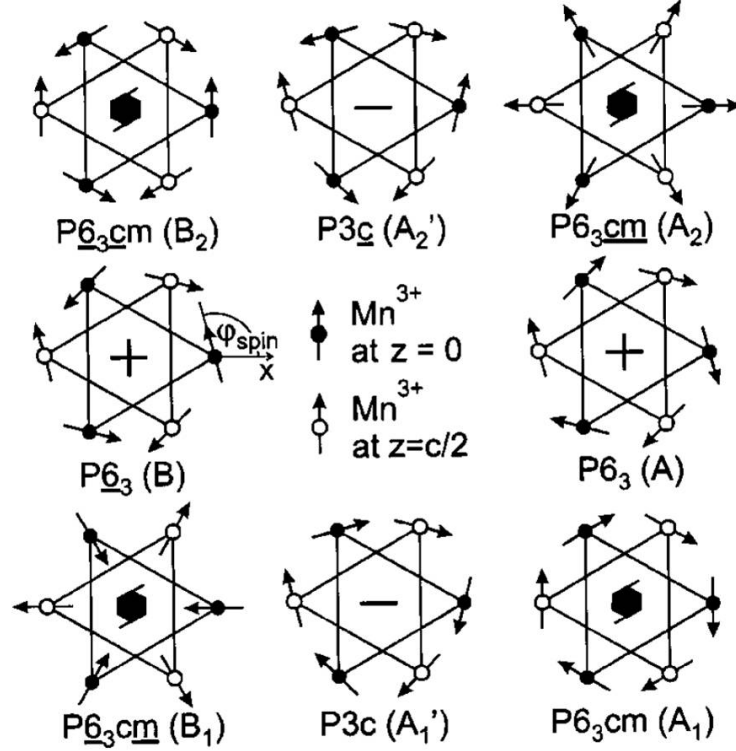
Figure 1.9: Triangular antiferromagnetic Mn^{3+} spins have A-type ferromagnetic and B-type antiferromagnetic coupling between adjacent planes along z. Different magnetic symmetries transform to each other via in-phase and out-of-phase spin rotations. [45]

1.3.2 Magnetic symmetries and the phase diagram

The determination of the magnetic symmetry is a key to evaluate the physical properties of matter, because symmetry can place constrains on the fundamental selection rules and conservation laws. Considering the complex magnetic structure in hexagonal manganites, various experimental techniques, including X-ray diffraction, neutron scattering, Faraday rotation, and second harmonic generation (SHG), provide complementary measurements for pinning down the magnetic symmetry. In particular, Fiebig has done some pioneering work, by using SHG, in determining the magnetic phases in hexagonal $REMnO_3$. This nonlinear optical method, based on the relation between induced polarization $P_i(2\omega)$ and applied electric field components $E_j(\omega)$ and $E_k(\omega)$ in Eq. 1.5, is able to distinguish the

possible Mn^{3+} spin structures [28, 46], like B_1 and B_2 symmetry in Fig. 1.9.

$$P_i(2\omega) = \xi_0 \chi_{ijk}^{\text{mag}} E_j(\omega) E_k(\omega), \tag{1.5}$$

By applying the electric field along different orientations, the induced polarization emerges only when χ_{ijk}^{mag} is nonzero. The set of nonzero χ_{ijk}^{mag} tensor components correspond to certain magnetic structure. All the possible magnetic phases in hexagonal manganites are list in Fig. 1.9, in which spin rotation angle $\varphi_{\text{spin}} = 0°$ or $90°$ is the ground state. For instance, hexagonal $ErMnO_3$ possesses the B_2 symmetry at zero magnetic field below T_N, applying high field induces an antiphase spin reorientation to A_2 phase through the intermediate one [28, 47]. The symbols refer to one-dimensional representations of the crystallographic point group [48]. The difference between A- and B-type structure lies in the nearest-neighbor spin ordering, whether it's antiferromagnetic or ferromagnetic coupling. Generally, A_2 phase is preferred at high magnetic field, for the reason that weak ferromagnetism is allowed when the MnO_5 polyhedra buckles.
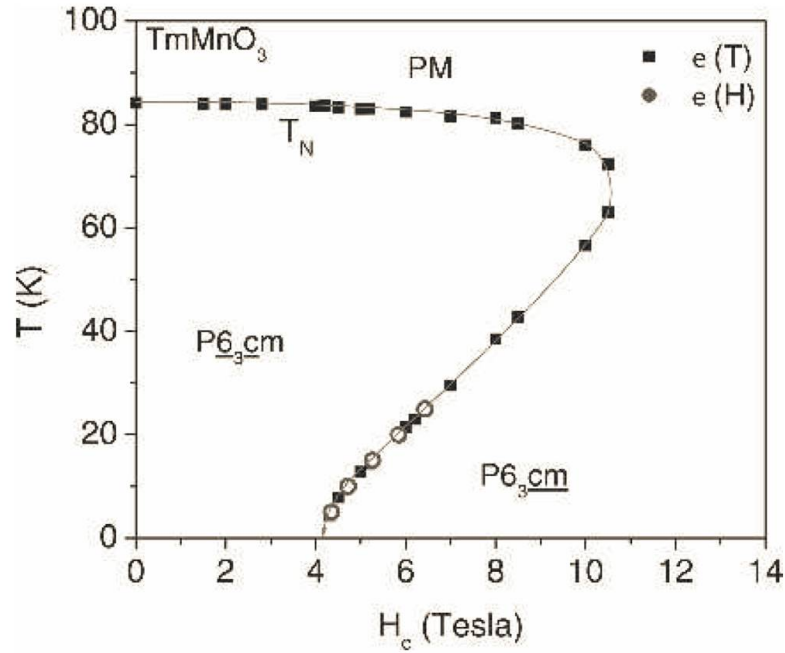
Figure 1.10: Magnetic phase diagram for $TmMnO_3$. The phase boundary is derived from anomalies of dielectric constant measurements. [49]

The magnetic phase diagrams of hexagonal manganites can be inferred from the measurements of magnetic, dielectric, optical and other physical properties [50, 51, 52]. Along the temperature axis, it goes through a second-order phase transition from paramagnetic to antiferromagnetic phase [35]. The shape of the T_N phase boundary shows a reentrant behavior, the representative phase diagram is plotted in Fig. 1.10, where the boundary is derived from the anomalies of $\varepsilon(T)$ and $\varepsilon(H)$ in TmMnO$_3$ [49]. This reentrant shape is also seen in other hexagonal manganites as well, like ErMnO$_3$ and YbMnO$_3$. Hexagonal HoMnO$_3$ is a special case with much more complex phase diagram, which is not discussed within the scope of this thesis. Due to the anisotropic exchange interaction between Mn^{3+} and RE spins, they conform the same magnetic symmetry. The Zeeman energy gain, at the Ising-like RE site under applied magnetic field, competes with thermal fluctuation, resulting in the bending over of the phase diagram. The Mn^{3+} spin reorientation transition has a two-step feature at low temperature (≤ 10 K): at first, the spin rotates into an intermediate region, characterized as a crossover transition; then it goes into the high magnetic phase through a second-order transition. The two phase boundaries merge at a critical point, below which is the first-order transition line. The subtle feature of the phase diagram will be discussed in Chapter 4.

1.3.3 Interlocked domain walls and multiferroic vortex

Intensive studies focused on hexagonal manganites are primarily due to the potential application for multi-functional memory devices. Because the formation of domains is the hallmark of any ferroic order, it is of both fundamental and technological interest to microscopically visualize cross-coupled domains and domain walls in multiferroics [54]. There are a large body of evidences showing the interplay among microscopic spin, charge, and lattice degrees of freedom in hexagonal manganites. The pioneering work, done by Fiebig, in imaging the crossed coupling domain walls was achieved by using the nonlinear SHG technique [53]. Because the 180° electric and magnetic domains break the spatial inversion and time
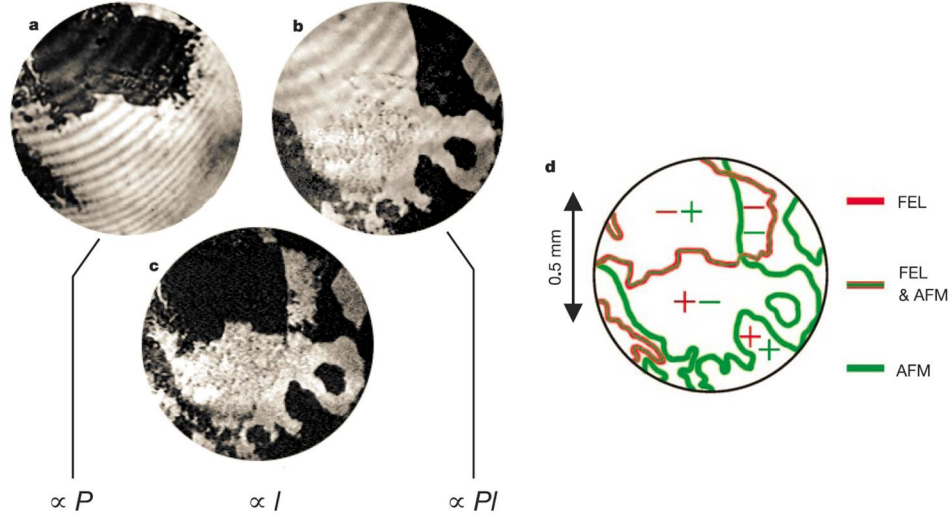
Figure 1.11: Coexistence of magnetic and electric domains in $YMnO_3$ imaged with SHG. Exposed second harmonic light from $\chi(P)$ (**a**), $\chi(Pl)$ (**b**), and $\chi(l)$ (**c**). The dark and bright color corresponds to opposite ferroelectric (**a**), magnetoelectric (**b**), and antiferromagnetic domains (**c**). The schematic of the cross-coupled domain walls are illustrated in **d**. [53]

reversal symmetry, respectively, SHG is able to distinguish the domains in a single setup. By monitoring the SHG intensity at different temperature ranges: $T_C > T > T_N$, and $T_N > T$, the electric polarization domain (Fig. 1.11a) and the ferroelectric antiferromagnetic domain (Fig. 1.11b) can be visualized. Surprisingly, the ferroelectric domains are always coupled with the magnetic ones, as shown in Fig. 1.11d, suggesting the intrinsic magnetoelectric coupling. Furthermore, free magnetic domain walls, not associated with the polarization reversals, are present as well. The clamping mechanism was attributed to strain mediation and reconstruction of spin interactions at the polarization boundaries. However, the spatial resolution in SHG ($\approx 10\ \mu$m) is not high enough to clarify the microscopic mechanism.

Recent advanced microscopic observations have shed light on the clamping mechanism in bulk hexagonal manganites. T. Choi *et al*. performed the transmission electron microscopy (TEM) measurements on a thin $YMnO_3$ single crystal, and observed the emergence of six domains from the central point, resembling a cloverleaf pattern [27]. The high-resolution (≈ 10 nm) TEM observation has identified the presence of structural antiphase domain boundaries (APBs), as shown in Fig. 1.12a. This cloverleaf pattern is assigned with a
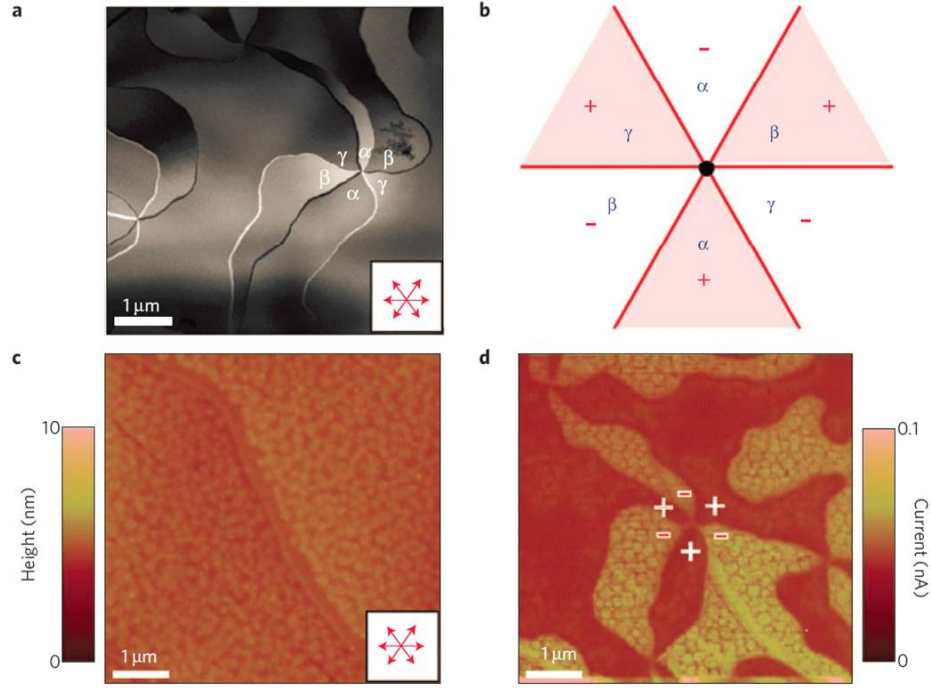
Figure 1.12: **a**, TEM dark-field image shows the antiphase domains emerging from the central point. **b**, the schematic describes that the antiphase structural domain boundary interlocks with the ferroelectric one. Topography (**c**) and CAFM (**d**) images are taken at the same location, demonstrating the smooth surface with nanometer roughness and the striking cloverleaf domains with conductive contrast. [27].

periodic configuration of three types of antiphase domain, $\alpha - \beta - \gamma - \alpha - \beta - \gamma$. Those three types of antiphases stem from the three possible trimerization distortion, as described in Fig. 1.13. One intriguing feature in the dark-field TEM image, Fig. 1.12a, is that bright and dark contrasts alternate around the center, corresponding to the upward and downward electric polarization domains. Therefore, it is emphasized that the APBs intimately interlocked with the ferroelectric domain boundaries, forming a cyclic configuration [$\alpha+$, $\beta-$, $\gamma+$, $\alpha-$, $\beta+$, $\gamma-$], shown both in Fig. 1.12b and Fig. 1.13 [27, 56]. Other microscopic complementary measurements, like conducting atomic-force microscopy (CAFM) (Fig. 1.12d) and piezo-response force microscopy (PFM) [57, 58], all suggest six alternating ferroelectric domains emerge from the vortex point, which is thus noted as multiferroic vortex. The presence and robustness of the vortices are topologically protected by the structural defects. More elaborate Landau theory, with parameters determined from first-principles calculations,
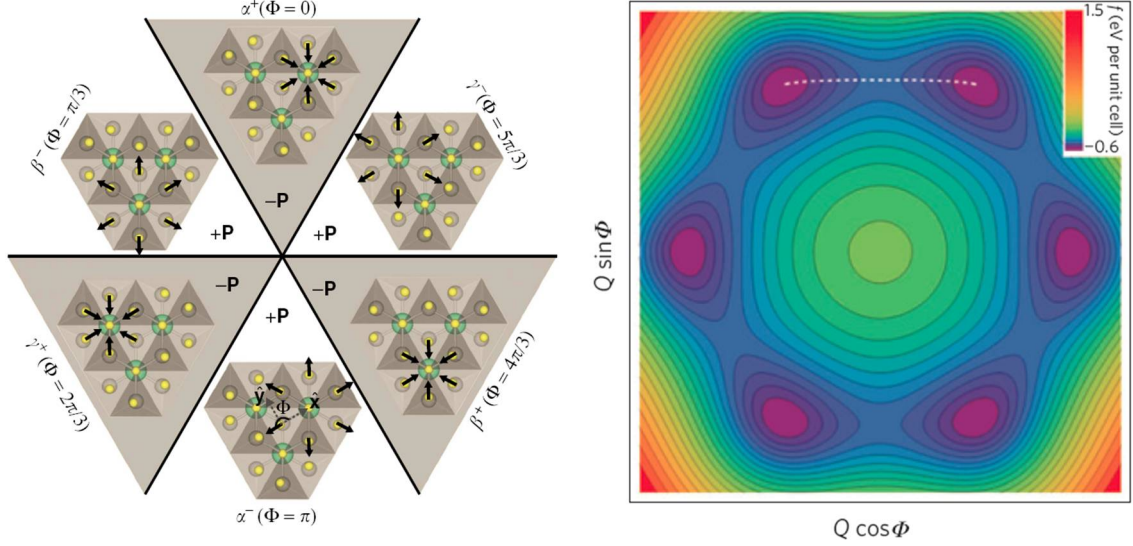
Figure 1.13: On the left, six structural antiphase domains with the arrows denoting the direction of the apical oxygen distortion. The Mexican hat shape of the free energy landscape (right panel) in hexagonal manganites, Q and Φ denote the amplitude and phase of the trimerization state. [33, 55]

outlines the free energy landscape in terms of the trimerization amplitude Q and phase Φ [33]. The contour plot shows a Mexican hat shape, suggesting $[\alpha+, \beta-, \gamma+, \alpha-, \beta+, \gamma-]$ are indeed the six ground states. Moreover, it reveals that the lowest energy domain wall configuration is the shortest path (white dotted line in Fig. 1.13) connecting two neighbouring states whose phase differs by $\pm\pi/3$. Therefore, the only possible configurations are $[\alpha+, \beta-, \gamma+, \alpha-, \beta+, \gamma-]$ (vortex) and $[\alpha+, \gamma-, \beta+, \alpha-, \gamma+, \beta-]$ (anti-vortex), which agrees with a graph theory study of vortex network [59]. In addition, vortex-like charged ferroelectric domain walls in the ab plane are also observed by PFM, CAFM and Kelvin-probe force microscopy [60, 61]. The multiferroic vortex, so far, has included the degree of freedoms of charge and lattice. A major part of my thesis work is to demonstrate that it is also magnetic spin and magnetoelectric vortex, which is discussed in Chapter 3 and 4, respectively.

Chapter 2

Development of magnetoelectric force microscopy

In 1981, the scanning tunneling microscopy (STM) was invented by Binnig *et al.* for imaging the individual atoms [62]. Later on, huge success was achieved by utilizing STM in exploring the sub-nanometer world, and Binnig and Rohrer won with the physics Nobel Prize in 1986. Due to the mechanism of tunneling, STM is limited to conductive materials such as metals and semiconductors. To extend the applications to insulating materials, Binnig *et al.* developed the atomic force microscopy (AFM) shortly after the invention of STM [63]. The operation of AFM is much more robust in various environments than STM, which needs ultra-high vacuum to prevent surface contamination. AFM can be implemented under ambient condition, and can be used for measurements of any materials in solid and even in liquid. The basic principle is to detect the atomic force, which is composed of long-range attractive van der Waals force and short-range repulsive Coulomb one, as shown in Fig. 2.1. It has various variants depending on the measured forces and the operation modes. For example, the general AFM can map out the topographic features of the surface with $\approx$ 10 nm lateral resolution and < 1 nm resolution in height. If the electrostatic or magnetic interaction exists between the tip and the sample, an electric potential or magnetic stray field map can be obtained, i.e., electric force microscopy (EFM) or magnetic force microscopy (MFM). This is possible for the reason that electric/magnetic force dominates at long-range, while atomic force is effective at short-range.

In scanning force microscopy, a sharp tip, located at the end of a cantilever, is attached to a $x - y - z$ piezo-scanner, which can precisely control the movements of the cantilever along three orientations. There are several operation modes, including contact, non-contact,
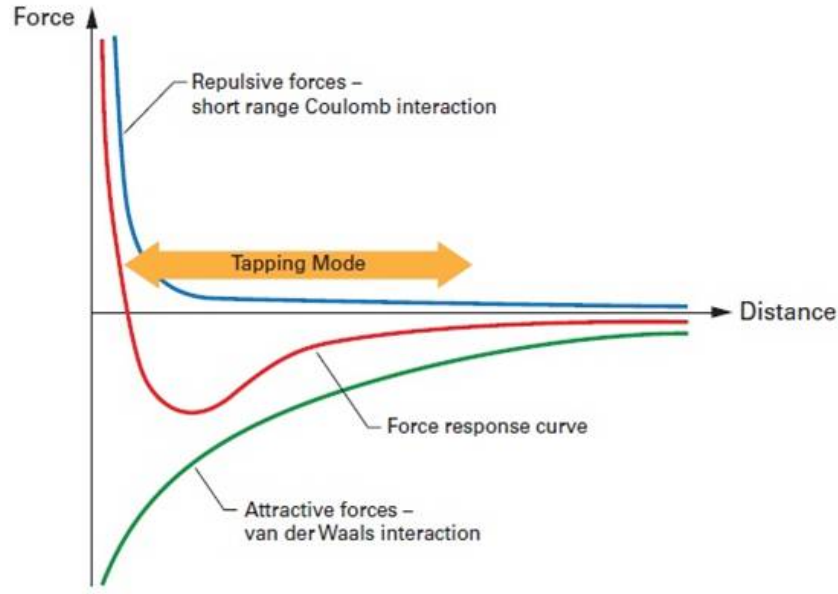
Figure 2.1: The force response curve (red) is a sum of long distance attractive van der Waals force (green) and short range repulsive force (blue).

tapping, constant height modes etc., for different measurement purposes. In contact mode, the tip is pressed against the sample surface, and the cantilever deflection is used as the feedback signal. By coating the tip with conductive material, it can be used for local current (CAFM) or piezo-response (PFM) measurements. In non-contact mode, the tip is hovering 5 - 15 nm above sample surface, in which the attractive van der Waals force gradient is used as the feedback signal. For the tapping mode operation, the tip gently taps the surface, and the cantilever vibration amplitude is maintained constant through the feedback loop. It allows high resolution topographic imaging with minimal damage to the surface, and reliable EFM/MFM measurements by alternatively putting the tip in tapping and lift mode. All the modes above are controlled via a feedback loop on the piezo-scanner, while in constant height mode the tip scans over a pre-determined plane with feedback turned off, which allows "quiet" measurements without noise generated by feedback loop. The specific force microscopy techniques, like MFM, PFM, and the novel magnetoelectric force microscopy (MeFM) invented by our lab, will be discussed in detail in subsequent sections.

2.1 Cryogenic magnetic force microscope
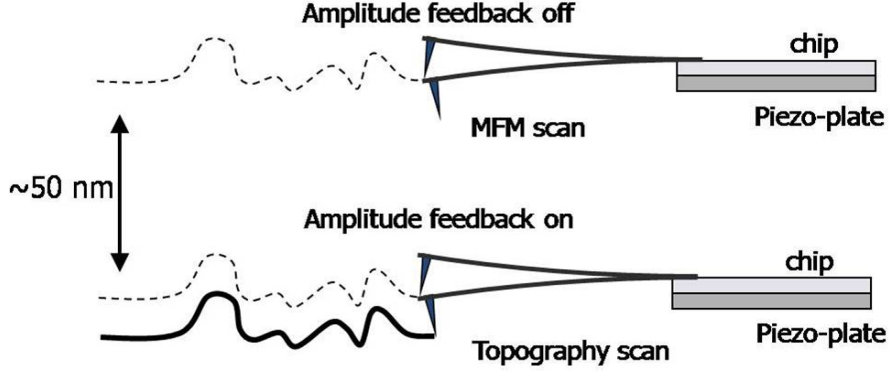
Figure 2.2: In MFM, the topography and magnetic line profile are measured successively. The interleave mode can minimize the topography-related feature.

Magnetic force microscopy (MFM) is a powerful tool to detect local magnetic dipoles with high spatial resolution (20 - 50 nm) and high magnetic sensitivity, it is widely applied in industry and fundamental research for imaging magnetic domains and domain walls [65]. The basic principle of MFM is to sense the magnetic interaction of tip/sample system:

$$U = - \int M_{\text{tip}}(r) \cdot B(r) dr \tag{2.1}$$

where M_{tip} is the tip magnetization, $B(r)$ is the magnetic stray field from the sample [66, 67]. Approximately, the tip magnetization can be considered as a constant dipole magnetization M, and the interaction, to the first order of estimation, is

$$U = -m \cdot B \tag{2.2}$$

Then the measured magnetic force is

$$F = - \triangledown U = \sum \frac{\partial}{\partial i}(m_x B_x + m_y B_y + m_z B_z)\hat{i} = m_z \frac{\partial}{\partial z} B_z \hat{z} \tag{2.3}$$

where the last equality holds up by assuming the tip is only sensible to out-of-plane stray field.
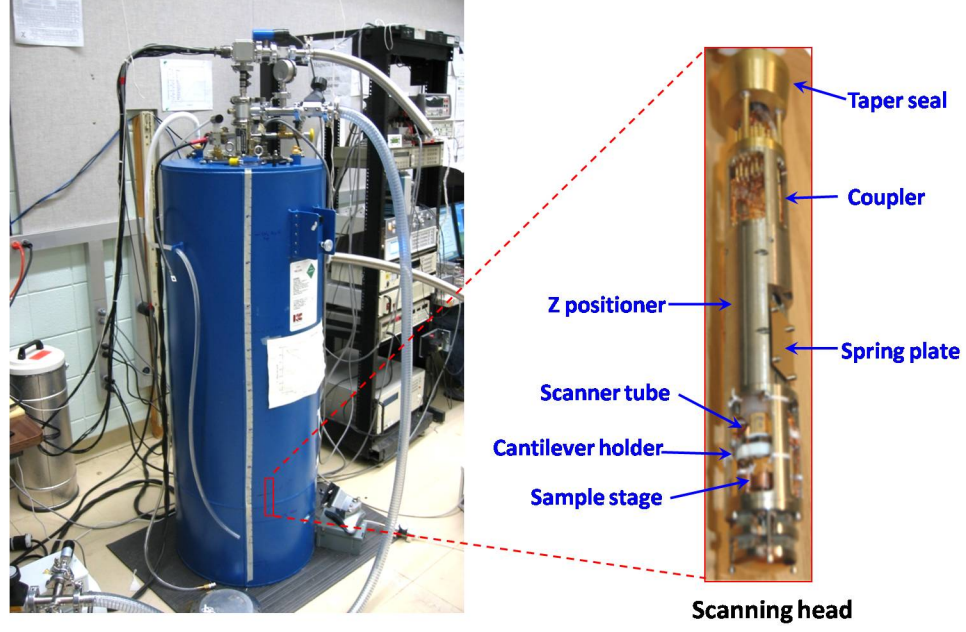
Figure 2.3: The picture of our home-built cryogenic MFM (left) and the scanning head (right).

First of all, considering the cantilever as a mechanic spring with force constant k_0, then effectively

$$k = k_0 - F_z' \tag{2.4}$$

the "spring" is softened or stiffened by the force gradient. Thereafter, the resonant frequency of the cantilever changes accordingly

$$f = \frac{1}{2\pi}\sqrt{\frac{k}{m}} = \frac{1}{2\pi}\sqrt{\frac{k_0 - F_z'}{m}} = f_0(1 - \frac{F_z'}{k_0})^{1/2} \approx f_0 - f_0\frac{1}{2k_0}F_z' \tag{2.5}$$

So the frequency shift of the cantilever resonant frequency is

$$\frac{\Delta f}{f_0} = -\frac{F_z'}{2k_0} = -\frac{m_z}{2k_0}\frac{\partial^2 B_z}{\partial z^2} \tag{2.6}$$

which relates MFM signal (Δf) to the magnetic force gradient. The MFM signal is demodulated via the frequency modulation (FM) technique, which keeps tracking the cantilever's resonant frequency through a phase locked loop [68]. Under certain circumstances, the second derivative of the stray field is equivalent to the magnetization distribution, i.e., the measured "frequency shift" image approximately represents the magnetic domain patterns.
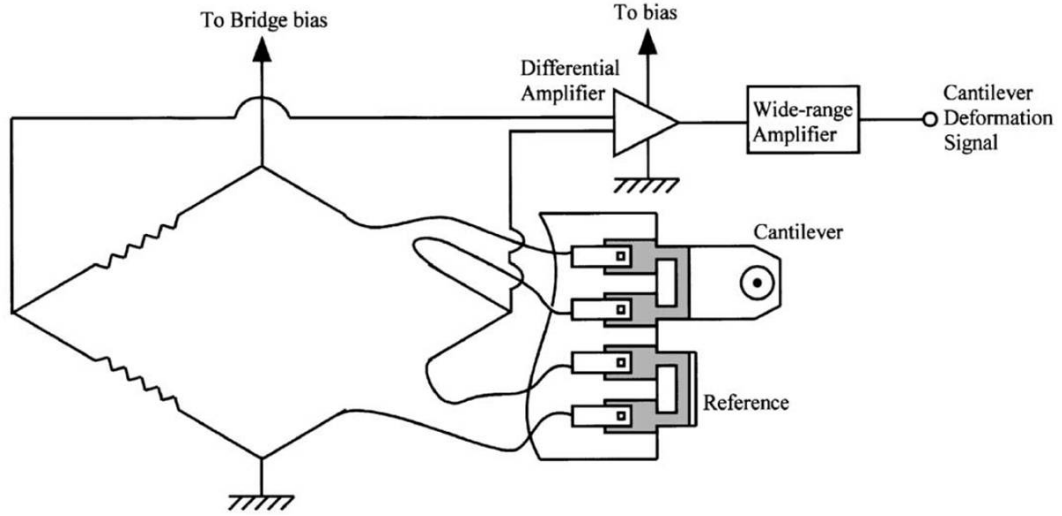
Figure 2.4: Schematic of the self-sensing piezo-resistive cantilever circuit. The cantilever deflection is monitored by the change of the resistance, which is precisely measured by the Wheatstone bridge. [64]

As shown in Fig. 2.2, MFM is taken with the interleave mode: it firstly scans the topography with tapping mode, then the tip is lift to maintain constant height from surface. In the lift mode, the amplitude feedback is turned off, and only the long-range magnetic force is sensed. The constant lift height guarantees that the topography effect is minimized in MFM image.

The instrument I mainly worked on is our home-built cryogenic magnetic force microscope, shown in Fig. 2.3, which is capable of magnetic imaging in a wide temperature range (2.5 - 300 K) with $in-situ$ high magnetic field (8.0 T) and high voltage (1.0 kV). The scanning probe has a compact design, a circular cylinder with a 8-inch height and a 1-inch base radius, and it is suitable for liquid helium experiments. The apparatus is interfaced with a Nanoscope IIIa (Bruker) controller and a Nanois Phase Locked Loop (SPECS). The cantilever displacement is sensed by the piezo-resistive method, i.e., the stress-induced resistivity change of piezo-resistive material integrated on the cantilever, as illustrated in Fig. 2.4 [64, 69]. The cantilever resistance is precisely balanced by a Wheatstone bridge. The difference between the cantilever and reference is amplified 2000 times via a differential amplifier, it is then fed to the controller as the cantilever deflection signal. The MFM tips

are fabricated by coating the bare tips with nominally 60 nm Co film using electron-beam evaporation, which is capped with 2 nm Cr layer to prevent oxidation [70]. The direction of the tip moment is determined by external magnetic field.

We have invented a cutting-edge mesoscopic technique, called magnetoelectric force microscopy (MeFM), to directly image and measure the local magnetoelectric (ME) domains [71]. Although sensitive techniques have been developed for macroscopic measurements of ME effects, little has been done on mesoscopic detection within a single domain or at domain walls. The ME effect is usually measured through macroscopic methods, like the Astrov apparatus mentioned in Section 1.2.2. Hence, it is necessary to perform the ME annealing, i.e., applying magnetic and electric fields simultaneously through the magnetic transition temperature, to obtain a single ME domain for reliable measurements. The ME annealing, on one hand, can be difficult for systems with strong pinning effects. On the other hand, the mesoscopic detection of the bulk ME effect of domains or domain walls has never been realized [72]. The direct observation of ME effects in the domains (and/or at domain walls) is crucial to reveal the underlying mechanisms of ME coupling. Our cryogenic MFM system can apply high electric field, without interference with the magnetic detection. The lock-in technique is applied to enhance the signal to noise ratio to detect weak local ME effect.

2.2   MeFM design principle

The basic principle of the MeFM setup is shown in Fig. 2.5. The sample is sandwiched by two electrodes, forming a parallel plate capacitor-like structure. A thin gold film ($\sim$50 nm) is deposited on the surface as the top electrode, which is electrically grounded to eliminate the electrostatic interactions between MFM tip and sample. A high AC voltage $V(\omega)$ ($\omega/2\pi$ = 10-300 Hz) is applied to the bottom electrode, generating an alternating electric field $E(\omega)$ throughout the sample. In a magnetoelectric material, the magnetic stray field $B(\omega)$, from the induced magnetization $M_{\mathrm{E}}(\omega) = \alpha_{\mathrm{ME}} \cdot E(\omega)$, would be modulated at the same frequency as that of the applied voltage.
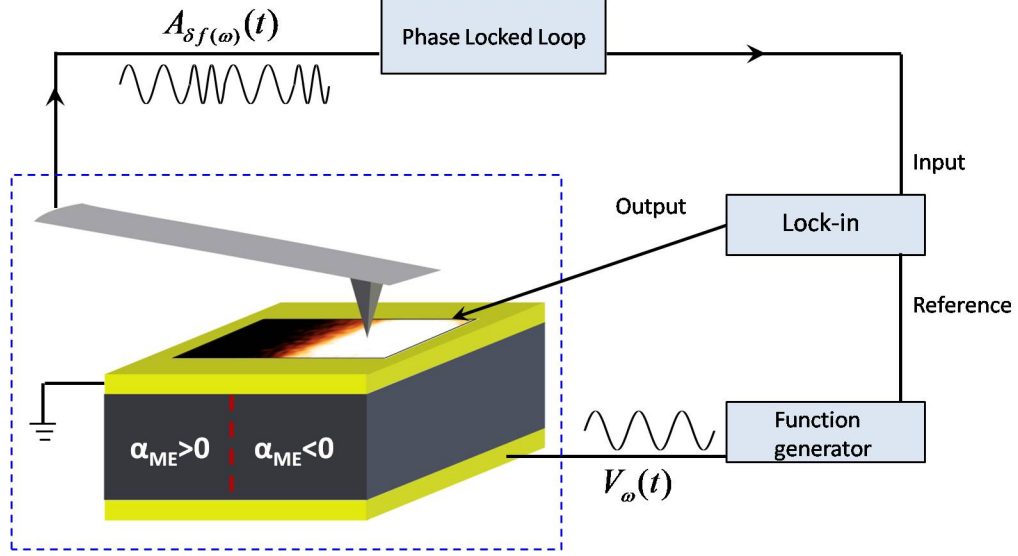
Figure 2.5: The voltage-induced magnetic signal is demodulated by a phase locked loop and a lock-in amplifier, successively. The output of the lock-in amplifier is recorded as the MeFM image. An example of ME domain is shown with a perspective view. [71]

The magnetic stray field is detected by a magnetic tip lifted from surface, resulting in a modulated MFM signal $\delta f_\omega(t)$, which is extracted by a phase locked loop (PLL). The modulated MFM signal is further fed to a lock-in amplifier to demodulate the M_E signal. The output of the lock-in amplifier is recorded as the MeFM image while the MFM tip scans over the sample surface. Consequently, the M_E signal is linearly proportional to the applied electric field, as described by Eq. 2.7. The ME domains can be directly visualized by MeFM due to different ME coefficients α_{ME}, showing different color contrasts in MeFM, the perspective image in Fig. 2.5.

$$\delta f_{\mathrm{MeFM}}(\omega) \propto \partial_z B(\omega) \propto M_{\mathrm{E}}(\omega) = \alpha_{\mathrm{ME}} \cdot E(\omega) \qquad (2.7)$$

The design of the MeFM is realized in our home-built cryogenic MFM. The sample is glued on a piece of sapphire plate with silver epoxy, which also serves as the back electrode. The sapphire plate is used for excellent electrical isolation and thermal conduction. An alternating voltage is generated from a standard lock-in amplifier (SR830) and is amplified by a Nanonis high voltage amplifier. To avoid the electrical interference, the modulated

high voltage is transmitted through a coaxial cable. The modulation frequency (10-300 Hz) is far separated from the resonant frequency of the cantilever (≈ 40 kHz).

To reliably measure the E-induced magnetic signal, the tip is maintained at a constant height (20-200 nm) from sample surface. One way is to use the frequency shift as topography feedback, i.e., non-contact mode, in which the force curve is calibrated to fall into the van der Waals range, where the frequency shift versus distance has a slope with fixed sign. The tip is able to approach closely to the surface (<10 nm). The tuning parameters for z feedback is carefully adjusted so that it is fast enough to follow the slope of the sample surface plane, but slow enough not to respond to the modulated magnetic signal. For example, if the electric field modulates at 50 Hz, the time constant of the z feedback should be larger than 20 ms to be insensitive to modulated stray field. On the other hand, if the feedback parameters are too slow, the z-piezo may not response timely to the large topography variation, resulting in the tip crash. However, the constant height approximation fails in the presence of strong static magnetic signal, which mixes with the van der Waals force, causing the tip to follow the magnetic pattern rather than the intrinsic topography. Alternatively, the topography feedback is disabled, and the MFM tip scans over a predetermined plane with a constant height from sample surface by intentionally outputting voltages to control the scanner. This is achieved by breaking in the communication between the scanner and the controller: at first, the surface plane is measured by locating four corners with topographic scan, and the flying plane is calculated with constant height offset from the surface via a LABVIEW program; then, z-piezo voltage is carefully controlled based on the measured xy voltage during scanning. Note this mode requires a strict thermal stability of the MFM system over a long period to avoid the tip crash due to thermal drift. In either case, the feedback of the PLL has to be fast enough to capture the modulated magnetic signal M_{E}. The demodulated MFM signal is fed to the input of the lock-in amplifier and the in-phase signal (i.e., x-channel) is recorded as the MeFM image.

2.3   Results and cross-checks
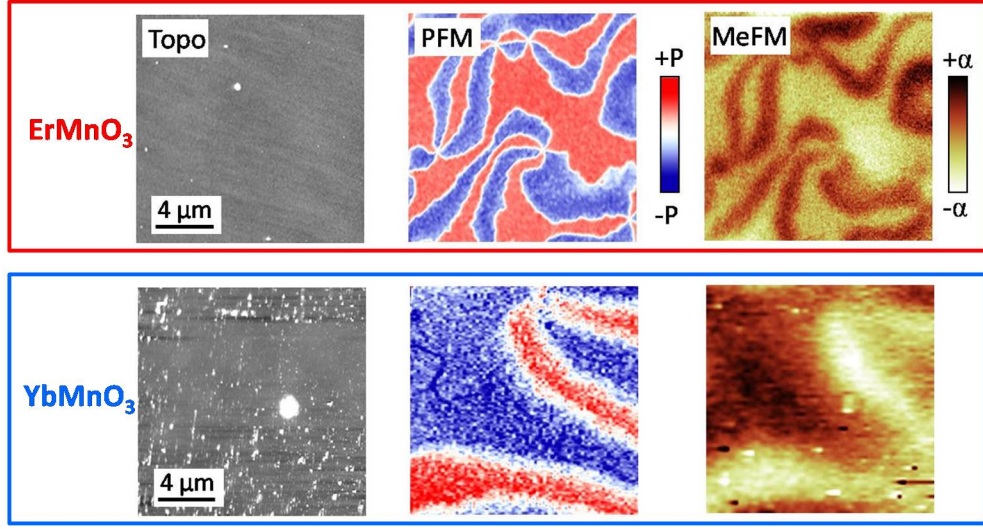
Figure 2.6: The topography, PFM, and MeFM images on the (001) surface of hexagonal ErMnO$_3$ (red boxed) and YbMnO$_3$ (blue boxed). [71]

To demonstrate the feasibility of the MeFM, the local ME responses of hexagonal manganites, ErMnO$_3$ and YbMnO$_3$, were studied. By performing measurements under various temperatures and magnetic fields, we achieved, for the first time, the unprecedented direct visualization of magnetoelectric domains, which coincide with the ferroelectric domains, as shown in Fig. 2.6. Comprehensive MeFM studies suggest that the magnetoelectric coupling in hexagonal manganites is mediated through a lattice instability, which is corroborated by symmetry analysis as well as a phenomenological modeling. More details will be discussed in Chapter 4.

To ensure the observed MeFM signal is from intrinsic ME effects, we have performed several cross-checks and control experiments. Since long-range forces, including magnetic and electrostatic interaction, would contribute to the MFM signal, numerous efforts were taken to eliminate the extrinsic electrostatic interaction. For instance, the sample is coated with an adequately thick gold film (50 nm) which is grounded to screen all the electric fields. Thin ($\leq$200 μm) plate-like crystals are chosen to minimize the stray electric field coming from the edges of electrodes. A control MeFM measurement was performed on a
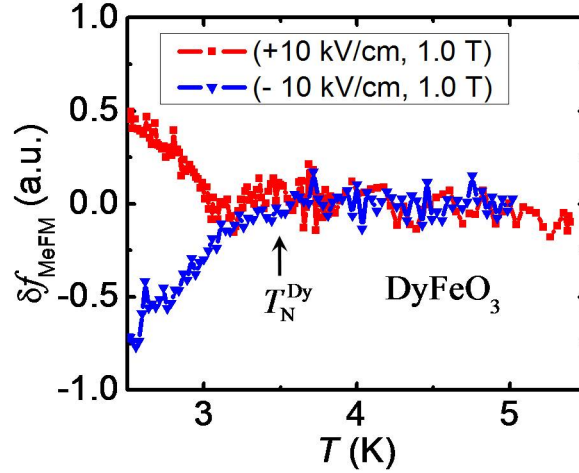
Figure 2.7: The combination of the annealing E and B fields determines the sign of the ME coupling coefficient, and its amplitude scales with the antiferromagnetic order parameter below T_N^{Dy}. The T-dependence of the linear ME effects in $DyFeO_3$ were measured with MeFM after different annealing conditions ($E = +/-10$ kV/cm, $B = 1.0$ T). [71]

piece of glass coated with gold film, and no MeFM signal was detected with the application of E and B fields, excluding the possibility of contamination from electrostatic interaction. Furthermore, another linear ME system, the orthoferrite $DyFeO_3$, was investigated as well. It has giant ME response below the Dy^{3+} ordering temperature ($T_N^{Dy} \approx 3.5$ K), and the sign of α_{ME} depends on the orientations of annealing E and B fields [73]. The temperature-dependent MeFM studies were performed on the (001) surface of $DyFeO_3$ after preparing bulk single domain states with different ME annealing. The measured MeFM signal is in agreement with a previous study, i.e., the temperature dependence of B-induced electric polarization in $DyFeO_3$, as shown in Fig. 2.7.

The influence of $E-$induced surface deformation to MeFM signal is negligible because of the weakness of piezo-response coefficient d_{33} (<1 pm/V) of hexagonal manganites, and the cancellation of d_{33} due to the random stacking of ferroelectric domains along the c-axis. The MeFM contrast is linearly proportional to the amplitude of applied E field, as shown in Fig. 2.8, indicating that it is a linear response. In addition, both the magnitude and the phase of MeFM signal are independent on the modulation frequency, confirming the
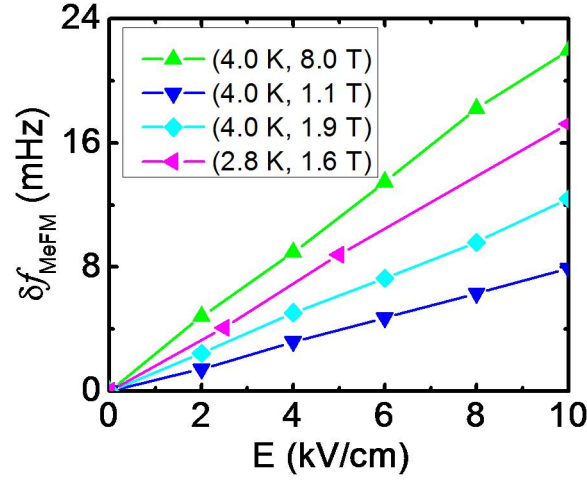
Figure 2.8: *E*-field dependence of the MeFM contrast at various representative magnetic field and temperature points in hexagonal ErMnO$_3$. [74]

magnetization induced by electric field as the origin.

2.4 Performance optimization
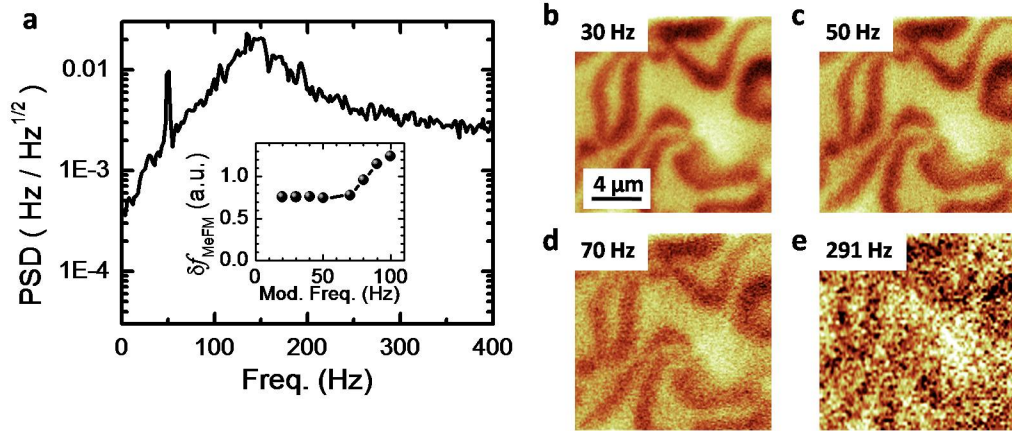
Figure 2.9: **a**, the power spectral density of the MFM signal with the modulation voltage ($V_{\mathrm{rms}} = 200$ V, $\omega/2\pi = 50$ Hz) applied to the back electrode. The inset shows the MeFM signal under various modulation frequencies. **b** − **e**, MeFM images are taken at the same location with 30 Hz, 50 Hz, 70 Hz, 291 Hz modulation voltage applied. The color scale in **e** is one tenth of that in rest images. [71]

Due to the weakness of ME effect, a lot of efforts are focused on tuning experimental

parameters to optimize the signal to noise ratio (S/N). The power spectral density (PSD) of

Fourier transform of MeFM signal is a powerful tool to analyze the modulated magnitude of signal and noise. Figure 2.9a shows a representative PSD of the MFM signal, in which a 50 Hz alternating voltage (200 V) is applied. The peak at 50 Hz corresponds to the modulated ME signal. The "hump" around 150 Hz is caused by the effective bandpass filter of frequency feedback in PLL. It results in the attenuation of demodulated signal at high frequency [75]. The modulation frequency dependence of the MeFM contrast is plotted in the inset of Fig. 2.9a. Apparently, it remains constant at low frequency (<80 Hz), and gradually increases when approaching the bump. Note that the PSD baseline represents the convolution of frequency noise and the transfer function (an effective damped harmonic oscillator) of PLL. Therefore, the rise of the frequency signal at higher frequencies (>80 Hz) is probably caused by the resonant enhancement of the background noise. Figure 2.9 show the MeFM images with E field modulated at different frequencies. They have similar image contrast at low modulation frequencies, while the one with high modulation frequency has much smaller contrast, in which the color scale is only one tenth of that in the rest images. In addition, lower modulation frequency produces lower noise level, resulting in better S/N, which is consistent with the trend of PSD baseline. However, lower modulation frequency requires longer averaging time to obtain the intrinsic ME response. For example, 30 Hz modulation needs 0.1 s for each data point, then capturing a (256×128) MeFM image takes approximately 1 hour. Therefore, as a trade-off between data quality and efficiency, the nominal modulation frequency is chosen to be 50 Hz for MeFM measurements.

2.5   Signal estimation

Based on Equation 2.7, the measured signal δf_{MeFM} is proportional to the product of ME coefficient and applied electric field. To get a reasonable estimation of α_{ME}, we need to consider various factors, e.g., the tip strength, lift height, and the electric field. The E-field induced magnetization (M_{E}) is estimated by comparing the MeFM signal with the MFM signal measured on a known ferromagnet. Because the MFM signal originates from the

dipolar interaction between the MFM tip and the local magnetic domain, δf_{MFM} is approximately proportional to the product of the MFM tip moment m_{tip} and the magnetization of the local domain (M_{domain}), that is

$$\delta f_{\mathrm{MFM}} \propto m_{\mathrm{tip}} \cdot M_{\mathrm{domain}} \tag{2.8}$$

The same formula is applied to the MeFM signal, i.e.,

$$\delta f_{\mathrm{MeFM}} \propto m_{\mathrm{tip}} \cdot M_{\mathrm{E}} \tag{2.9}$$

By comparing the image contrast of the MeFM images with that of the MFM images of a known ferromagnet, the M_{E} signal can be estimated as following:

$$M_{\mathrm{E}} = \frac{\delta f_{\mathrm{MeFM}}}{\delta f_{\mathrm{MFM}}} \frac{m_{\mathrm{tip(MFM)}}}{m_{\mathrm{tip(MeFM)}}} M_{\mathrm{domain(MFM)}} \tag{2.10}$$

Here we use the ferromagnatic $Fe_{1/4}TaS_2$ ($T_{\mathrm{C}} \sim 160$ K) as the calibration sample, which has strong uniaxial anisotropy with out-of-plane easy axis [76]. The ferromagnetic domain patterns are observed on single crystals of $Fe_{1/4}TaS_2$ after zero field cooling using our cryogenic MFM [77]. A representative MFM image measured at 60 K is shown in Fig. 2.10. The ratio of the MFM tips' moments was estimated from MFM measurements on the same reference sample (a commercial magnetic tape) at room temperature. From Eq. 2.8, we obtain the ratio between different tips:

$$\frac{m_{\mathrm{tip(MFM)}}}{m_{\mathrm{tip(MeFM)}}} = \frac{\delta f_{\mathrm{tip(MeFM)}}^{\mathrm{tape}}}{\delta f_{\mathrm{tip(MFM)}}^{\mathrm{tape}}} \tag{2.11}$$

Using the saturated magnetization of $Fe_{1/4}TaS_2$ (1 μ_{B}/f.u.) for M_{domain}, and the MFM image contrast of Fig. 2.10 ($\delta f_{\mathrm{MFM}} \sim 16.5$ Hz), the induced magnetization M_{E} can be obtained based on Eq. 2.10. For example, the MeFM study on $ErMnO_3$ has a strength of 3.83 mHz (δf_{MeFM}), the induced magnetization M_{E} is estimated to be 6.8×10^{-5} (μ_{B}/f.u.). Therefore, the linear magnetoelectric coupling coefficient can be estimated using the definition $\alpha = M_{\mathrm{E}}/E \approx 13$ ps/m ($E = 10^6$ V/m), which agrees with the first-principles calculations. Similar results are obtained using the same calibration procedure on different $Fe_{1/4}TaS_2$ single crystals and other ferromagnetic samples.
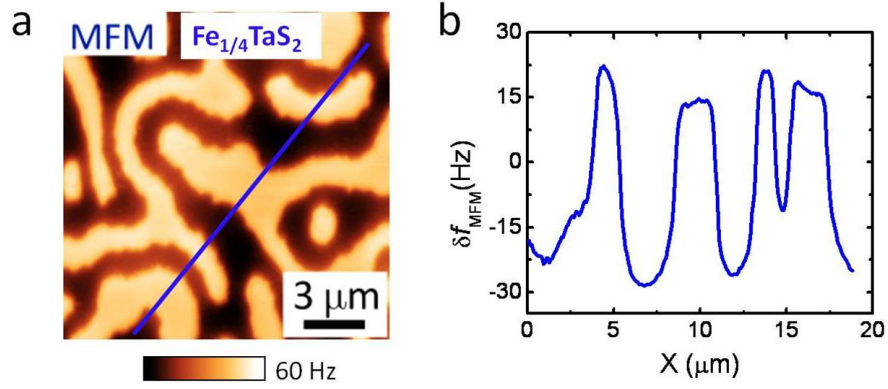
Figure 2.10: **a**, the out-of-plane magnetic domain patterns on the (001) surface of a $Fe_{1/4}TaS_2$ single crystal were observed in MFM at 60 K after zero field cooling. **b**, a representative line cut of the blue line in **a** shows the profile of the ferromagnetic domains. [74]

The reminders of this thesis are organized as follows: in Chapter 3, the cross-coupled domain walls in hexagonal $ErMnO_3$ are investigated via the combination of PFM and low temperature MFM, suggesting a strong ME coupling at the boundaries [78]; a milestone work in understanding the bulk ME coupling in hexagonal manganites will be presented in Chapter 4 [74].

Chapter 3

Collective magnetism at multiferroic vortex domain walls

In Section 1.3.3, we have discussed the multiferroic vortex in hexagonal manganites, composed of cyclic interlocked structural antiphase and ferroelectricity domain states, forming a topology-protected defect. Topological defects physics, which have been fruitful playgrounds for emergent phenomena, are pervasive in complex matter such as superfluids, liquid crystals, the Earth's atmosphere, and the early universe [79]. Recently, vortex-like topological defects, called magnetic skyrmions, were observed in helical magnets with broken inversion symmetry [80]. The interplay between the topological spin texture of skyrmions and the spins of conduction electrons may lead to novel spintronic applications. Hexagonal manganites, which possess the cross-coupled lattice charge freedoms and complex magnetic phases, attract great interest in achieving the magnetoelectric coupling. Despite of much exciting progress on the macroscopic magnetoelectric coupling and the 6-state vortex physics, the magnetic nature of the vortices were still unknown. At the antiphase domain boundary, the structural phase shifts atomically sharp [27, 81]. Because the Mn atom carries spins, presumably, the antiferromagnetic Mn^{3+} spins must response to the structural domain boundary, making the multiferroic vortex a coupled charge, lattice, and spin topological defect.

Previous second harmonic generation (SHG) studies suggested that ferroelectric domain walls (DWs) in $YMnO_3$ always pin 180° antiferromagnetic DWs in millimeter size crystals [53]. However, SHG is unable to resolve vortex domain structure due to its spatial resolution limitations ($\sim$10 μm) [53]. Several novel techniques, such as X-ray magnetic linear

dichroism (XMLD) [82], scanning micro-diffraction [83], and spin polarized-scanning tunneling microscopy (SP-STM) [84], are able to visualize antiferromagnetic domains or walls in very limited cases. None of these state-of-the-art are applicable in hexagonal REMnO$_3$, because it is an insulating antiferromagnet with non-collinear commensurate spin structure. XMLD is powerful in detecting orientation domains of collinear antiferromagnets, scanning micro-diffraction can only distinguish domains with different structural modulation wave-vectors, and SP-STM is only applicable for conductive samples. Magnetic force microscopy (MFM) has been widely applied in the data storage industry for its high magnetic sensitivity and nanometer spatial resolution in detect stray field gradient [85]. Advanced MFM has successfully visualized uncompensated moments at the interface of exchange bias systems [86]. As far as we are aware, this is the first report of direct visualization of uncompensated moments in antiferromagnetic domain walls.

3.1   Sample preparations

To correlate the antiferromagnetic domains with the ferroelectric one, cryogenic MFM and PFM measurements need to be performed at exactly the same location. Since the two kinds of images are measured in different microscopes, it is a technical challenge to locate the same spot within nanometer error. Because electric charges accumulate on the bare surface of hexagonal manganites, the resulting electrostatic interaction strongly interferes the magnetic signal detection in MFM. The sample surface is usually coated by a thin gold film ($\approx$ 50 nm), deposited with magnetron sputtering, to screen off the electric field, and the deposition may change the morphology. Fortunately, magnetron sputtering barely introduces extra topographic features. There are several steps to align ambient PFM and cryogenic MFM images: at first, a location (500 μm $\times$ 500 μm) with significant features is chosen, which is visible under optical microscope; then, it is mapped out by approximately 30 PFM images (100 μm $\times$ 100 μm), patched together to form a large topographic and PFM map; third, the surface is coated with thin gold film, and a second topographic map is
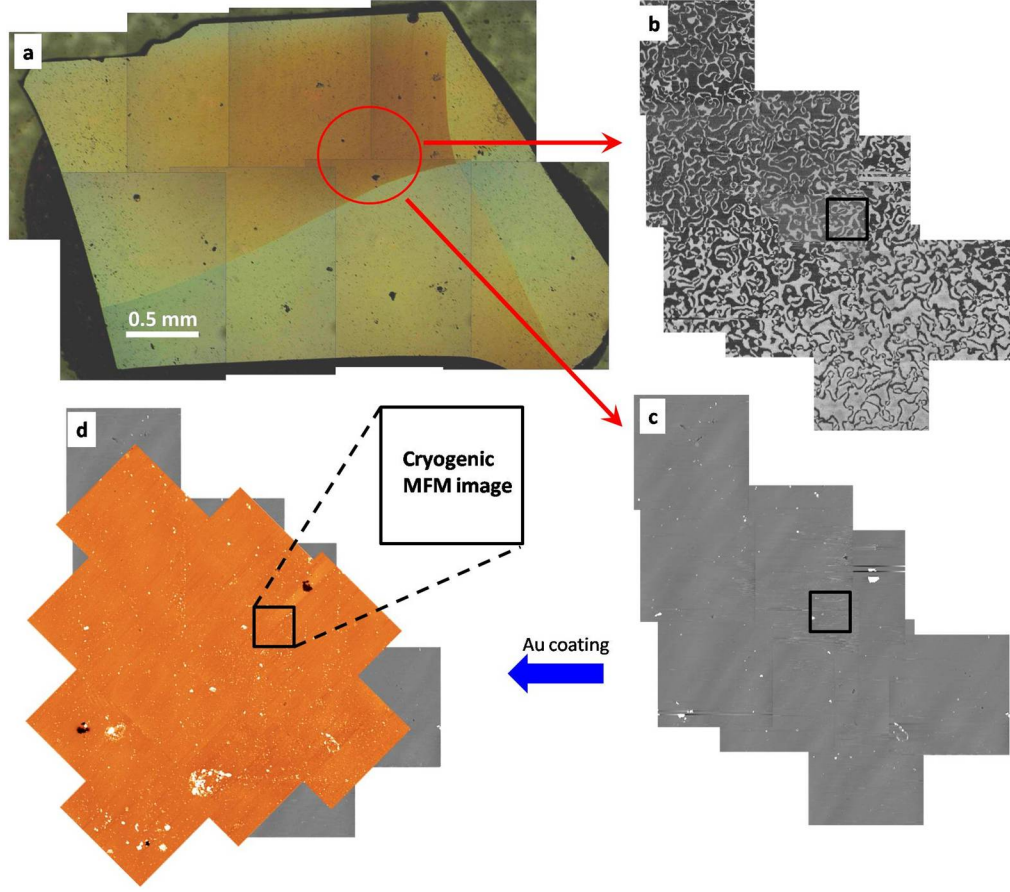
Figure 3.1: Schematic of aligning PFM and MFM images. **a**, optical image of a plate-like ErMnO$_3$ single crystal, the red circle denotes the area of interest with significant feature visible under optical microscope. Several PFM images are patched to cover the area, and the PFM and the same location topo map are shown in **b** and **c**. After depositing gold film, the topographic map is measured again and aligned with previous one (**d**). At last, the topography of cryogenic MFM image (black box) is aligned to the topo map (**d**), and eventually correlates with the same location PFM image.

acquired roughly around the same location, topographic landmarks are used to align the two topographic maps. Finally, the sample is transferred to the cryogenic MFM, and the tip is landed within the 500 μm × 500 μm zone under optical microscope. After that, a 40 μm × 40 μm region (maximum scan area) in cryogenic MFM is compared with the aforementioned large topographic map by aligning the subtle topographic features, and the MFM and PFM measurements at the same location are achieved. The procedure is illustrated in Fig. 3.1.
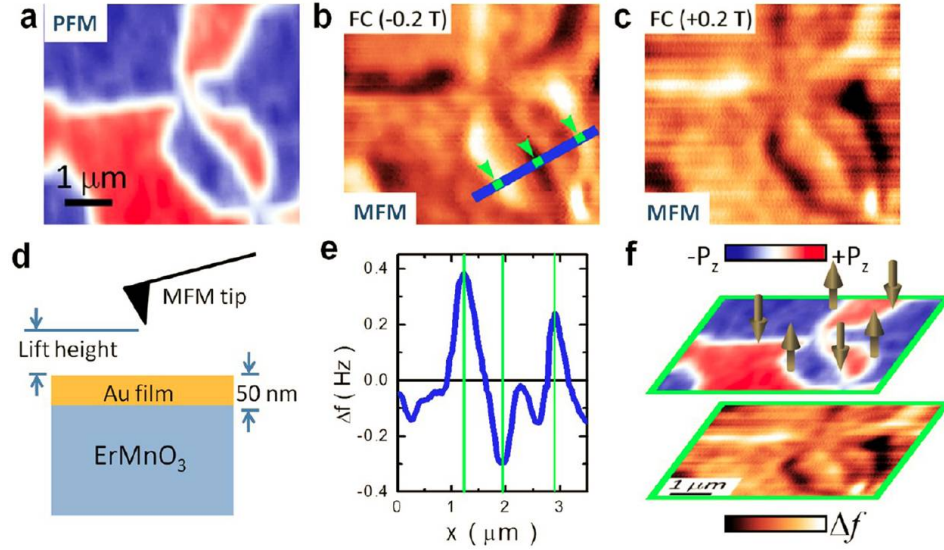
Figure 3.2: **a**, ambient PFM image on the (001) surface of a single crystal hexagonal ErMnO$_3$. The red and blue colors in PFM correspond to up and down polarization domains. **b** (**c**), MFM image measured at 5.5 K in a 0.2 T out-of-plane magnetic field after -0.2 T (+0.2 T) field cooling from 100 K to 5.5 K. The MFM images are taken at the same location as the PFM image. **d**, a cartoon sketch shows the setup of the MFM experiment. **e**, the line profile of the MFM signal along the blue line in **b**, vertical green lines denote the position of the DWs as indicated by the green arrows in **b**. **f**, a perspective view of PFM (**a**) and MFM (**c**) images with brown arrows representing the orientation of the uncompensated magnetic moments at structural antiphase ferroelectric DWs. [78]

3.2 Interlocked ferroelectric and antiferromagnetic domain walls

Room temperature PFM images are taken on the (001) surface of a single crystal hexagonal ErMnO$_3$, shown in Fig. 3.2a, where six alternating up (red) and down (blue) ferroelectric domains merge at a vortex core. The MFM images (Fig. 3.2b, c) are measured at 5.5 K in a 0.2 T out-of-plane magnetic field after field cooling from 100 K ($> T_{\mathrm{N}} \approx 80K$), taken at the same location with the PFM image. Clearly there are line features with alternating bright and dark colors in the MFM images, correlating with the antiphase ferroelectric DWs around the vortex core in the PFM image. Note that the contrast inversion between Fig. 3.2b and 3.2c is due to the reversal of local net moments because the orientation of the MFM tip moment is determined by the external magnetic field (0.2 T $\gg \mu_0 H_c \approx 0.02$ T). The line profile of MFM signal is plotted in Fig. 3.2e, and more line profiles are
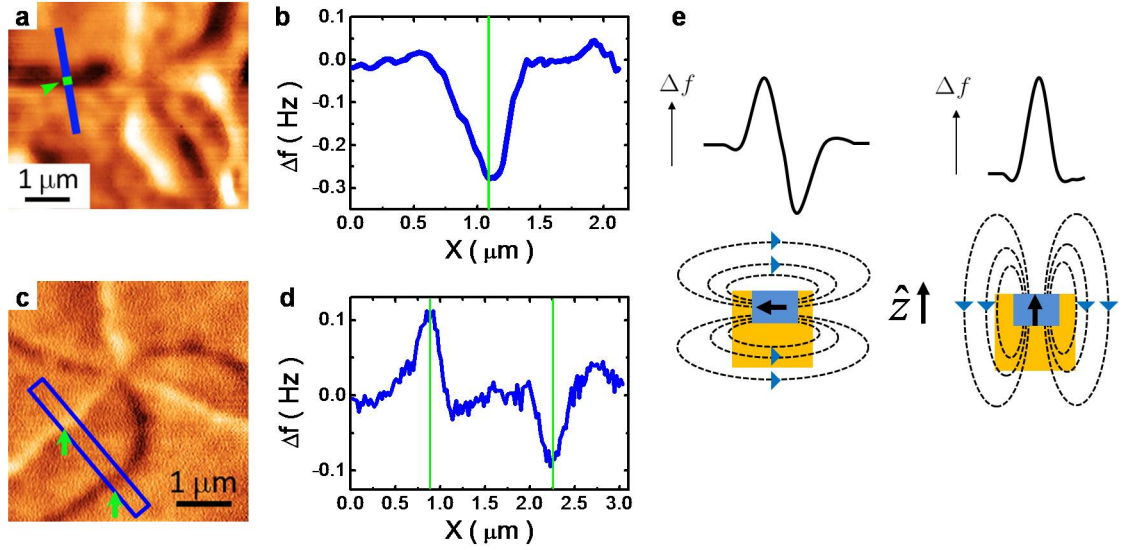
Figure 3.3: **a** and **c**, MFM image of vortices measured at 5.5 K in 0.2 T magnetic field from different samples of the same batch. **b** (**d**), the line profile of MFM signal along the blue line (box) in **a** (**c**). **e**, cartoons of magnetic stray fields and the corresponding MFM line profiles from in-plane and out-of-plane magnetic moments. [78]

shown in Fig. 3.3. Assuming dipole interaction between MFM tip and local net moment, the out-of-plane net moment produces a single peak line profile, while the in-plane one generates an antisymmetric up down line feature, as shown in Fig. 3.3e. Therefore, the MFM signal at DWs originates from local net moments along the c-axis. Since no net moment is expected inside antiferromagnetic domains, the net moments at the DWs must come from the uncompensated moments at the antiferromagnetic DWs which are coupled to the antiphase ferroelectric DWs. The fact that orientation of cooling magnetic field determines the magnetic state of alternating vortex DWs (comparison between Fig. 3.2b and 3.2c) suggests that the DW magnetism is likely a correlated phenomenon, tied to the antiferromagnetic order of the Mn^{3+} spins. Therefore, this results provide compelling evidence that the 6-state vortices in $ErMnO_3$ are truly multiferroic. The perspective PFM and MFM images in Fig. 3.2 reveal that the uncompensated magnetic moments at DWs around a vortex core are parallel to the c-axis with alternating orientation, similar to the alternating ferroelectric polarization of domains around a vortex core.
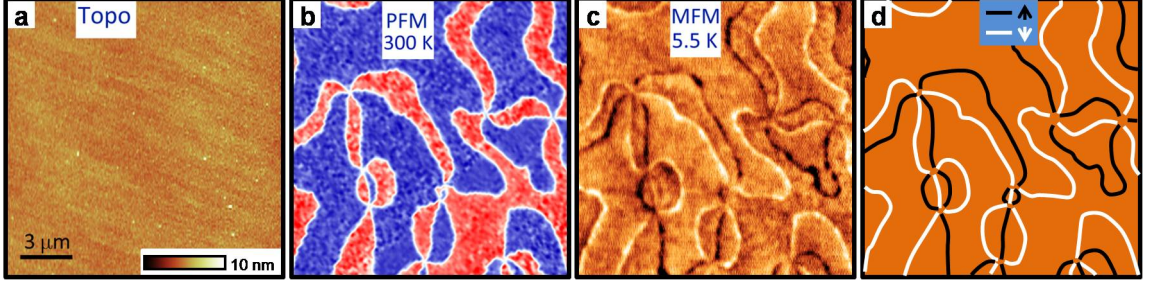
Figure 3.4: **a**, topography, **b**, room-temperature PFM image, and **c**, MFM image taken at the same location on the (001) surface of a $ErMnO_3$ single crystal. **d**, a cartoon sketch of the DW net magnetic moments over the entire field of view based on MFM data of one vortex and the connectivity of vortices in **b**. Black (white) lines represent up (down) net moments. [78]

To determine whether the alternating pattern of DW net magnetic moments is a local property or a global one of the vortex network, the MFM image with maximum scan size (16×16 μm) at 5.5 K is obtained. The alignment between PFM (Fig. 3.4b) and MFM (Fig. 3.4c) images is realized by using topographic features. An illustration of the pattern of DW net moments is showed in the cartoon (Fig. 3.4d), which is based on the vortex connectivity in the PFM and the magnetic pattern of one vortex. Clearly, the DW signals in the MFM image are in excellent agreement with that in the illustration, suggesting that the alternating DW net moments correlate over the entire field of view, possibly over the whole sample, and thus representing a collective phenomenon. The collective magnetism is confirmed at multiple locations on different crystals from the same batch (Fig. 3.5). The finding suggests the existence of two types of magnetic DWs, noted as DW_I and DW_{II}.

The origin of the net moments at the DWs seems puzzling. Previous micromagnetic analysis of 180º antiferromagnetic DWs in hexagonal $YMnO_3$ suggested that oscillatory uncompensated Mn^{3+} spins rotate across the DW in the ab-plane due to in-plane anisotropy, which doesn't account for the observed out-of-plane magnetization. Furthermore, the uncompensated moment from the pure antiferromagnetic Mn^{3+} DWs is too weak to be comparable with the detected signal. Therefore, the observed out-of-plane uncompensated moments likely come from Er^{3+} spins, which generally have out-of-plane anisotropy. To understand
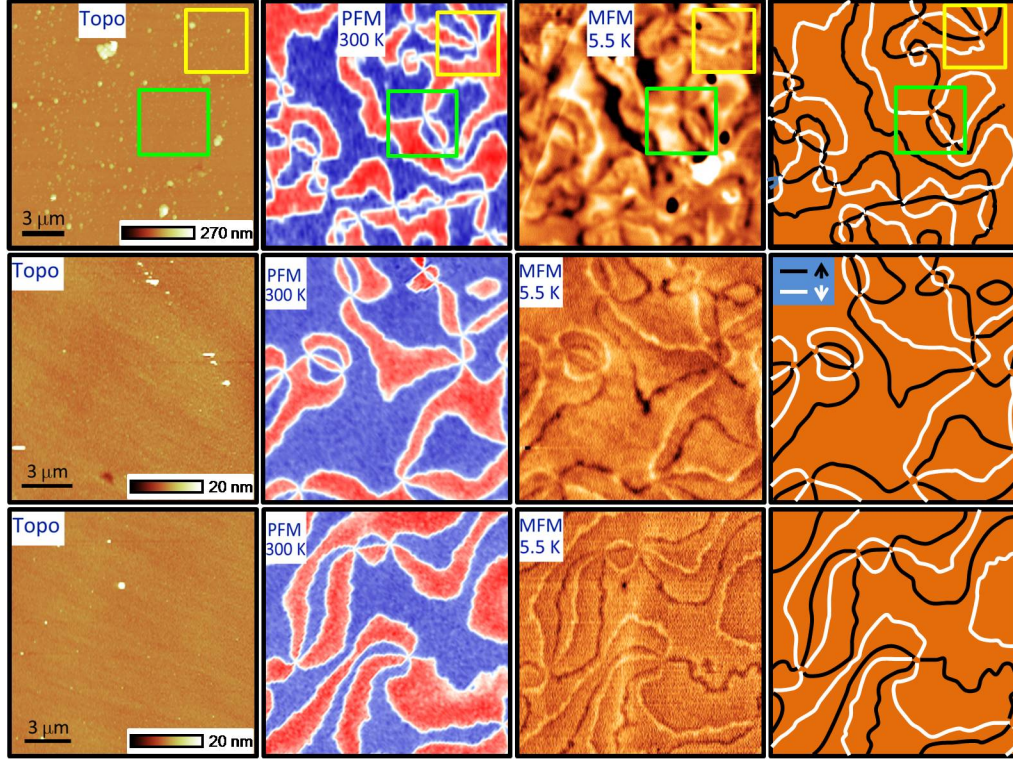
Figure 3.5: The correlation of alternating domain wall net moments over multiple vortex netwroks. [78]

the origin of the DW moments, we studied the temperature dependence of the DW magnetic signal, as shown in Fig. 3.6. The DW contrast, defined as the difference between bright and dark DWs, decreases sharply at low temperature ($<$10 K), then the trend becomes slowly at higher temperatures, which resembles the Curie-Weiss behavior. Note that the behavior is inconsistent with temperature dependence of the Mn^{3+} order parameter (the green dashed line in Fig. 3.6g) [87]. Assuming that the MFM signal is proportional to the DW net moments, a good fit (red solid line) of temperature dependent DW contrast is obtained by using 0 K phenomenological doublet model. In this model, the effective doublet ground state of Er^{3+} ions is split by the exchange fields from neighboring Mn^{3+} spins [36]. Indeed, the DW contrast disappears above 80 K, in excellent agreement with T_N, inferred from the bulk susceptibility data.

The doublet model has been successful in explaining the bulk, i.e., inside domains, partial RE^{3+} ordering in other hexagonal $REMnO_3$, which are examined with X-ray magnetic
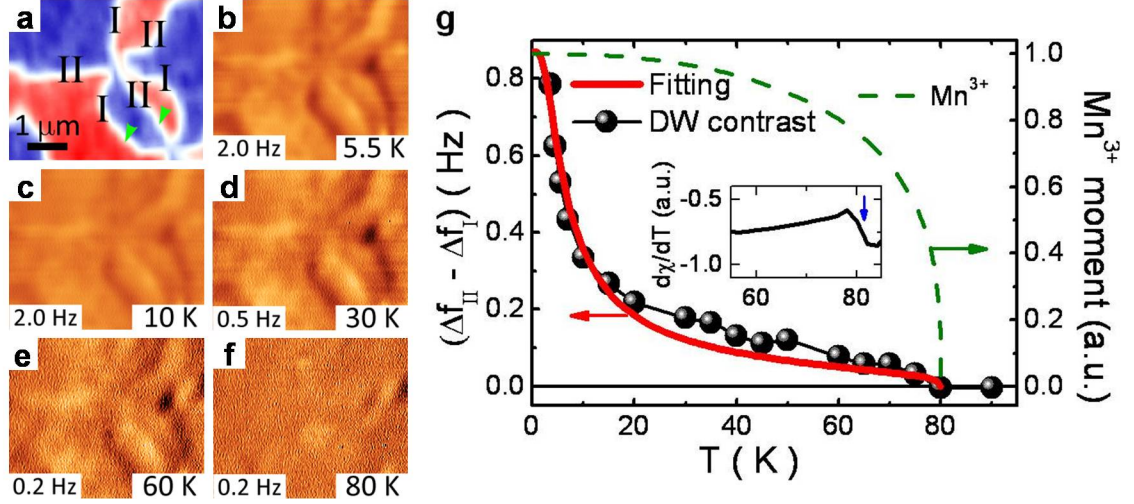
Figure 3.6: **a**, PFM image at the same location as the MFM images, DW_I (DW_{II}) are labeled by "I" ("II"). **b-f**, selected MFM images at various temperatures. The color scales are noted at the left bottom of each image. **g**, temperature dependence of the DW contrast $(\Delta f_{II} - \Delta f_I)$ of two DWs noted by green arrows in **a**. The red curve is a fitting curve based on a phenomenological doublet model. The inset shows the derivative of the DC susceptibility with respect to temperature $d\chi_{DC}/dT$. The green dashed line is the temperature dependence of the Mn^{3+} order parameter moment according to neutron scattering. [78]

resonant scattering, neutron diffraction, and Mössbauer spectroscopy [37, 36, 38]. The characteristic temperature dependence of the RE^{3+} moment in hexagonal $REMnO_3$ is an S-shaped curve described by:

$$m_{\mathrm{RE}}(T) = m_{\mathrm{RE}}(0) \cdot \tanh\frac{\Delta(T)}{2k_B T} \tag{3.1}$$

where $\Delta(T) = \Delta_0 \cdot m_{\mathrm{Mn}}(T)/m_{\mathrm{Mn}}(0)$ is the splitting of the effective doublet due to exchange interactions from the Mn^{3+} 120° antiferromagnetic order moment $m_{\mathrm{Mn}}(T)$ [37, 36, 38]. It acts like the effective field to polarize the Ising-like RE^{3+} spins. The Mn^{3+} ordering data is from neutron scattering $m_{\mathrm{Mn}}(T) = m_{\mathrm{Mn}}(0) \cdot [1 - (T/T_{\mathrm{N}})^d]^e$ with fixed parameters: $d \approx 2.36$, $e \approx 0.31$ [87]. By fitting the temperature dependent DWs contrast, it is obtained that $\Delta_0 = 8.7 \pm 1.5K$, and $T_{\mathrm{N}} = 80 \pm 1K$. The value of Δ_0 is consistent with the values obtained in $HoMnO_3$ (11 K), $YbMnO_3$ (16 K) and $TmMnO_3$ (20 K) from XMRS, neutron scattering and Mössbauer spectroscopy measurements [37, 36, 38]. The good agreement between doublet model and our MFM data suggests the doublet model is applicable for the

DW magnetism as well. Therefore, we propose that the DW net magnetic moments come from uncompensated Er^{3+} spins polarized by the exchange fields from neighboring Mn^{3+} spins.

3.3 Dzyaloshinskii-Moriya interaction
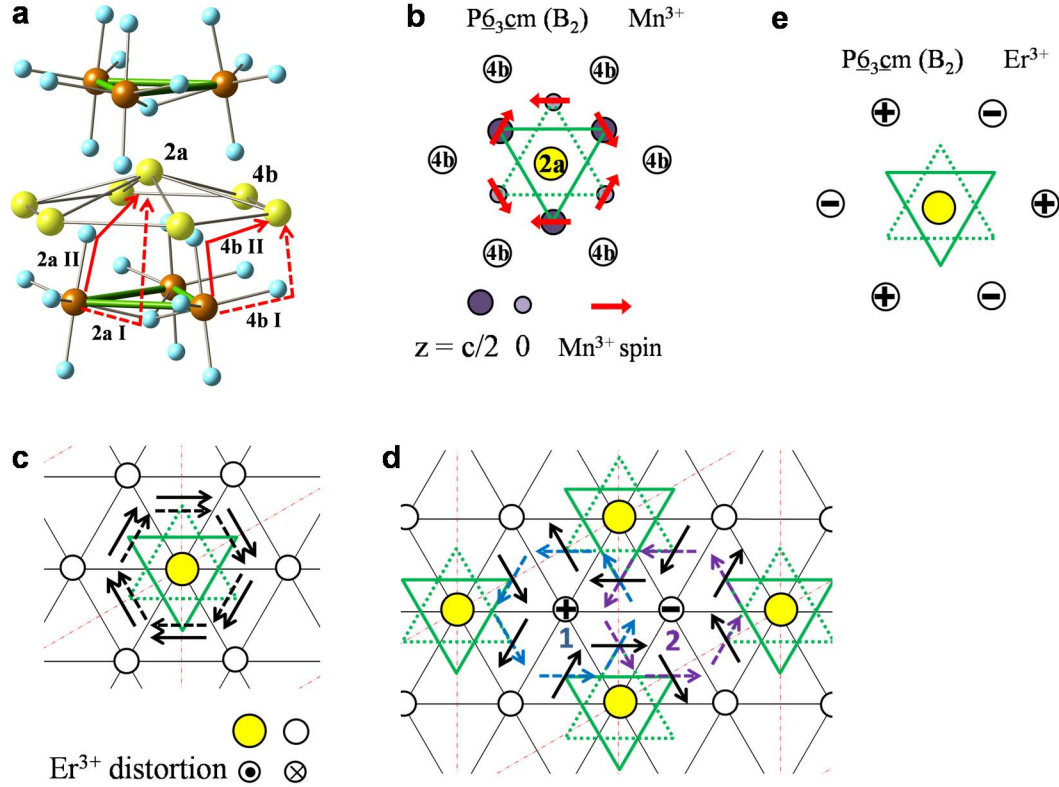
Figure 3.7: **a**, 3D cartoon of hexagonal $ErMnO_3$ structure, where yellow, brown, light blue spheres represent Er^{3+}, Mn^{3+}, O^{2-} ions, respectively. The red lines show the exchange paths at 2a and 4b sites. Path I (II) is defined as interacting through the planar (apical) oxygen, and is noted by a dotted (solid) red arrow. **b**, Mn^{3+} spin configuration of B_2 phase. Solid (dotted) green triangles represent Mn^{3+} trimers at $z = c/2$ ($z = 0$) layer that is above (below) Er^{3+} layer. **c**(**d**), DM vectors and inducted Er^{3+} moments at 2a (4b) site with ferroelectric polarization pointing into paper. The blue and purple dotted arrows represent DM vectors of the exchange path I for site 4b(1) and 4b(2). **e**, the induced Er^{3+} antiferromagnetic order respects B_2 symmetry as well. [78]

It is believed that the effective exchange fields originate from anisotropic exchange interactions, and the antisymmetric components are the well-known Dzyaloshinskii-Moriya (DM) interactions [88, 89]. The presence of DM interactions are the key ingredient for

spiral spin orders, which induce ferroelectricity by breaking inversion symmetry and become multiferroic [2, 4]. In hexagonal $REMnO_3$, the partial RE^{3+} antiferromagnetic order is likely attributed to the DM interactions between RE^{3+} and Mn^{3+} spins, because the dipolar interactions between RE^{3+} and Mn^{3+} are of order of 1 K and thus are too weak to account for the observed coupling strength ($\sim$10 K) [36]. In low magnetic field ($<$1 T), the magnetic space group of Mn^{3+} ordering belongs to P$\underline{6}_3$cm magnetic symmetry, i.e., B_2 in the one-dimensional irreducible representation. The exchange interactions are through the exchange path defined by the red lines, shown in Fig. 3.7a [49, 90]. The exchange interactions are formulated as: $H_{DM} = \sum_i \vec{D}_i \cdot (\vec{\sigma} \times \vec{S}_i) = -\sum_i \vec{\sigma} \cdot (\vec{D}_i \times \vec{S}_i) = -\vec{\sigma} \cdot \vec{H}_{eff}$, where $\vec{D}_i$, $\vec{\sigma}$, $\vec{S}_i$ are the DM vectors, the Er^{3+} spin, and Mn^{3+} spins, respectively. The second equality uses the permutation rule. Therefore, $\vec{H}_{eff} \equiv \sum_i \vec{D}_i \times \vec{S}_i$ is the effective exchange field that polarizes the Er^{3+}. The direction of a DM vector is defined as the rotation axis of the distortion of Mn-O bond from high symmetry position by using the right hand rule.
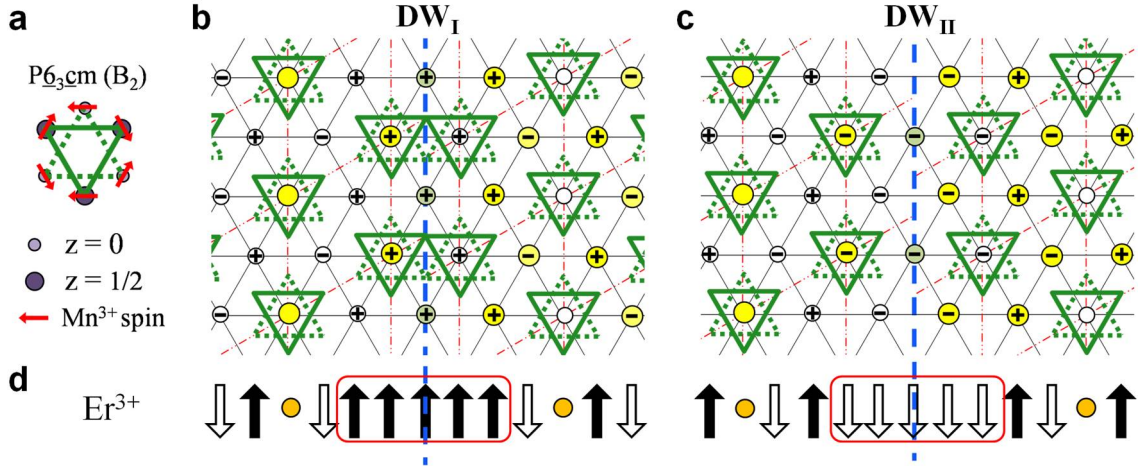
Figure 3.8: Mn^{3+} trimers are denoted by the green triangles at $z = c/2$ (solid) and $z = 0$ (dotted) in **a**. **a** and **a**, the local distortion and spin configuration of Er^{3+} spins in type I and type II DWs, respectively. Yellow (white) circles correspond to ion distorting out of (into) paper. "+" ("-") denotes the induced Er^{3+} moment is out of (into) paper. **a**, illustration of spin configuration near DWs, the arrows inside the red boxes represent uncompensated moments of the DWs. [78]

To provide a simple physical insight of the DW net moments, we propose a simple DW model by making a few very simple assumptions. It has been suggested that there are

two types of interlocked structural antiphase ferroelectric DWs alternating around vortex cores, which may be the structural origin of the two types of magnetic DWs. Assuming atomically sharp Mn^{3+} spin variation at DWs, a single Mn^{3+} spin configuration in domains across DWs, and abrupt structural distortion variation across the two types of DWs, we find opposite uncompensated Er^{3+} moments polarized by DM exchange fields at the two types of DWs. The results of this simple model agree with the observation very well. As shown in the schematic in Fig. 3.8, the uncompensated net moments have opposite orientation across the two different DWs, which quantitatively explains the collective magnetism in the vortex network.

3.4 Landau theory of topological defects in hexagonal manganites
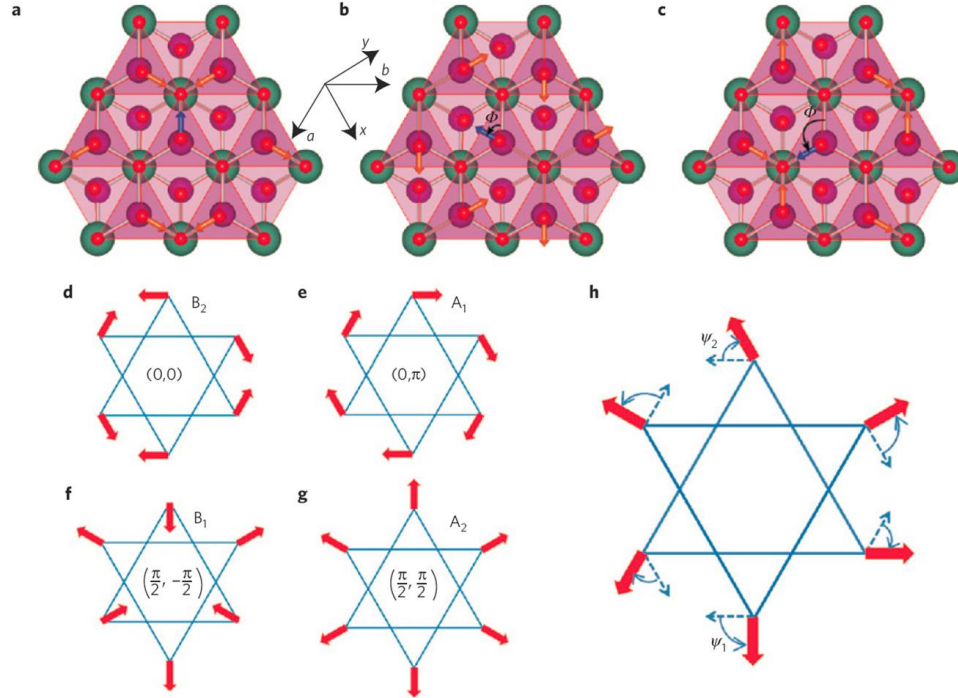
Figure 3.9: **a-c**, displacements of apical oxygen ions on the ab plane in different structural antiphases, denoted by Φ. Shown are the $\alpha+$ with $\Phi = 0$ (**a**), $\gamma-$ with $\Phi = \pi/3$ (**b**), and $\beta+$ with $\Phi = 2\pi/3$ (**c**). **d-g**, four magnetic states with the spin directions indicated by red arrows and the corresponding values of the angles (χ_1, χ_2). **h**, the rotations of spins in DWs are described by ψ_1 and ψ_2. [33]

The doublet model fits the Curie-Weiss-like temperature-dependent DW contrast very

well, suggesting that DW moment likely originates from the out-of-plane RE moment, which is polarized by Mn^{3+} ordering through DM interaction. However, the model cannot explain how the uncompensated moment is produced at the structural boundary, nor explain the alternating magnetism around the vortex core. The above DW scenario can qualitatively explain the collective magnetism by make a few very simple assumptions: two types of alternating structural antiphase domain boundaries and atomically sharp spin variation [78]. A realistic model requires proper consideration of the exchange and anisotropy energies and the symmetries of the order parameters, and the spin rotation near the DWs is more extensible. Later on, a landau theory study of the topological defects in hexagonal manganites, with parameters determined from first-principles calculations, shows that the ferroelectric DWs indeed carry a magnetic moment [33]. The notations of structural antiphase (apical oxygen displacement) Φ, spin rotation angle in DWs ψ, and spin angle relative to local axis anisotropy χ of corresponding magnetic states are described in Fig. 3.9. Because of the strong in-plane Mn-Mn exchange interaction, the neighboring spins remain close to 120º throughout a magnetic domain wall. Moreover, the spins need to be matched with the local in-plane anisotropy axes, they must rotate in the *ab* plane. The out-of-plane canting Mn^{3+} moment is proportional to the spin rotation angle relative to local anisotropy axes, therefore, $\chi_{1,2} = \psi_{1,2} - \Phi$ is defined, and the weak ferromagnetism $\propto \sin\chi_1 + \sin\chi_2$. For example, $(\chi_1, \chi_2) = (0,0)$ corresponds to B_2 state with zero canting moment, while A_2 phase $((\chi_1, \chi_2) = (\pi/2, \pi/2))$ allows weak ferromagnetism [33].

The crystalline symmetry determines the form of the magnetic free-energy density:

$$f(\psi_1, \psi_2, H) = S[(\partial\psi_1)^2 + (\partial\psi_2)^2] + A[\sin^2\chi_1 + \sin^2\chi_2] -$$
$$C_1\cos(\chi_1 + \chi_2) - C_2\cos(\chi_1 - \chi_2) - \frac{1}{2}MH(\sin\chi_1 + \sin\chi_2) \quad (3.2)$$

The last term describes the weak ferromagnetic moment along the *c* axis in the A_2 phase. For the neighbouring antiphase domains, the magnetic structure must respond to the presence of a structural domain wall. At a structural domain wall with $\Delta\Phi = \pi/3$, spin rotates either by
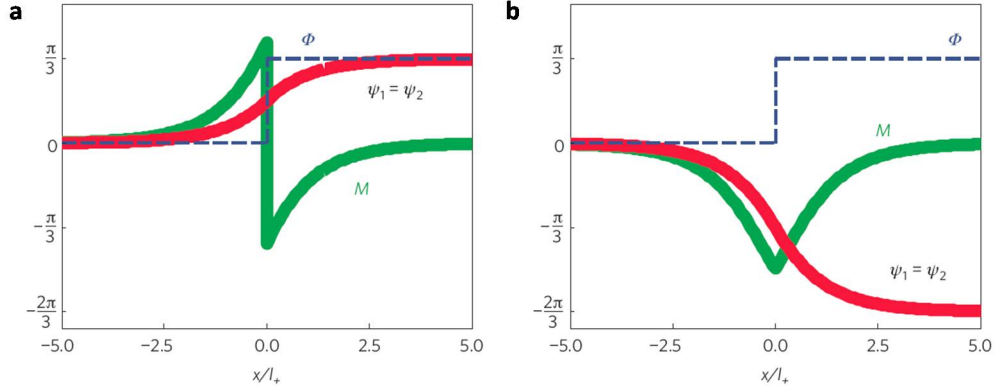
Figure 3.10: **a**, **b**, the variation of the spin rotation angles $\psi_{1,2}$ (solid red), magnetization **M** (solid green), and the trimerization phase Φ (dashed blue) across the domain wall. [33]

$\pi/3$ or $-2\pi/3$, i.e., $\Delta\chi = 0$ or $\Delta\chi = -\pi$. The ground energy states are: $\Delta\psi_1 = \Delta\psi_2 = \pi/3$ and $\Delta\psi_1 = \Delta\psi_2 = -2\pi/3$. The domain wall configuration in Fig. 3.10b, clamped to the structural boundary, carries a non-zero moment along c-axis, which agrees with our observations. Note that the width of the magnetic DWs ($l \sim 5-10$ nm) greatly exceeds that of the atomically sharp structural DWs. The results imply that the winding of structural phase around the vortex core of the structural domains causes a total spin rotation angle along a loop encircling the vortex is 2π or 4π. Therefore, the structural vortices are also magnetic vortices, i.e., multiferroic vortex.

3.5   Magnetic field dependence of the collective magnetism

Our MFM measurement suggests a non-zero magnetization at the DWs, which favors the scenario shown in Fig. 3.10b, i.e., the Mn^{3+} spin rotates by -120° ($\Delta\psi = -2\pi/3$) at the 60° structural boundary ($\Delta\Phi = \pi/3$). When crossing two adjacent DWs, e.g., $\alpha+ \to \beta-$, $\beta- \to \gamma+$, shown in Fig. 3.11, $\Phi = 0 \to -\pi/3 \to -2\pi/3$ (black), $\psi = 0 \to 2\pi/3 \to 4\pi/3$ (red), $\chi = \psi - \Phi = 0 \to \pi \to 2\pi$. As a result, the net moment $M = \sin(\chi)$ (blue) shows opposite sign at neighbouring DWs, which is in excellent agreement with the observed alternating uncompensated moments. The magnetic DWs over the entire sample correlate with each other through the self-organized structural vortex network, eventually form a
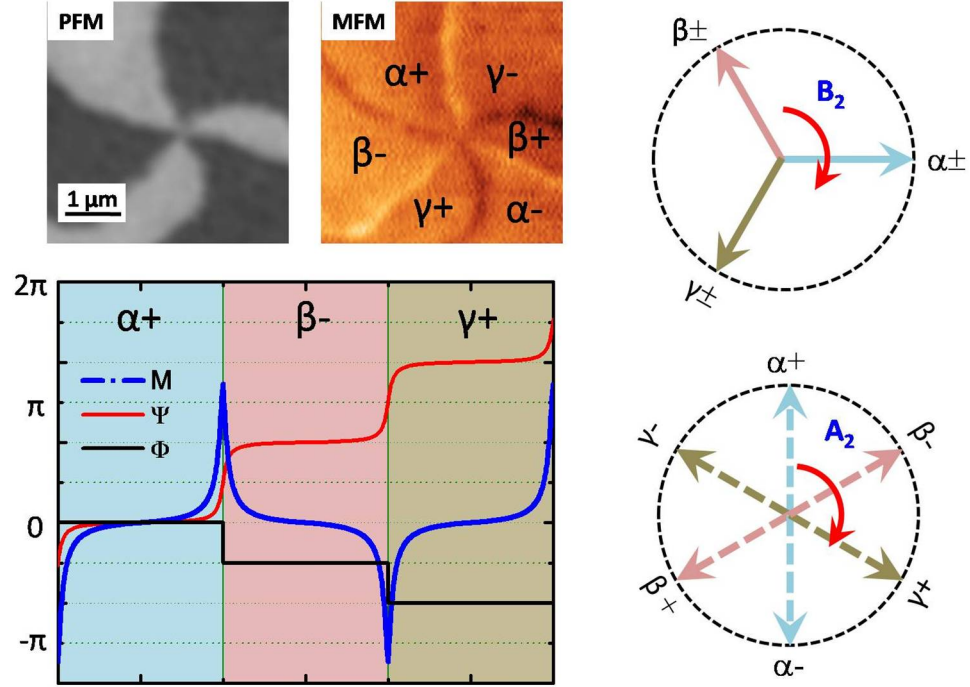
Figure 3.11: The DW moments are simulated for adjacent domains with the Landau theory. On the top, the ambient PFM and 5.0 K MFM images, taken on the same location, show the ferroelectric and magnetic vortex, where the structural antiphases are assigned. The bottom curves illustrate the variations of the structural phase Φ (black), spin rotation angles ψ (red), and the magnetization M (blue) across the two DWs. The right circles denote the spin rotation angles around the vortex core in B_2 and A_2 phase, and the red arrows represent the proceeding orientation of the structural phases.

collective magnetism in the hexagonal manganites, as shown in Fig. 3.4 and 3.5.

Previous studies suggest a B_2 magnetic symmetry at low magnetic field in ErMnO$_3$, and applied high field drives it into A_2 phase through a spin reorientation transition. Given a fixed structural vortex, like $(\alpha+, \beta-, \gamma+, \alpha-, \beta+, \gamma-)$ shown in Fig. 3.11, the increment of the structural phase in the cyclic states is $-\pi/3$ [33]. Defining the anti-clockwise rotation on the phase circle to be positive, the structural phases proceed clockwise (red arrows in Fig. 3.11). In B_2 phase, the spin rotates in opposite way with the local anisotropy axis does, and the angle change by $2\pi/3$ across each boundary. Therefore, the domain spin state has a Z_3 symmetry, that is, it is solely determined by the lattice structural phase, and is irrelevant to the buckling orientation (electric polarization). Considering the upward and downward polar distortions are equivalent at zero magnetic field (B_2), it is expected that

$\pm$ polarization states are degenerate. On the contrary, the spin angles follow the structural phase closely in A_2 symmetry ($\Delta\psi = \Delta\Phi$), i.e., decrease by $\pi/3$ in proceeding the structural phases, as shown in the bottom circle in Fig. 3.11. Because the external magnetic field lifts the degeneration of Mn^{3+} spin ordering for $\pm$ polarization domains, the spin state has a Z_6 symmetry in A_2 phase.
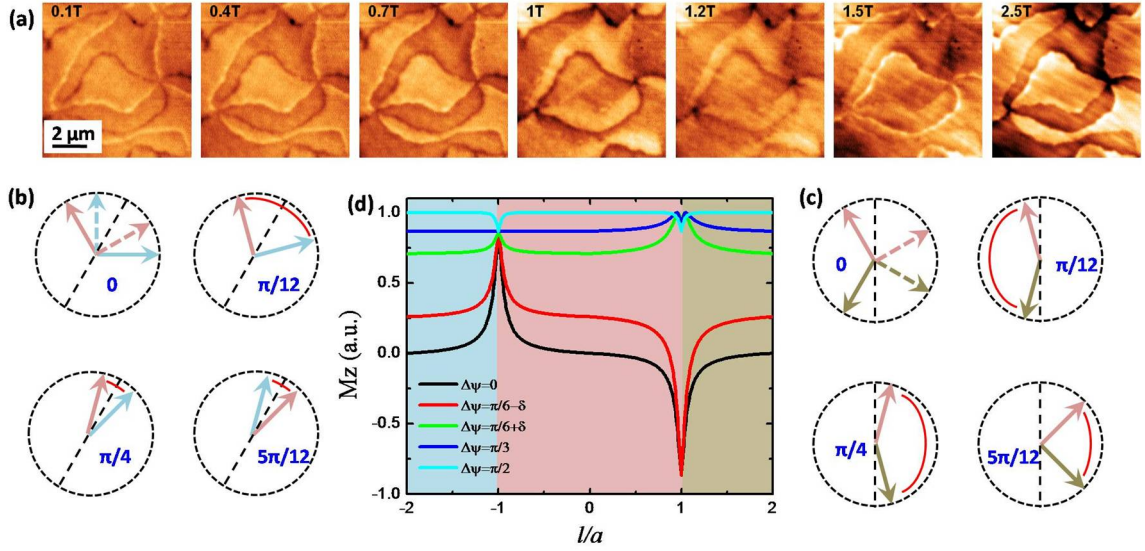
Figure 3.12: **a**, the magnetic field dependent MFM images, taken at 5.0 K, in which the line features correspond to antiferromagnetic DWs. **b** (**c**), the evolution of the spin rotation state in the [$\alpha+$, $\beta-$] ([$\beta-$, $\gamma+$]) DW during the spin reorientation transition. The solid (dotted) arrows denote the spin state of B_2 (A_2) phase, and the red lines illustrate the DW moments. **d**, the simulation of the DW magnetisms at the adjacent structural DWs under various spin rotation angles: 0, $\pi/6 - \delta$, $\pi/6 + \delta$, $\pi/3$, $\pi/2$.

In the spin reorientation transition from B_2 to A_2 phase, the symmetry of Mn^{3+} spins has to change from Z_3 to Z_6. The spin rotations at the DWs, determined by the spin state, produce corresponding DW magnetism, which evolves with the applied magnetic field. Figure 3.12a shows the magnetic field dependent MFM images taken at low temperature (5.0 K). Clearly, it has alternating up and down DW moments at 0.1 T, forming a magnetic vortex network. The strength of the DW magnetism changes with applied magnetic field, and dramatically around transition field point (1.5 T). Qualitative analysis suggests the bright and dark DWs, at 0.1 T, behavior differently: bright DWs firstly dim the contrast, and disappear at 1.0 T, then gradually become bright again at high field; on the contrary,

the dark ones become darker at first, then suddenly turn to bright at 1.5 T. The distinct characters are quantitatively simulated in Fig. 3.12d, where the magnetic DW profiles are plotted under certain spin state. Note that the spins in different domains are assumed to be rotated simultaneously by applied magnetic field. Across the DWs, the rotation of the spins takes the shortest path to connect the spin states in neighbouring domains. For example, for the [$\alpha+$, $\beta-$] DW, as shown in Fig. 3.12b, the $\alpha+$ domain (light blue) and $\beta-$ one (pink) rotate towards each other when increasing magnetic field, causing the DW moment to decrease firstly, disappear (rotate by $\pi/3$), then gradually come back at high magnetic field. In contrast, in the [$\beta-$, $\gamma+$] DW, Fig. 3.12d, the $\beta-$ (pink) and $\gamma+$ (olive) domain rotate oppositely, and become exactly anti phase at $\pi/6$. Therefore, the DW moment has a sharp contrast flip at this point, as shown in the right DW in Fig. 3.12d. The simulations are in good agreement with the MFM observations. The evolutions of the bulk domain spin state, from three-fold states in B_2 phase to six-fold states in A_2 phase, cause the change of DWs magnetism, the degeneration of the two types of DWs is lifted to accommodate the symmetry change of bulk domain states. The study of DWs magnetism provides an indirect way to probe the domain spin state based on the magnetic field dependence of DW moments.

Chapter 4

Bulk linear ME effect in hexagonal manganites

The coupling between the magnetic and electric dipoles in multiferroic and magnetoelectric materials holds promise for conceptually novel electronic devices. The revival of magneto-electricity in the past decade has been fuelled by the discoveries of new multiferroic materials exhibiting giant magnetoelectric effects due to the cross-coupling between coexisting ferro-electric and magnetic orders. Recently, the quantized magnetoelectric polarizability has been proposed to classify three-dimensional topological insulators in the presence of strong correlations [91, 92]. Therefore, the ME effect has a profound and broad impact on di-verse areas of materials science. As introduced in Section 1.3, the $REMnO_3$ compounds are improper ferroelectrics in which the polarization P is induced by a structural instability called the trimerization mode Q_{K_3} that condenses at $T_C \sim 1300 - 1500$ K [30, 31, 32, 33]. The Mn^{3+} spins form a 120° non-collinear antiferromagnetic order L in the crystallographic xy-plane below the Neel temperature ($T_N \approx 70 \sim 90$ K). The nonlinear coupling between P and Q_{K_3} modes results in six-state topological vortices with interlocked ferroelectric and structural antiphase domain walls, where a net magnetization was discovered at the domain walls of $ErMnO_3$ [78]. Its appearance is a direct manifestation of a strong and non-trivial bulk coupling of L, P, and Q_{K_3} within each domain, forming a collective magnetism in the entire network, as discussed in Chapter 3. The same coupling can give rise to a bulk linear ME effect if the magnetic structure of the domain wall could be realized throughout the domains. This is possible to do by applying a strong magnetic field H, inducing a spin reorientation transition from the B_2 to the A_2 phase. Our MeFM technique allows, for the first time, a direct visualization of the resulting ME domains, which will be discussed in the

subsequent sections.

4.1   Direct visualization of magnetoelectric domains in ErMnO$_3$
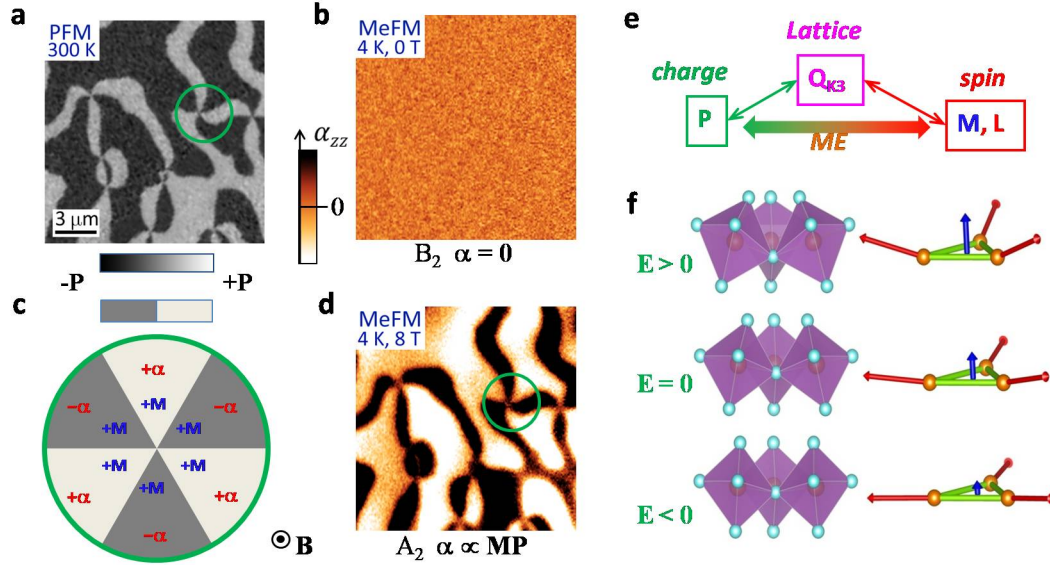
Figure 4.1: Room temperature PFM image (**a**), and 4.0 K MeFM images at zero magnetic field (**b**) and 8.0 T (**d**), are taken at the same location on the (001) surface of a ErMnO$_3$ single crystal. The white (dark) color in **a** represents an up (down) ferroelectric domain. **c**, a cartoon of the ME coefficient α_{zz} of A$_2$ phase in different ferroelectric domains in hexagonal ErMnO$_3$. **e**, a cartoon illustration of the effective ME coupling through structural instability trimerization. **f**, cartoon illustrations of the changes of the buckling of MnO$_5$ polyhedra (trimer mode Q_{K_3}) induced by E-fields through P resulting in the changes of the canting moment M of Mn^{3+} spins. [74]

To investigate the ME response for different ferroelectric domains, the PFM and MeFM images are taken at the same location. Following the same procedure with that of aligning PFM and MFM images, shown in Fig. 3.1, we firstly performed the PFM measurement on the bare surface of a hexagonal ErMnO$_3$ single crystal and capture the topography and PFM maps, then the sample surface is coated with thin gold film to eliminate electrostatic interaction in MFM and MeFM measurements, in the end, MFM and MeFM images are aligned to PFM one through topographic landmarks. The ferroelectric domain pattern is shown in Fig. 4.1a, where the network of six-fold vortex structure is present. Note that the bright (dark) color corresponds to up (down) polarization domains. In zero magnetic

field, the Mn^{3+} spins order in a 120° pattern with magnetic symmetry $P\underline{6}_3\underline{c}m$ (B_2), which falls into the magnetic point group $\underline{6}mm$. Based on the ME tensor table in Fig. 1.3, no linear ME effect is allowed in this group. Consistently, no MeFM contrast is observed in zero magnetic field at 4.0 K (Fig. 4.1) with $E = 10$ kV/cm. The spin configuration of the hexagonal manganites can be controlled with the application of a magnetic field along the z axis. In a large magnetic field, hexagonal $ErMnO_3$ is in the $P6_3\underline{cm}$ phase (A_2) [49], where the notations of spin configuration are described in Fig. 3.9. A_2 symmetry belongs to the point group $6\underline{mm}$, category #14 in Fig. 1.3, which allows non-zero diagonal components, and $\alpha_{xx} = \alpha_{yy} \neq \alpha_{zz}$. In the A_2 phase, the in-plane Mn^{3+} spins rotate through 90° from that of the B_2 phase, resulting in a net magnetic moment (M_z) along the z axis due to the canting of the Mn^{3+} spins. We, indeed, observe a sharp MeFM contrast (Fig. 4.1d) in 8.0 T at 4.0 K with $E = 10$ kV/cm. The sign of the MeFM signal changes at ferroelectric domain walls, that is, the ME domain pattern is identical to the ferroelectric one. The relations among α, P, and canted moment M_z are summarized in Fig. 4.1c. The canting moments point to the same orientation due to the applied strong magnetic field, while the polarizations alternate around the center, suggesting $\alpha_{zz} \propto M_z P_z$.

Several control experiments are performed in hexagonal $ErMnO_3$ to confirm the relation $\alpha_{zz} \propto M_z P_z$. Similar MeFM results on $ErMnO_3$ single crystals with stripe domain pattern are shown in Fig. 4.2a-d. This demonstrates that the ME effect and the clamping of ferroelectric, structural antiphase and antiferromagnetic orders in $ErMnO_3$ are independent of domain structures. Furthermore, in the presence of opposite magnetic field, the canted moment M_z is reversed, resulting in opposite α_{zz} in Fig. 4.2e and Fig. 4.2f. At the same time, the direction of the MFM tip moment M_{tip} follows that of applied magnetic field, and the image contrast is proportional to the product of M_{tip} and local magnetization ΔM. Hence, the image contrast are identical for opposite magnetic fields, as shown in the +4 T and -4 T MeFM images. Note that, in the cartoon Fig. 4.2e and f, M_z originates from the static canted magnetization, while MeFM signal only contains the induced magnetization
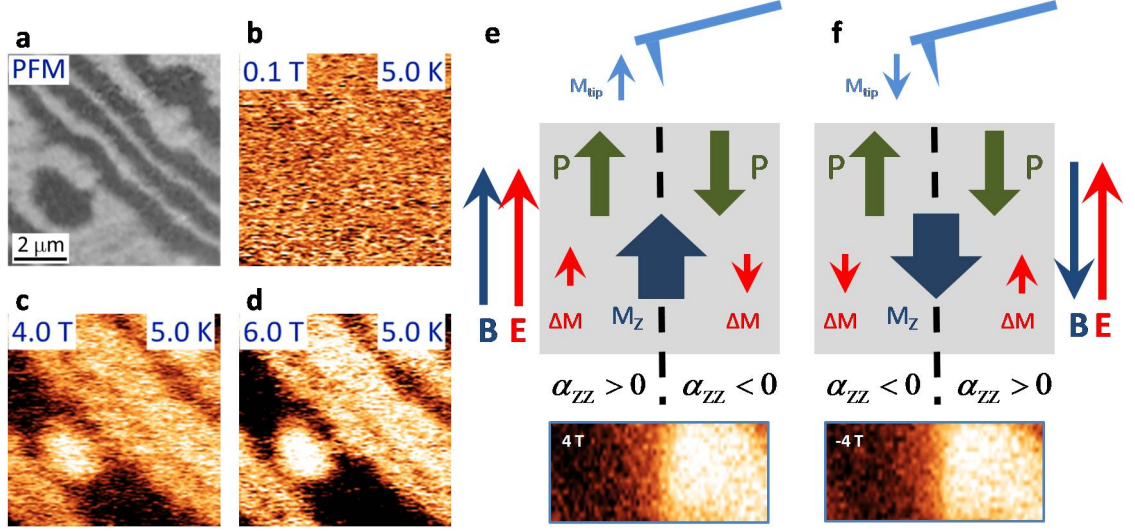
Figure 4.2: **a-d**, room temperature PFM image of the (001) surface of a ErMnO$_3$ single crystal with stripe domain pattern. **b-d**, low temperature MeFM images, same location with **a**, are taken at 0.1, 4.0 and 6.0 T. **e-f**, cartoons show the MeFM images in opposite magnetic fields. [74]

ΔM.

In the A$_2$ phase, the canting moment originates from anisotropic exchange interactions between neighbouring Mn^{3+} spins [55], the same interaction also accounts for the uncompensated DW moment as discussed in Chapter 3. A symmetry analysis, based on the phenomenological Landau free energy expansion, shows that $M_z \propto L_{A_2} \cdot Q_{K_3}$, where L_{A_2} is the magnetic order parameter describing the symmetry of the A$_2$ phase [33]. Figure 4.3 shows the symmetry transformations of the allowed linear magnetoelectric term $f_{\mathrm{ME}} \propto \cos(3\Phi) L_{A_2} H_z E_z$ in the Landau free energy expansion under the generators of the $P6_3/mmc1'$ space group of hexagonal manganites. Here, S_a denotes translation, 3_c is three-fold rotation, $\tilde{2}_c$ is two-fold screw rotation, m_{a+b} is mirror plane $(-y, x, z)$, I is spatial inversion, T is time reversal. Note that $\chi = \psi - \Phi$ denotes the Mn^{3+} spin rotation angle relative to the local anisotropy coordinates, while $\sin(\chi_1) + \sin(\chi_2)$ represents L_{A_2} order parameters and the canting moment. L_{A_2} is the magnetic order parameter describing the symmetry of the A$_2$ phase, formally defined as $L_{A_2} \equiv \frac{1}{N} \sum_i S_i \cdot n_i$, where n_i is the unit vector in the spin direction on the ith Mn site, S_i is the average spin on the site i and N is

	S_a	3_c	$\tilde{2}_c$	m_{a+b}	I	T
$E_z H_z$	$+$	$+$	$+$	$-$	$-$	$-$
$P_z\big|_{E_z=0} \propto Q_{K_3} \cos 3\Phi$	$+$	$+$	$+$	$+$	$-$	$+$
$\chi_1 = \psi_1 - \Phi$	χ_1	χ_1	$\pi - \chi_2$	$-\chi_1$	$-\chi_2 - \pi$	$\chi_1 + \pi$
$\chi_2 = \psi_2 - \Phi$	χ_2	χ_2	$\pi - \chi_1$	$-\chi_2$	$-\chi_1 - \pi$	$\chi_2 + \pi$
$M_z \propto \mathbf{L}_{A_2} \cdot \mathbf{Q}_{K_3}$ $\propto \left(\sin \chi_1 + \sin \chi_2 \right)$	$+$	$+$	$+$	$-$	$+$	$-$
$\cos\left(3\Phi\right) L_{A_2} H_z E_z$	$+$	$+$	$+$	$+$	$+$	$+$

Figure 4.3: The notations are consistent with Fig. 3.9. In particular, $\Phi_{1,2}$, $\psi_{1,2}$ denotes the rotation of the MnO$_5$ polyhedral, i.e., structural trimerization phase, and the spin rotations angles, respectively. The first row in the table corresponds to the generators of the $P6_3/mmc1'$ space group of hexagonal manganites. $+$ (-) represents that certain property is (not) conserved under the symmetry operation. [74]

the total number of Mn sites. For $T \ll T_N$, the A$_2$ magnetic ordering parameter is reduced to $L_{A_2} = \frac{1}{2}L(\sin \chi_1 + \sin \chi_2)$, where L is the magnitude of the 120° spin ordering in the Mn layers, and the order parameter of B$_2$ phase is $L_{B_2} = \frac{1}{2}L(\cos \chi_1 + \cos \chi_2)$. As shown in Fig. 4.3, the term $\cos(3\Phi)L_{A_2}H_zE_z$ in free energy expansion is invariant under all the generators of the $P6_3/mmc1'$ space group. Therefore, the allowed linear ME coupling in A$_2$ phase is:

$$\alpha_{zz} = -\frac{\partial^2 f_{ME}}{\partial E_z \partial H_z} \propto \cos(3\Phi)L_{A_2} \propto P_z M_z \tag{4.1}$$

that is, linear ME coefficient of the A$_2$ phase is proportional to the product of the canting moment and the polarization, which is consistent with our MeFM observations.

4.2 Lattice-mediated ME coupling mechanism

More elaborate theory, combing first-principles calculations, group theory, and microscopic spin models, shows that the trimerization mode Q_{K_3}, acting as the mediator, induces the bulk linear ME effect in hexagonal manganites [74, 55]. Simply speaking, the trimer distortion not only induces a polarization, but also induce a weak ferromagnetism. On one hand,
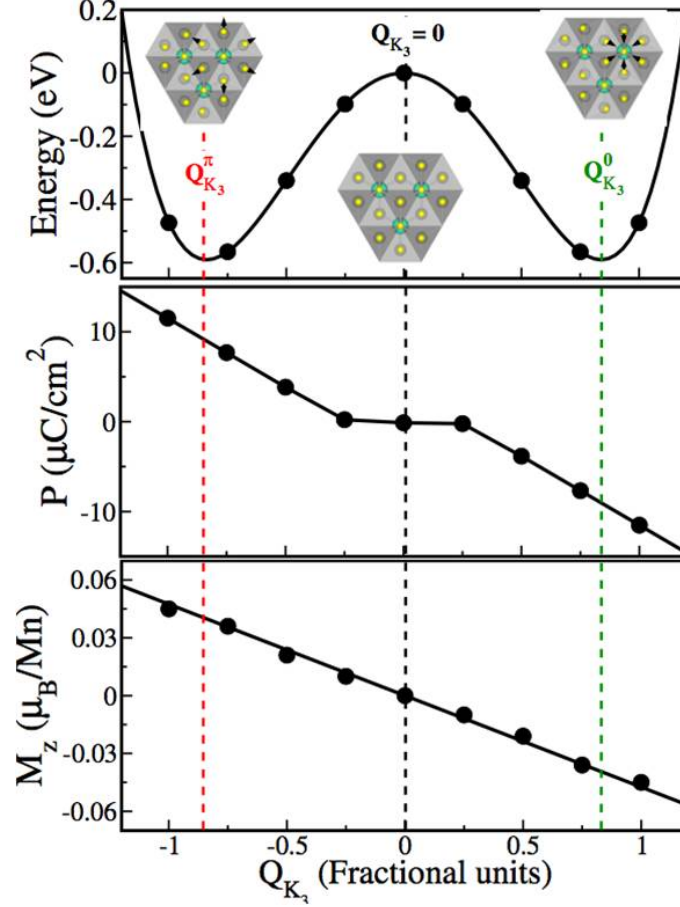
Figure 4.4: **a**, the energy (per unit cell), **b**, electric polarization P, and **c**, the canting moment per formula unit, are calculated with first-principles as a function of the amplitude of trimer distortion Q_{K_3}. [74, 55]

the buckling of the MnO_5 trimer determines the electric polarization linearly. The ferro-electricity flips sign when the trimer distorts oppositely. On the other hand, a out-of-plane weak ferromagnetism, arising from the canting Mn^{3+} spins, couples to the Q_{K_3} mode due to DM interaction [89, 18]. Therefore, applied external electric field changes the polarization, causing the change of the MnO_5 buckling, which finally changes the out-of-plane canting moment [74, 55]. To clarify the origin of the diagonal linear ME susceptibility α_{zz}, the phenomenological Landau free energy is expanded with respect to P, Q_{K_3}, and Φ, and the invariant linear ME term $f_H = -cL_{A_2}Q_{K_3}H_z$, last row in Fig. 4.3, and the interaction with

the applied electric field $f_{\mathrm{E}} = -P_z E_z$ are included:

$$f = f_0 + f_{\mathrm{H}} + f_{\mathrm{E}} = \frac{1}{2} a_Q Q_{K_3}^2 + \frac{1}{4} b_Q Q_{K_3}^4 + \frac{1}{2} a_P P_z^2 + d_{13} P_z Q_{K_3}^3 \cos 3\Phi + \frac{1}{2} d_{22} P_z^2 Q_{K_3}^2$$

$$- c L_{A_2} Q_{K_3} H_z - P_z E_z \quad (4.2)$$

The equilibrium magnetization is then given by

$$M_z \equiv -\frac{\partial f}{\partial H_z} = c L_{A_2} Q_{K_3} \quad (4.3)$$

In the A_2 phase the in-plane components of spins are rigid ($\chi_1 = \chi_2 = \frac{\pi}{2}$), so that $L_{A_2} = L$ and $M_z = c L Q_{K_3}$ for weak electric field. The linear ME susceptibility is then,

$$\alpha_{zz} \equiv \frac{\partial M_z}{\partial E_z} \big|_{E_z=0} = c L_{A_2} \frac{\partial Q_{K_3}}{\partial E_z} \big|_{E_z=0} \quad (4.4)$$

We note that the electric field dependence of magnetic ordering ($\partial L / \partial E_z$) cannot be neglected in the spin reorientation region, where it results in large anomalous magnetoelectric response. However, the anomalous contribution vanishes in the A_2 phase.

To find out the electric field dependence of Q_{K_3}, we minimize free energy with respect to Q_{K_3} and P_z, and differentiate the coupled equations for these two order parameters with respect to E_z at $E_z = 0$, which gives

$$\frac{\partial Q_{K_3}}{\partial E_z} \big|_{E_z=0} = \frac{d_{13} \cos 3\Phi}{d_{22}} \cdot \frac{1}{2a} \quad (4.5)$$

where $a = a_Q - \frac{d_{13}^2}{2d_{22}^2} a_P \approx a_Q$. In this derivation we implement the approximation $d_{22} Q_{K_3}^2 \ll a_P$. Therefore,

$$\alpha_{zz} = c L \cdot \frac{d_{13} \cos 3\Phi}{d_{22}} \cdot \frac{1}{2a_Q} \quad (4.6)$$

Here $\cos 3\Phi$ determines the sign of α_{zz} in structural antiphase domains. Since $P_z \approx -\frac{d_{13}}{d_{22}} Q_{K_3} \cos 3\Phi$, the sign of α_{zz} follows that of P_z [32]. This result can also be derived by integrating out Q_{K_3} and P_z to obtain an explicit expression of free energy $f(E_z, H_z)$, which would naturally contain the corresponding free energy term $-\alpha_{zz} E_z H_z$.

To quantitatively estimate the magnitude of α_{zz} in hexagonal ErMnO$_3$, the parameters in Eq. 4.6 need to be estimated from first-principles calculations. Note that $c L = \frac{\partial M_z}{\partial Q_{K_3}}$

and $\frac{d_{13}}{d_{22}} = \frac{\partial P_z}{\partial Q_{K_3}}$ lead to $|\alpha_{zz}| = \left| \frac{1}{2a_Q} \cdot \frac{\partial M_z}{\partial Q_{K_3}} \cdot \frac{\partial P_z}{\partial Q_{K_3}} \right|$. The parameter a_Q and the slopes $\partial M_z/\partial Q_{K_3}$ and $\partial P_z/\partial Q_{K_3}$ are extracted from first-principles calculations. Here we consider the high temperature $P6_3/mmc$ structure with the A_2 magnetic ordering and freezing-in the zone boundary K_3 mode. The total energy per unit cell, polarization, and canting magnetization are computed as a function of the amplitude of the K_3 mode, as shown in Fig. 4.4. The energy landscape is well fitted with the phenomenological Landau free energy expansion $f_0 = \frac{1}{2}a_Q Q_{K_3}^2 + \frac{1}{4}b_Q Q_{K_3}^4$, in which $a_Q = -3.5\text{eV}/\text{Å}^2/(\text{u.c.})$ and $b_Q = 5.78\text{eV}/\text{Å}^4/(\text{u.c.})$, with energy minimum at $Q_{K_3}^{\min} \approx 0.778\text{Å}$. Therefore, we obtained values of the slopes, at the energy minimum position, $\partial P_z/\partial Q_{K_3} \approx -18.3\mu\text{C}/\text{cm}^2/\text{Å}$ and $\partial M_z/\partial Q_{K_3} \approx -0.062\mu_\text{B}/\text{f.u.}/\text{Å}$ from the linear part of the $P_z(Q_{K_3})$ and $M_z(Q_{K_3})$ curves, respectively. In the end, we obtain the theoretical estimation of the $\alpha_{zz} = 0.7\text{ps/m}$. The trimer mode Q_{K_3} mediates an effective cross-coupling between P_z and M_z (L_{A_2}), that is, the linear magentoelectric effect. Qualitatively, the electric field induces changes of trimerization mode, through electric polarization, leading to changes of canting moment M_z. The excellent agreement between the experimental observations and the microscopic model provides compelling evidence for the fundamental mechanism of lattice-mediated magnetoelectric couplings, which may be generalized to other materials.

4.3 Critical fluctuation induced divergent ME susceptibility in ErMnO$_3$

More interestingly, our systematic MeFM studies at various temperatures (2.8-10 K) and magnetic fields (0-8 T) reveal a giant enhancement of the magnetoelectric effect. Figure 4.5 shows the complete data set of MeFM measurements at 2.8 K in various magnetic fields. Overall, the MeFM contrast increases with increasing magnetic field. Surprisingly, the contrast is strongest at ~ 1.4 T (Fig. 4.5l), indicating a non-monotonic field dependence of the linear ME effect. More quantitative information can be obtained by plotting the MeFM contrast, defined as the difference between neighbouring domain, as a function of $\mu_0 H$ measured at various temperatures (2.8, 4.0, 5.2, and 10 K), as shown in Fig. 4.6. The
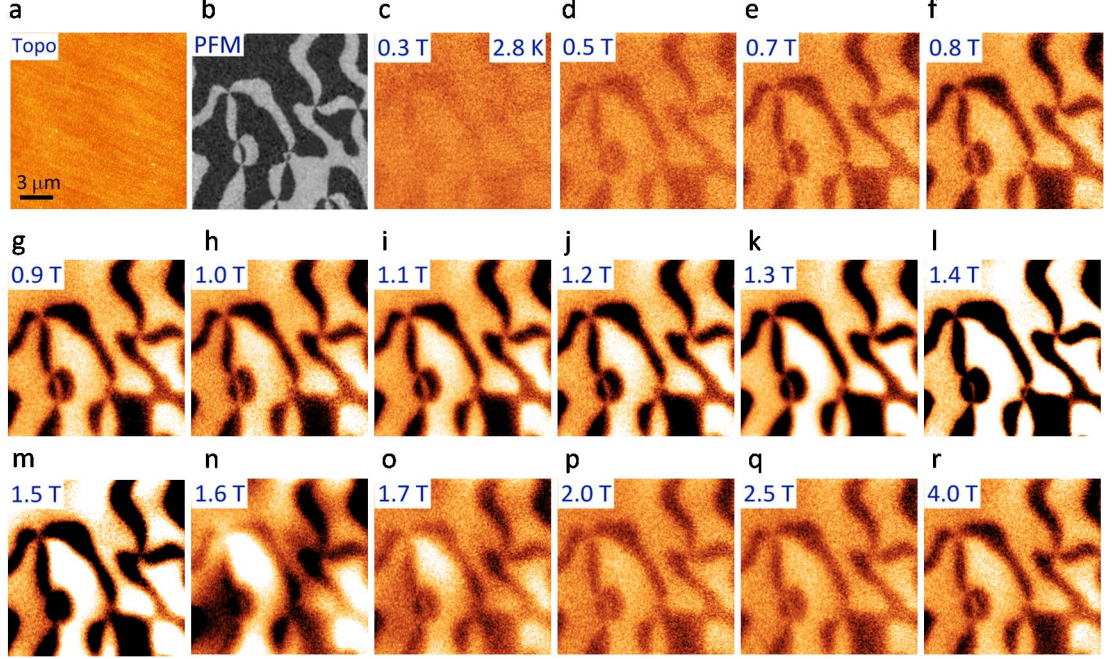
Figure 4.5: **a**, topography of the scanned area, **b**, PFM image, and **c-r**, MeFM images of the same location in various magnetic fields (0.3-4.0 T). The color scale is 10 nm (38 mHz) for topography (MeFM) images. [74]

H-dependence of MeFM data can be approximately divided into three different intervals: high field A_2 region, low field ($0 < \mu_0 H < 1$ T) B_2 region and the intermediate field A'_2 region, which will be discussed separately.

4.3.1 Nonlinear ME response in A_2 phase

In the A_2 phase, the MeFM signal is approximately T-independent below 10 K. Note that the A_2 phase threshold field point varies for different temperatures, for instance, A_2 phase emerges since 2.0 T at 4.0 K, while at 10 K, it starts from ~ 4 T. It turns out that all the high-field data points in A_2 region collapse to a single curve described by MeFM$(H) = a + c \cdot (\mu_0 H)^2$ (solid line in Fig. 4.6). This is consistent with the A_2 magnetic symmetry and the saturation of both Mn^{3+} and Er^{3+} ordered moments at $T \ll T_N (\sim 80K)$. Here the intercept (a) is proportional to α_{zz} originating from the $L_{A_2}E_zH_z$ term in the free energy expansion, which is discussed in previous section. The second part is the nonlinear
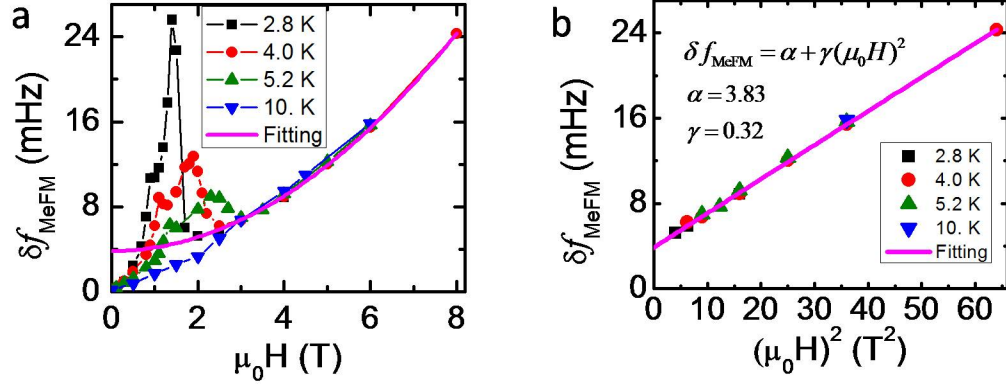
Figure 4.6: **a**, H-dependence of the MeFM signal at 2.8, 4.0, 5.2, and 10 K. The solid curve (magenta) is the polynomial fitting $\text{MeFM}(H) = a + c \cdot (\mu_0 H)^2$ of the high-field A_2 phase with extrapolation to zero field. The intercept a of the fitting curve corresponds to the linear ME effect in the A_2 phase. **b**, MeFM contrast versus H^2 of the MeFM(H) data in the high field A_2 phase to demonstrate the H^2 dependence is independent of temperature below 10 K. [74]

ME effect due to the $L_{A_2} E_z H_z^3$ term in free energy. This behavior is more apparent when plotting the MeFM signal versus H^2, shown in Fig. 4.6b, suggesting that the linear ME effect dominates at low fields, whereas the nonlinear one prevails at high magnetic fields. Based on the MeFM signal estimation in Chapter 2, the measured linear ME effect ~ 13 ps/m, which is in reasonable agreement with that estimated from first-principles calibrations (~ 0.7 ps/m), refer to Section 4.2 for details, where only the contribution of Mn^{3+} spins is taken into account [55]. This indicates that the strong spin-orbital coupling from rare-earth elements may enhance α_{zz} in the A_2 phase. Our results are also consistent with the previous macroscopic ME measurements ($\alpha_{zz} \sim 3$ps/m) on the partially poled $ErMnO_3$ single crystals [93].

4.3.2 Paramagnetic-like ME effect in B_2 phase

In the B_2 region, in particular at low field, the MeFM data collapses to a single curve with the H/T scaling, $\text{MeFM}(H) = b \cdot (\mu_0 H)$, corresponding to the $E_z H_z^2$ term in the free energy. As discussed in Chapter 3, the Dzyaloshinskii-Moriya (DM) interactions between the Mn^{3+} and Er^{3+} spins provide an effective exchange field to polarize the rare earth spins. For B_2
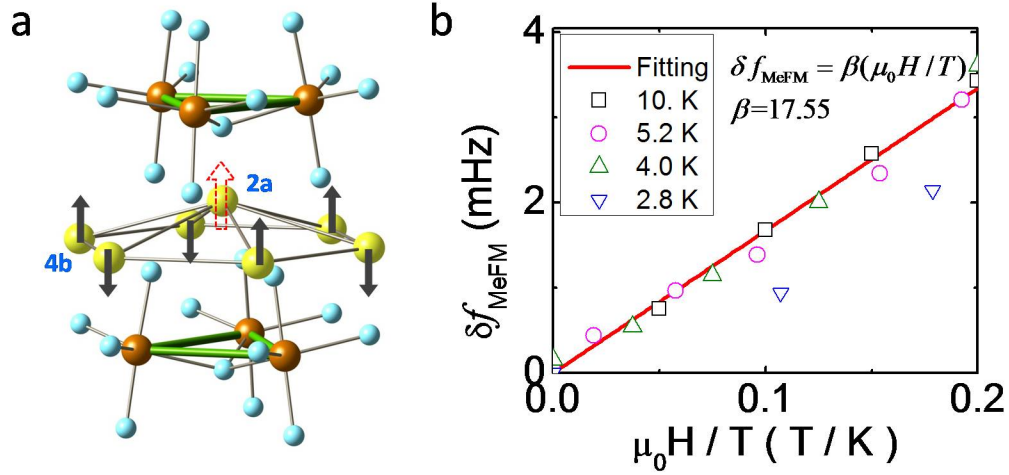
Figure 4.7: **a**, a 3D cartoon of the ErMnO$_3$ crystal structure, where yellow, brown, light blue spheres represent Er, Mn, O atoms, respectively. The black arrows at the 4b sites denote the Er^{3+} moments polarized by Mn^{3+} through DM interactions. The red hollow arrow at 2a site describes the paramagnetic spins induced by applied magnetic field. **b**, the MeFM signal is plotted against H/T at various T and H. [74]

phase, Er^{3+} at 4b sites are polarized antiferromagnetically, while the spin at 2a sites remain disordered due to the zero net DM exchange field (see Fig. 4.7) [78]. The rare earth moment induced by Mn^{3+} spins through DM interaction in B$_2$ phase is also discussed in Fig. 3.7. Therefore, the Er^{3+} spins at 2a sites are expected to show paramagnetic behavior, i.e., the H/T scaling at low field or high temperature region ($\mu_0 H/T < 0.2$). The non-linear ME effect ($E_z H_z^2$) at low field likely comes from the H-induced Er^{3+} moments at the 2a site. This behavior is consistent with the B$_2$ magnetic symmetry, which forbids any linear ME effect, but does allow nonlinear ones.

4.3.3   Divergent ME susceptibility in the intermediate A$_2'$ region

The most prominent feature in Fig. 4.6a is the pronounced divergence of the MeFM signal observed as the temperature is lowered in the intermediate-field A$_2'$ ($P3\underline{c}$) phase confined between two ME susceptibility anomalies: a kink and an asymmetric peak. There two anomalies are consistent with two-steps in magnetization measurements, shown in Fig. 4.8,
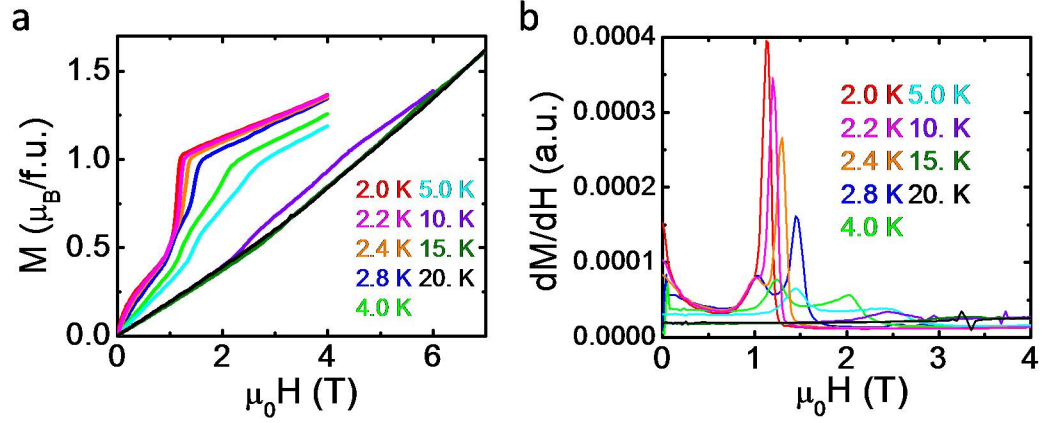
Figure 4.8: **a**, $M(H)$ data measured on a hexagonal ErMnO$_3$ single crystal at various temperatures. **b**, the derivative $\mathrm{d}M/\mathrm{d}H$ of the $M(H)$ in **a**. A two-peak feature is observed in the $\mathrm{d}M/\mathrm{d}H$ at low temperatures. As T decreases, the two peaks get closer and tend to merge to a single peak, i.e., a critical endpoint below 2 K. [74]

indicating a continuous spin reorientation transition in the A$_2'$ region. The magnetic susceptibility shows a two-peak feature, and the two peaks get closer, become more pronounced, and eventually merge to a single one around 2 K. Similarly, the MeFM anomalies, Fig. 4.6a, emerge only below ~ 6 K and converging to each other quickly as the temperature is lowered. The peak value at 2.8 K is 7-8 times larger than that of the linear magnetoelectric effect in the high-field A$_2$ phase. It is expected that the ME susceptibility α will diverge as the temperature is further lowered, similar to the magnetic susceptibility $\mathrm{d}M/\mathrm{d}H$. As mentioned in the Section 4.3.1, anomalous ME response could be present in the intermediate A$_2'$ region, where the spin ordering L is soft and $\partial L/\partial E$ term could be dominated at low temperatures.

To characterize the anomalous ME response, we consider the expansion of free energy in powers of $L_{A_2} = L\sin\psi$, which is compatible with $P6_3cm$ symmetry of the paramagnetic ferroelectric state. During the spin reorientation transition from B$_2$ to A$_2$, ψ varies between 0 and $\pi/2$. The formulas for the free energy expansion is

$$f = C_{20}L_{A_2}^2 + C_{11}L_{A_2}H_z + C_{02}H_z^2 + C_{40}L_{A_2}^4 + C_{31}L_{A_2}^3 H_z + C_{22}L_{A_2}^2 H_z^2 + C_{13}L_{A_2}H_z^3 +$$

$$C_{04}H_z^4 + E_z(D_{20}L_{A_2}^2 + D_{11}L_{A_2}H_z + D_{02}H_z^2 + D_{13}L_{A_2}H_z^3) \quad (4.7)$$

where the terms proportional to C_{20} and C_{40} describe the 2nd and 4th order magnetic anisotropies, the C_{11} term describes the weak ferromagnetism in the A_2 phase, D_{11} is the linear ME coupling. The P_z-dependence is not explicitly shown, because P_z is invariant under symmetry transformations of the ferroelectric phase.
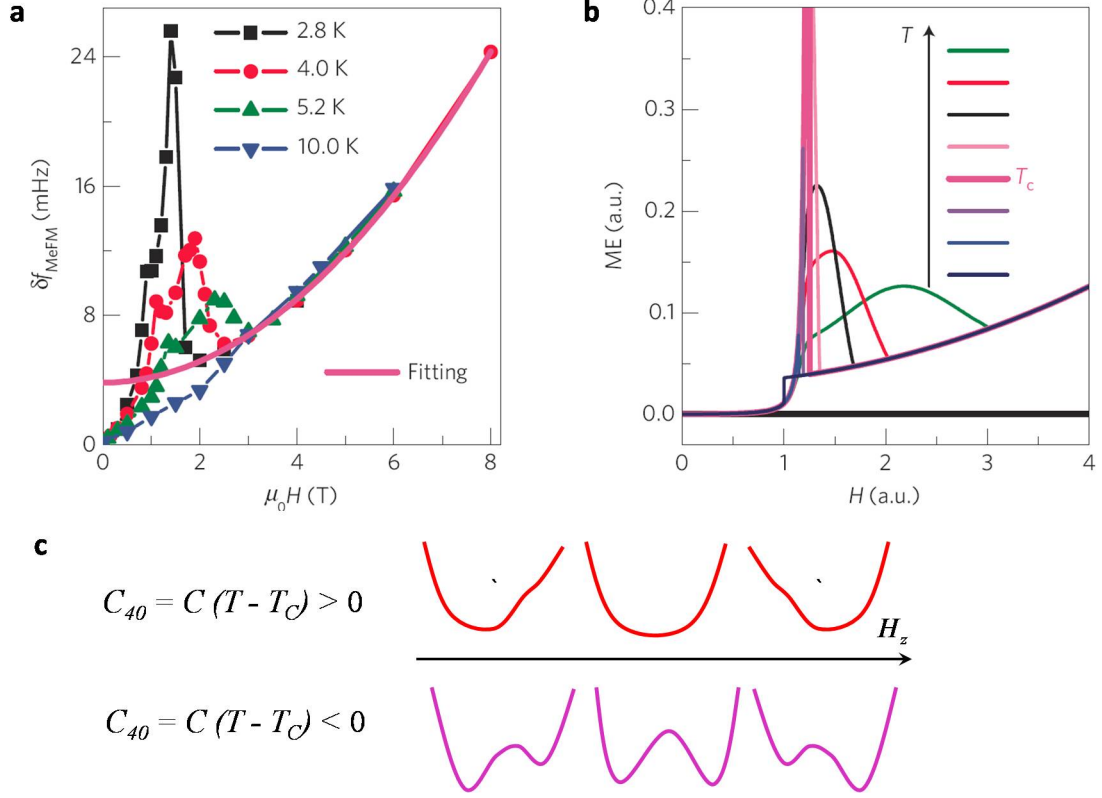
Figure 4.9: **a**, H-dependence of the MeFM signal at various temperatures and fitting curve. **b**, the simulated magnetic field (h) dependence of magnetoelectric responses at various effective temperatures (t) using a phenomenological Landau theory of the reorientation transition. Here t_c is the critical temperature at which the order of the spin reorientation transition changes from second to first. **c**, a cartoon shows the evolution of the energy minimum versus applied magnetic field above and below the critical temperature. [74]

Due to the weak ferromagnetism of the A_2 phase, the spin rotation angle ψ becomes nonzero as soon as $H_z \neq 0$. However, the re-orientation largely occurs near $C_{20} + C_{22}H_z^2 = 0$ and the character of the spin rotation depends on the sign of the 4th order anisotropy C_{40}. For $C_{40} > 0$, the spin reorientation goes continuously in an extended interval of H_z, while for $C_{40} < 0$, the angle ψ abruptly jumps from a small value to a large value, signaled a first-order transition. The evolution of the energy minimum with magnetic field

is characterized as the 2nd order and 1st transition for $T > T_C$ and $T < T_C$, respectively, shown in Fig. 4.9c. Assuming that C_{40} changes sign at ~ 2 K, we can qualitatively reproduce the experimentally observed phase diagram using the Landau expansion Eq. 4.7. The comparison between MeFM data and the simulation is shown in Fig. 4.9. In the vicinity of the critical temperature 2 K, the simulated ME susceptibility shoots up, agrees well with the observation.

In the continuous reorientation region, the rotation angle ψ is very sensitive to applied magnetic and electric fields, which give rise to the anomaly in the magnetoelectric coefficient,

$$(\frac{\partial M_z}{\partial E_z})_{E_z=0} = -\frac{\partial^2 f}{\partial E_z \partial H_z} + \frac{\frac{\partial^2 f}{\partial L_{A_2} \partial H_z} \frac{\partial^2 f}{\partial L_{A_2} \partial E_z}}{\frac{\partial^2 f}{\partial L_{A_2}^2}} \tag{4.8}$$

Here, the first term is proportional to the linear ME coupling D_{11} in Eq. 4.7, while the second term describes the anomalous response, which is large only in the reorientation region. As the interval shrinks to a point, the stiffness $\partial^2 f/\partial L_{A_2}^2$ becomes small, resulting in a sharp peak in the ME susceptibility. The calculated H_z dependence of $(\partial M_z/\partial E_z)_{E_z=0}$, Fig. 4.9b, reproduces well the observed field and temperature dependence of the ME response.

The $T - H$ phase diagram constructed from the MeFM peaks (red spheres) and the magnetization steps (blue triangles) is shown in Fig. 4.10a. The intermediate region becomes narrower at lower temperatures and merge into a tri-critical point (black star), at which the order of the reorientation transition changes from second to first (the red dashed line indicates the first-order B$_2 \rightarrow$ A$_2$ transition line). The simulated phase diagrams, based on the Landau theory, of the ME response and the order parameter ψ are plotted in Fig. 4.10b and c. The anomalous response is large in the continuous reorientation region, in which the magnetic state is extremely sensitive to external perturbations. It blows up near the tri-critical point where the system loses stiffness, $\partial^2 f/\partial L_{A_2}^2$, with respect to spin rotations, the bright spot in Fig. 4.10b. In other words, the diminishing energy barrier between B$_2$ and A$_2$ phases allows small perturbations such as H or E fields to swing the Mn^{3+} spins towards the A$_2$ phase by gaining either the Zeeman or the ME free energy (Fig. 4.10d),
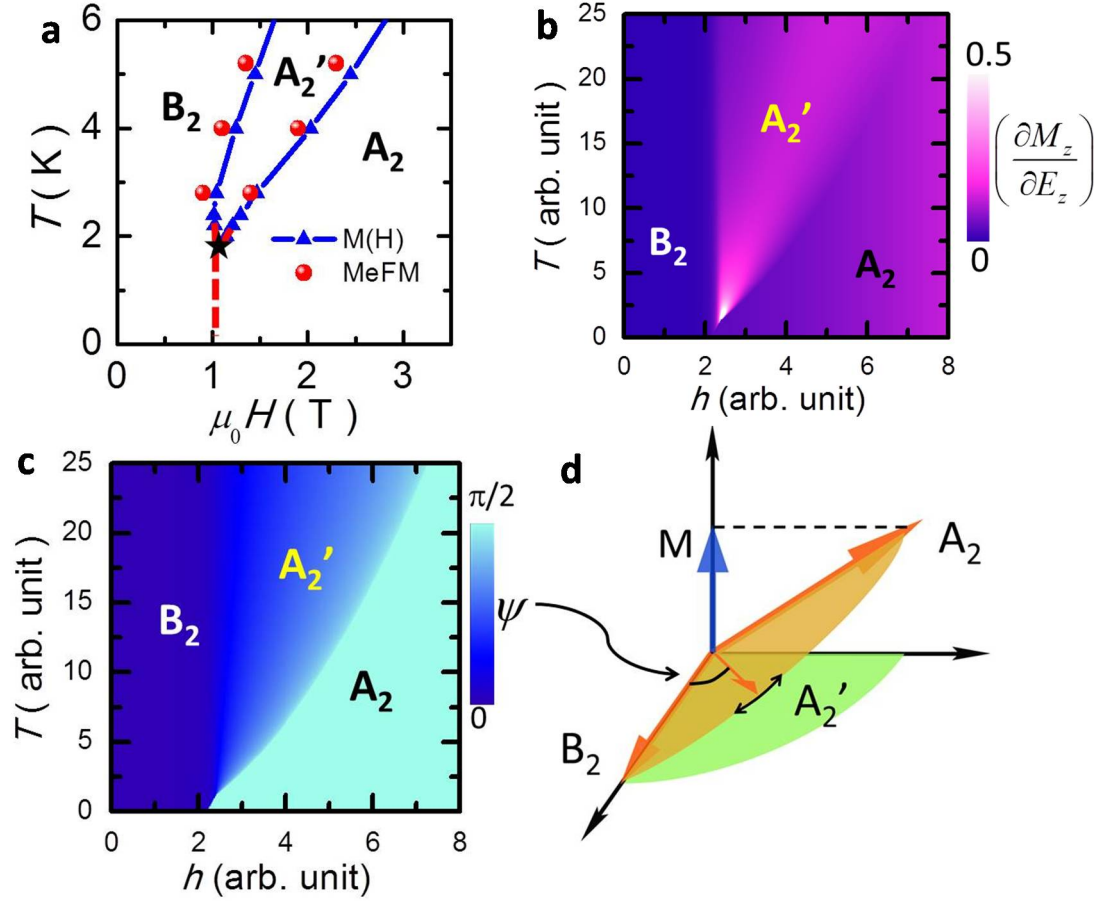
Figure 4.10: **a**, the $T-H$ phase diagram of $ErMnO_3$ constructed from the anomalies in MeFM (red spheres) and in dM/dH data (blue triangles) at various temperatures. The two crossovers converge into a possibly critical point (black star) of a first-order transition of $B_2 \rightarrow A_2$ (red dashed line). **b-c**, the simulated $T-H$ phase diagram of the ME response $(\partial M_z/\partial E_z)_{E_z=0}$, and the order parameter ψ. **d**, a cartoon illustration of giant responses due to critical fluctuations of Mn^{3+} spins in the intermediate A_2' phase near the critical point. The canting angle of Mn^{3+} spins is exaggerated for illustration. [74]

resulting in an additional increase of the canting moment M_z. This scenario is corroborated by the fact that in the vicinity of the critical point not only the magnetoelectric, but also the magnetic susceptibility tends to diverge (Fig. 4.8). The peak in the ME response is remarkably well reproduced within our phenomenological theory Fig. 4.9b and Fig. 4.10b.
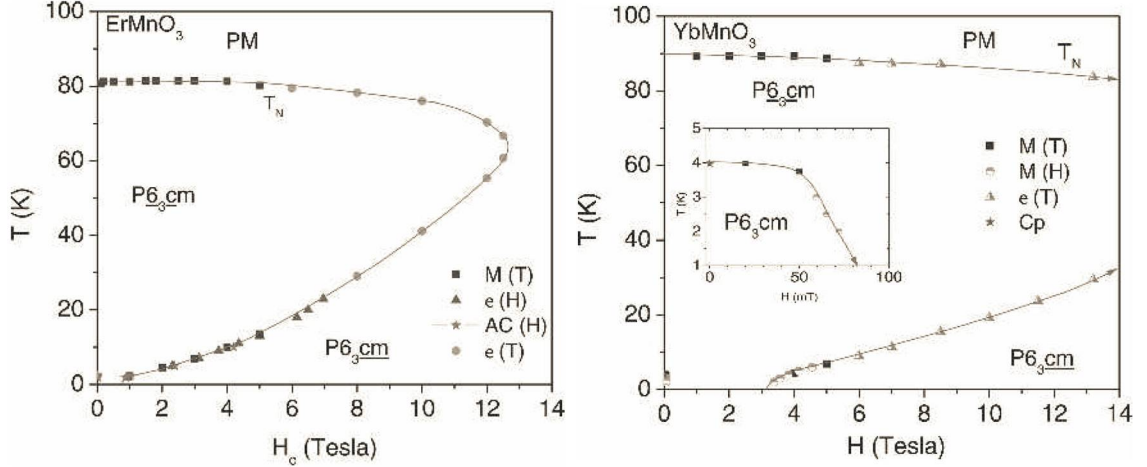
Figure 4.11: The phase boundary is derived from DC magnetization, dielectric constant, and AC magnetic susceptibility measurements. The inset in the YbMnO$_3$ phase diagram shows the Yb^{3+} moment order. [49]

4.4 MeFM study in hexagonal YbMnO$_3$

Hexagonal YbMnO$_3$ is in the same family with ErMnO$_3$, they share the similar reentrant $T-H$ phase diagram. Figure 4.11 shows the magnetic phase diagram of ErMnO$_3$ and YbMnO$_3$ based on the bulk DC magnetization, dielectric constant, and AC magnetic susceptibility measurements [49, 36]. This bending over behavior of the phase boundary originates from the exchange interaction between the Ising-like rare earth and Mn^{3+} spins. With the application of magnetic field, the Zeeman energy gain at the rare earth sites act back on the Mn^{3+} ordering through the DM interaction, causing Mn^{3+} spins to rotate from low field B$_2$ to high field A$_2$ phase. The rare earth spins are more rigid at lower temperature, resulting in the reentrant shape of the phase boundary. In addition, the phase boundary of YbMnO$_3$ requires higher magnetic field compared with ErMnO$_3$ at fixed temperature, and the turning over field for YbMnO$_3$ even extends beyond the measurement limit ($>$14 T) [49].

The $M(H)$ measurements for YbMnO$_3$ and ErMnO$_3$ provide more insights to the comparison, as shown in Fig. 4.12. The evolution of magnetization in YbMnO$_3$ shows a step-like behavior, while in ErMnO$_3$ it increases smoothly with tiny anomalies. As we will
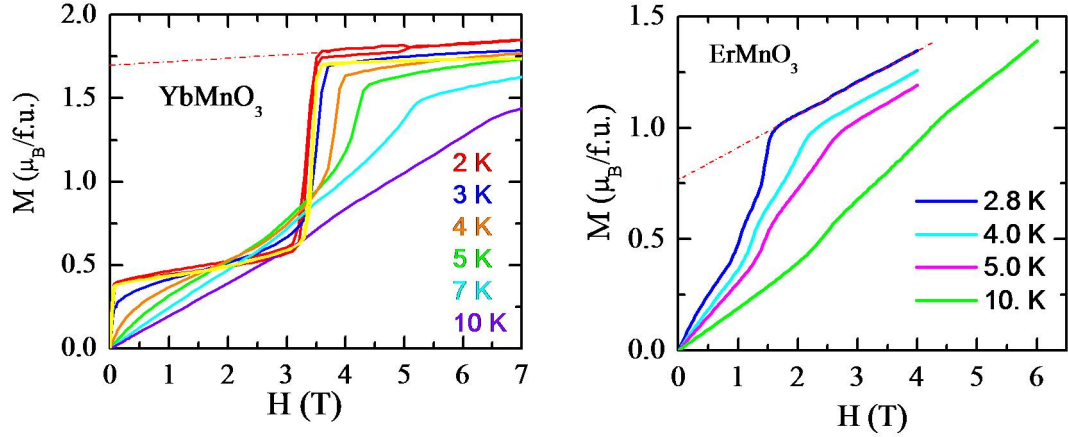
Figure 4.12: $M(H)$ measurements for YbMnO$_3$ (left panel) and ErMnO$_3$ (right panel) are taken under different temperatures.

see later, the spin reorientation transition in YbMnO$_3$ occurs in a narrow field range rather than a cross-over spin rotation in ErMnO$_3$, this is probably due to the strong out-of-plane anisotropy of Yb ion. From the $M(H)$ curve, the size of the rare earth spin can be inferred by extrapolating the high field magnetization back to zero field. The Yb^{3+} spin carries $\sim 1.7\mu_B$/f.u., and Er^{3+} moment is only $\sim 0.75\mu_B$/f.u.. Larger rare earth spins result in stronger DM interaction with Mn^{3+} spins. Meanwhile, Yb^{3+} spins are more rigid, and a higher magnetic field is required to align up all the spins, which may account for the discrepancy for the overall phase diagrams of YbMnO$_3$ and ErMnO$_3$.

Section 4.3 shows the ME susceptibility in ErMnO$_3$ tends to diverge near the critical temperature (2 K). Our MeFM measurements capture the divergence of anomalous ME response at low temperatures, for example, at 2.8 K, lowest stable temperature in MeFM measurements, the peak contrast of ME signal in ErMnO$_3$ is already one order of magnitude stronger than the linear ME effect. It would be of great interest to investigate the ME response at and below the critical point. Hexagonal YbMnO$_3$ has higher critical point ($\sim$3.5 K), evidenced by the step-like magnetization jump below 4.0 K (Fig. 4.12), which is within the base temperature limit of our MeFM. In addition, YbMnO$_3$ has similar magnetic phase diagram (Mn^{3+}) with ErMnO$_3$, but qualitatively different $M(H)$ behavior, i.e., the

characters of the rare earth site differ a lot. The systematic study of $YbMnO_3$ is important to understand the underlying ME mechanism in hexagonal manganites, and to disentangle the contribution from the Mn^{3+} and rare earth sublattices.
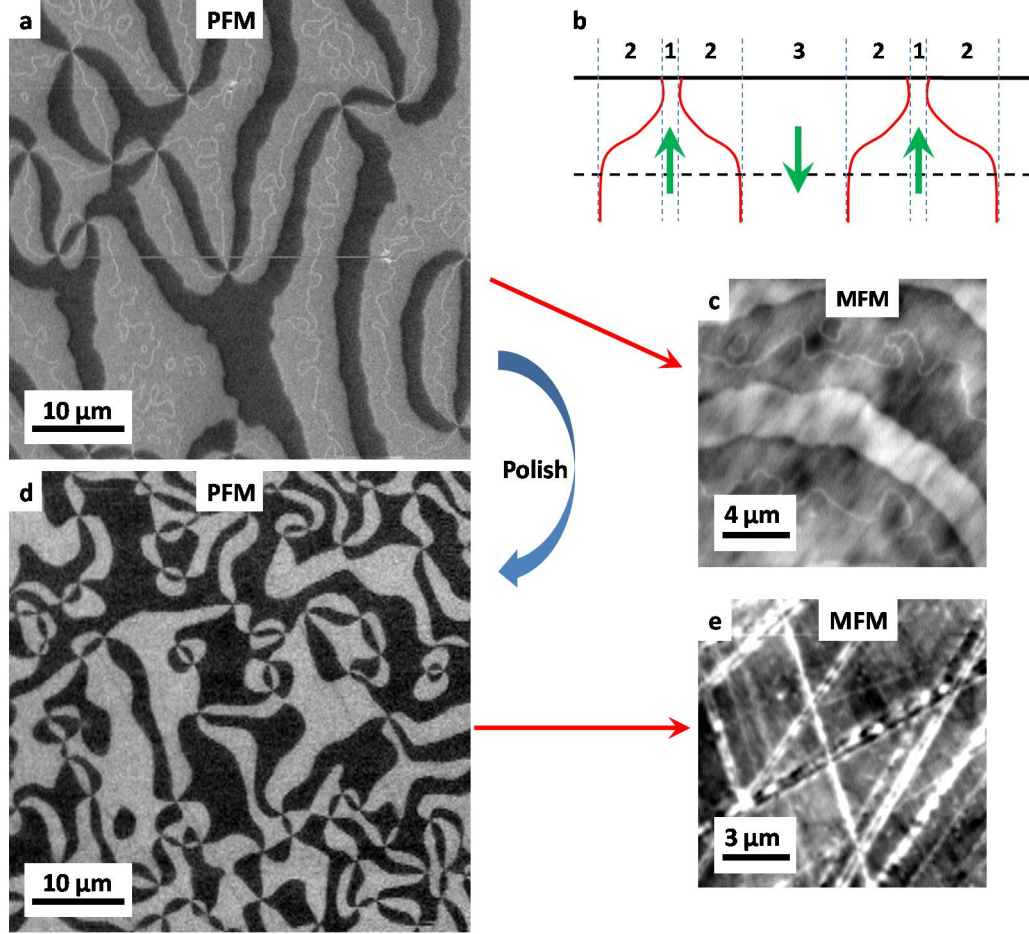
Figure 4.13: **a**, a large PFM image taken on the (001) as-grown surface of unpolished $YbMnO_3$ crystal. **b**, a cartoon scenario to explain the three-color contrast in **a**. Note that solid and dotted horizontal lines denote the surface position and the PFM penetrating depth, respectively. Red curved lines represent the ferroelectric domain boundary, and green arrows represent the polarization orientation. **c**, a typical MFM image (5.0 K, 2.5 T) taken on the unpolished surface. After polishing off 50 μm layer, **d**, the PFM image shows an evenly distributed up and down domains, and **e**, typical MFM image (5.0 K, 3.0 T) is filled with polishing lines.

The plate-like $YbMnO_3$ single crystals (thickness $\sim 200\mu$m) are synthesized by a conventional flux method. Several crystals from the same batch, with both as-grown and polished surface, are studied. Generally, as-grown surfaces are preferred because polishing procedure damages the magnetic structure of surface layer (4.13e), for instance, as-grown surfaces of

$ErMnO_3$ samples were used in MFM and MeFM measurements described in previous text. However, the $YbMnO_3$ (001) surface has the extra narrow meandering lines everywhere in the PFM (Fig. 4.13a) and MFM images (Fig. 4.13c). Because the PFM technique probes only finite depth near surface ($\sim$ tip radius 200 nm) [94], the narrow bright lines are likely due to a self-poling effect, that is, oxygen off-stoichiometry close to surface prefers downwards polarization [59], as shown in the cartoon in Fig. 4.13b. In region 1 (3), only up (down) polarization domain is present, causing strong bright (dark) contrast. While in the intermediate region 2, the stacking of opposite polarizations cancels out and results in a grey color contrast in PFM image. Because MeFM measurement is sensitive to surface layer as well, the measured ME contrast is attenuated by the stacking of opposite polarization domains along z axis in this as-grown surface. To resolve the issue, post-synthesis sample preparations, including polishing off surface layer and re-annealing (to relax the mechanical strain effect), were performed. Figure 4.13d shows a representative PFM image on the polished surface of $YbMnO_3$, where up and down polarization domains are evenly distributed with much stronger contrast. A serious issue of polished surface is that the mechanical polishing damages the local magnetic structure, resulting in extra line features in MFM, Fig. 4.13e. Therefore, certain area with less polishing lines is chosen. Besides, the line features are barely visible in MeFM measurement, though they overwhelm other features in static MFM images.

Figure 4.14 shows the same location MeFM images at different magnetic fields, which are aligned to PFM image by correlating the topographic landmarks. Clearly, the ME domain flips sign across the boundary of polarization domain, which is consistent with $ErMnO_3$. Despite of the similarity, the overall sign of α is inverted at 4.2 T, Fig. 4.14f, in striking contrast with that of $ErMnO_3$. Furthermore, the ME contrast at high field is negligible, suggesting an almost zero nonlinear ME effect. Note that 4.2 T is also the phase boundary between B_2 and A_2 phase, the interplay between Mn^{3+} and Yb^{3+} spins accounts for the unprecedented behavior.
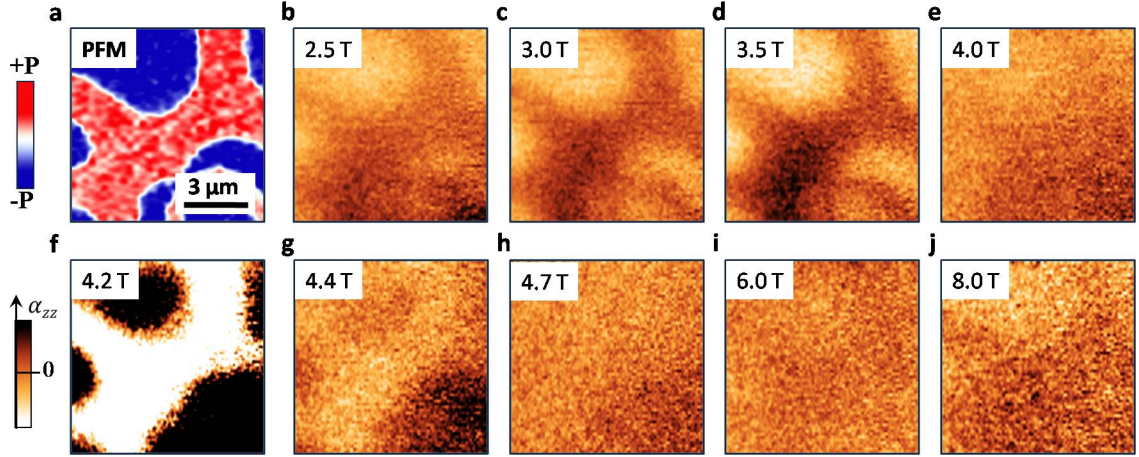
Figure 4.14: **a**, ambient PFM image, and **b-j**, 5.0 K MeFM images under various magnetic field (up to 8.0 T), taken at the same location of (001) surface of a hexagonal YbMnO$_3$ single crystal.
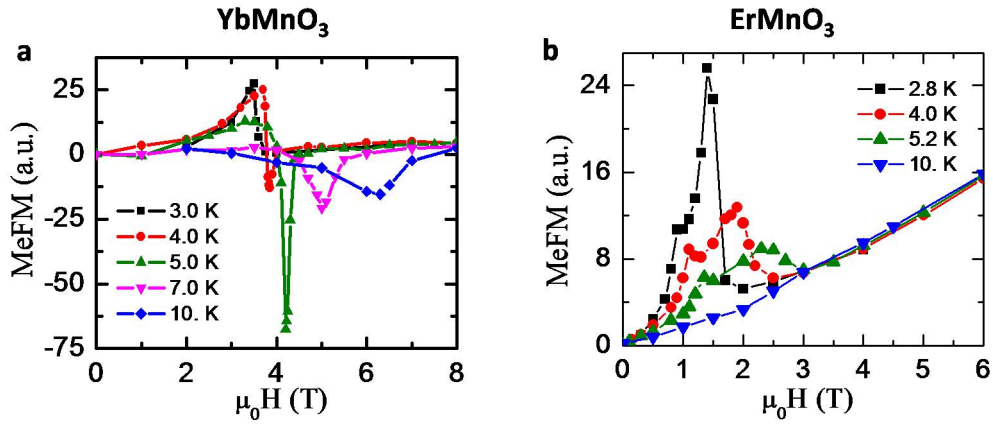
Figure 4.15: **a**(**b**), plots of H-dependent MeFM signals at various temperatures (up to 10 K) for hexagonal YbMnO$_3$ (ErMnO$_3$).

To get a comprehensive picture of ME coupling mechanism, systematic studies at various temperatures (3.0-10 K) and magnetic fields (0-8.0 T) in YbMnO$_3$ are performed and compared with those of ErMnO$_3$, as shown in Fig. 4.15. The overall signal in YbMnO$_3$ is much weaker except the intermediate region. In both B$_2$ and A$_2$ region, the ME contrast is slightly above zero, while approaching the transition, the strength increases with magnetic field then sharply drops down to deep negative value at the transition point. Above the transition, the ME contrast plumbs down to a small positive value, which is likely due to the saturation of the Yb moment in A$_2$ phase. Getting closer to the critical point from high

temperature (> 4 K), the peak becomes stronger and tends to diverge at lower temperature, which is quite similar to the intermediate A_2' region in $ErMnO_3$. The most significant distinction is the sign of the divergence at the phase boundary, that is, the second peak in $YbMnO_3$ has opposite sign with rest regime. Naturally, it is expected that α_{RE} has the same sign with α_{Mn} in $ErMnO_3$, while they are opposite in $YbMnO_3$. At even lower temperature (< 4 K), the strength of the second peak reduces, and the separation of two peaks becomes negligible. At the lowest temperature (3 K), the negative peak disappears, leaving only a single asymmetric positive peak. This behavior can be explained by the two 2nd order transition lines merging into one 1st order one. Below the critical temperature, the transition from B_2 to A_2 is infinitely sharp, therefore, the divergence cannot be captured by the measurements.
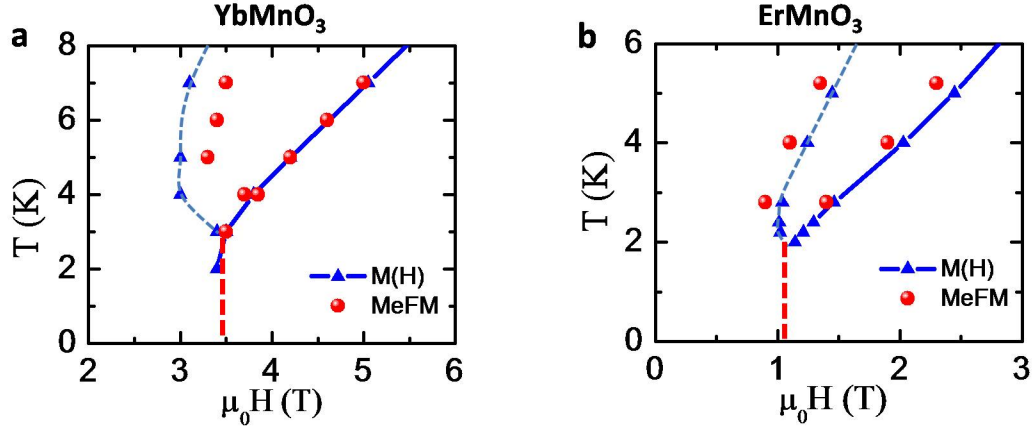
Figure 4.16: **a**(**b**), the $T-H$ phase diagram of hexagonal $YbMnO_3$ ($ErMnO_3$) is constructed from the anomalies in MeFM curves (red spheres) and dM/dH (blue triangles). The red dash lines denote the 1st order phase transition of $B_2 \rightarrow A_2$ below the critical points.

The magnetic $T - H$ phase diagram in Fig. 4.16 are constructed from the anomalies in dM/dH (blue triangles) and peaks in MeFM curve (red spheres), both of which are performed on the same crystal batch. Note that the transition points deferred from MeFM (Fig. 4.16a) are approximated from the positive/negative peak positions. The results from the macroscopic and mesoscopic measurements agree well with each other. The discrepancies for the phase boundary deferred from MeFM and the $M(H)$ curve are likely due to the

variation of sample crystals and the selection criteria for the phase boundary points. Two peaks in MeFM correspond to the two-step magnetization in $M(H)$. The first boundary is cross-over transition, which is noted as blue dotted line in Fig. 4.16. Both of the phase diagrams show the tri-critical points, with two 2nd order phase boundaries (blue lines) merging into a single 1st order phase transition line (red dotted line).
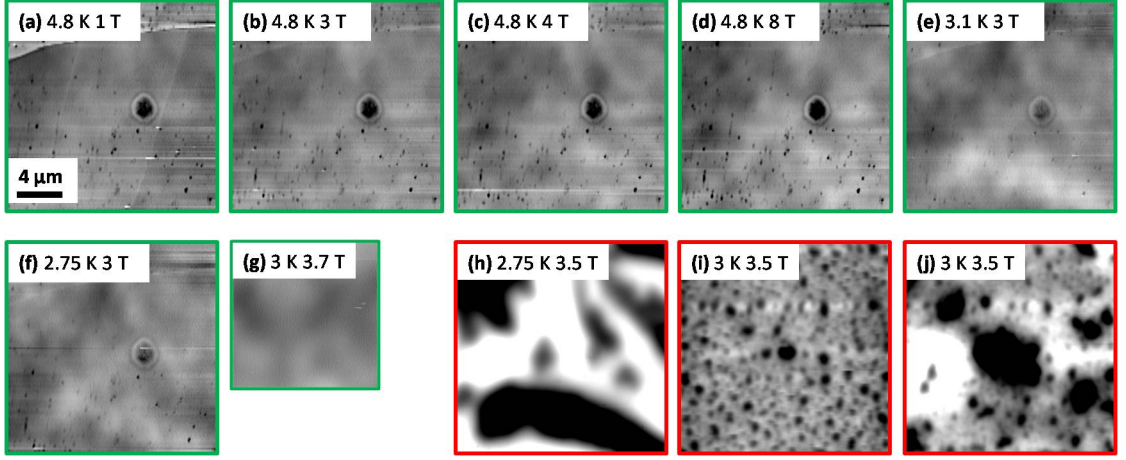
Figure 4.17: **a-j**, the same location MFM images of YbMnO$_3$ are taken at various temperatures and magnetic fields. Note that the color scale for the green boxed (**a-g**) and red boxed (**h-j**) images are 1.53 Hz and 15.3 Hz, respectively.

The $T - H$ phase diagram of YbMnO$_3$ is consistent with MFM measurements as well. Due to the character of antiferromagnetic domains, the MFM image contrast is weak for most of the regions in the phase diagram. If the transition line below the critical point is indeed 1st order, a phase coexistence may be observed at the phase boundary. The MFM measurements on hexagonal YbMnO$_3$ are sampled all over the phase space (2.75-5 K, 0-8 T), as shown in Fig. 4.17. Above the critical point, the domains and DWs contrast is weak for the whole magnetic field range (Fig. 4.17a-d). At lower temperature where 1st order transition occurs, the contrast is still weak within the pure B$_2$ (Fig. 4.17e,f) and A$_2$ phase (Fig. 4.17g). However, the contrast is significantly enhanced along the 1st order phase boundary (Fig. 4.17h-j). The bubble-like domain has 20 times stronger contrast than other phase space points (Fig. 4.17a-g). Note that the color scale for Fig. 4.17a-g is 15.6 Hz, and 1.56 Hz for the rest images. Because the pronounced domain pattern appears around 3.5

T, which is sufficient to align most moments of ferromagnetic domains, the only reasonable explanation is the coexistence of low-moment B_2 and high-moment A_2 phase. The phase coexistence at the phase boundary agree with the step-like jump $M(H)$ (Fig. 4.12) at low temperatures (< 4.0 K), suggesting the 1st order transition. The appearance of the domains evolves even after the subsequent scans under exactly same conditions (Fig. 4.17i and j), confirming the slow dynamic process during the transitions.

4.5 Revisit of Landau theory

In previous Section 4.3, the Landau theory, in the expansion of spin ordering L_{A_2}, is implemented to explain the anomalous ME response in the intermediate region A_2' in ErMnO$_3$. In that phenomenological model, the sign of the 4th order anisotropy $C_{40} = C(T - T_C)$ is assumed to be opposite for above and below the critical temperature without justification. The MeFM studies in YbMnO$_3$ have provided more evidences for the critical fluctuation enhanced ME susceptibility in hexagonal manganites, though there are discrepancies in terms of the sign of the divergent ME effect and the A_2 phase behavior. To unify the two cases, M. Mostovoy proposed to take into account of the rare earth free energy, derived from a microscopic spin model of exchange coupling between Mn and Yb spins, in the complete free energy expansion.

4.5.1 Include RE free energy

The Landau free energy of Mn and RE spins is :

$$f = f^{\text{Mn}} + f^{\text{RE}} \tag{4.9}$$

Considering the Mn ordering in $P6_3cm$ (polar) structure, the free energy is

$$f^{\text{Mn}} = (C_{11} + D_{11}E)LH + (C_{20} + D_{20}E)L^2 + (C_{02} + D_{02}E)H^2 + (C_{22} + D_{22}E)L^2H^2 + C_{40}L^4 + ...$$
$$\tag{4.10}$$

which is the full Landau free energy considered in Eq. 4.7 in Section 4.3.3. Here $L = L_{A_2} = \sin\psi$ $(L_{B_2} = \cos\psi)$ is the Mn spin orientation order parameter in A_2 (B_2) phase. For RE magnetism, we only consider the 4b sites. The RE spins are Ising-like (anisotropy), with the moment $\mu^{RE} = gJ\mu_B$, where $g = g^0 + g^1 E_z$ is the $g-$factor of RE spins, and g^1 describes the linear electric field dependence of the $g-$factor at the 4b sites of $P6_3cm$ structure. Therefore the Zeeman energy of RE moment is

$$\varepsilon^{RE} = -\mu^{RE}H_z = -(g^0 + g^1 E_z)J\mu_B H_z = -(\mu + \alpha E_z)H_z \tag{4.11}$$

where $\mu = g^0 J\mu_B$ is the RE moment and $\alpha = g^1 J\mu_B$ is the electric field dependence of RE moments due to E_z dependent $g-$factor, which leads to macroscopic magnetoelectric effect α^{RE}.

The Hamiltonian of RE spins at 4b sites $(\sigma_1, \sigma_2, \sigma_3, \sigma_4)$ in the exchange field of Mn^{3+} order is:

$$\mathcal{H}^{RE} = -g_1 \cos\psi(\sigma_1 - \sigma_2 + \sigma_3 - \sigma_4) - g_2 \sin\psi(\sigma_1 + \sigma_2 + \sigma_3 + \sigma_4)-$$

$$(\mu + \alpha E_z)H_z(\sigma_1 + \sigma_2 + \sigma_3 + \sigma_4) \tag{4.12}$$

Here σ_i is Ising spins with values ± 1. The g_1 (g_2) term describes the RE-Mn coupling in B_2 (A_2) phase. The last term is the Zeeman coupling with magnetic moment dependent on E_z.

Based on the microscopic spin model, we get the rare earth free energy by solving he partition function,

$$f^{RE} = -\frac{1}{\beta}\ln Z^{RE} = -\frac{2}{\beta}[\ln\cosh(\beta h_1) + \ln\cosh(\beta h_2)] - \frac{4\ln 2}{\beta} \tag{4.13}$$

see Appendix A for the detail.

4.5.2 $\alpha_{zz}^{\mathbf{Mn}}$

The magnetoelectric effect in hexagonal manganites has two contributions: RE and Mn:

$$\alpha_{zz} = \frac{\partial M_z}{\partial E_z} = \alpha_{zz}^{Mn} + \alpha_{zz}^{RE} \tag{4.14}$$

In fact, the expression in Eq. 4.8 is merely the contribution from Mn^{3+} spins. The magnetoelectric effect of Mn^{3+} order is:

$$\alpha_{zz}^{Mn} = \frac{\partial M_z^{Mn}}{\partial H_z} = -\frac{\partial^2 f^{Mn}}{\partial E_z \partial H_z} - \frac{\partial^2 f^{Mn}}{\partial E_z \partial \psi} \cdot \frac{d\psi}{dH_z} \tag{4.15}$$

in which, the second term considers nonrigid Mn^{3+} spin, i.e., it can be rotated by applied electric or magnetic fields. The derivation of each items in Eq. 4.15 is list in Appendix A. The second term in Eq. 4.15 is responsible for the anomalous ME responsible, which is discussed in Sec. 4.3.3 as well. Apparently, the anomalous term diverges as the spin rotation angle $\psi \to 90^o$, causing the divergence of α_{zz}^{Mn}.

4.5.3 α_{zz}^{RE}

To evaluate α_{zz}^{RE}, the RE magnetic moment and polarization are calculated based on the RE free energy Eq. 4.13:

$$M_z^{RE} = -\frac{\partial f^{RE}}{\partial H_z} = 2(\mu + \alpha E_z)[\tanh(\beta h_1) + \tanh(\beta h_2)] = \frac{\mu + \alpha E_z}{\alpha H_z} P_z^{RE} \tag{4.16}$$

$$P_z^{RE} = -\frac{\partial f^{RE}}{\partial E_z} = 2\alpha H_z[\tanh(\beta h_1) + \tanh(\beta h_2)] = \frac{\alpha}{\mu + \alpha E_z} M_z^{RE} H_z \tag{4.17}$$

Note that this value has to be divided by 4 to get the proper magnetization (in the unit of μ_B/f.u.). Therefore, the magnetoelectric effects due to RE moments:

$$\alpha_{zz}^{RE} = \frac{dP_z^{RE}}{dH_z} = \frac{\alpha}{\mu + \alpha E_z} \cdot \left(M_z^{RE} + H_z \frac{dM_z^{RE}}{dH_z} \right) \tag{4.18}$$

The susceptibility of RE moments is:

$$\frac{dM^{RE}}{dH_z} = \frac{\partial M^{RE}}{\partial H_z} + \frac{\partial M^{RE}}{\partial \psi} \cdot \frac{d\psi}{dH_z} \tag{4.19}$$

$$\frac{\partial M^{RE}}{\partial H_z} = 2(\mu + \alpha E)^2 \beta[\text{sech}^2(\beta h_1) + \text{sech}^2(\beta h_2)] \tag{4.20}$$

Clearly, the rare earth contribution to the ME effect α_{zz}^{RE} contains the term proportional to the magnetic susceptibility dM^{RE}/dH_z. This is consistent with the MeFM observations that $ErMnO_3$ has strong nonlinear ME response in A_2 phase while it's close to zero in

$YbMnO_3$, as shown in Fig. 4.15. This discrepancy is due to the large magnetic susceptibility in $ErMnO_3$ at high field, and flat $M(H)$ in $YbMnO_3$ after the magnetization jump, Fig. 4.12. Note that the Mn^{3+} canting moment (tilt angle $< 1^o$) contributes little to the overall magnetization, the out-of-plane $M(H)$ curve mainly characterizes the RE^{3+} behavior.

In the Landau theory in Section 4.3.3, where rare earth free energy is not considered, the change from two 2nd order transitions (above critical temperature) to one 1st order line (below critical temperature) is simulated by explicitly flipping the sign of C_{40}, the 4th order anisotropy (Fig. 4.9). By including the Ising-like rare earth contribution, the critical phenomena naturally emerges, in particular, the H-dependent ME susceptibility at various temperatures can be reproduced with fixed tuning parameters. It turns out that the sign of RE-Mn coupling term g_2 in Eq. 4.12 determines the divergence behaviors of $YbMnO_3$ and $ErMnO_3$. When g_2 is set to be positive, the divergence peak get enhanced in approaching the critical temperature, and it evolves into a step-like function below critical point, which is in excellent agreement with the $ErMnO_3$ behavior, as illustrated in Fig. 4.9b and Fig. 4.18a. For negative g_2, the divergence shows a negative peak, which grows as getting close to critical point. Below the critical temperature, the negative divergence disappears, and only a positive broad peak presents, as shown in Fig. 4.18b, which matches the MeFM observation in $YbMnO_3$ very well.

In the simulation, the nonzero parameters of Eq. 4.10 and 4.13 include: the Zeeman energy term $C_{11}LH$, field-induced spin reorientation $(C_{20} + C_{22}H^2)L^2$, the trilinear ME term $D_{11}ELH$, and the rare earth free energy. The order parameter L is calculated by minimizing the total free energy under certain (T, H) condition. By simply changing the sign of g_2, the ME susceptibility behavior for $ErMnO_3$ and $YbMnO_3$ can be reproduced. Note that g_2 term corresponds to the interplay between RE^{3+} and Mn^{3+} sublattices. The simulation disentangles the ME components of the Mn and RE sublattices, which contribute the same direction in $ErMnO_3$ while oppositely in $YbMnO_3$. Since α^{Mn} is responsible for the anomalous divergence in the intermediate A_2' phase, the $3d - 4f$ interplay accounts for
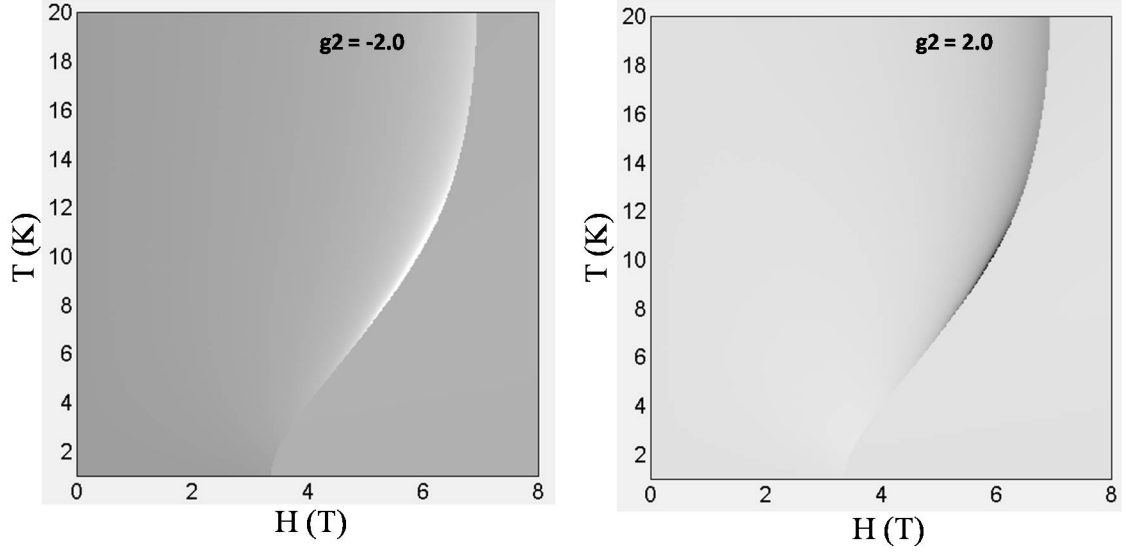
Figure 4.18: The simulation of α_{zz} under various temperature and magnetic fields for ErMnO$_3$ (**a**) and YbMnO$_3$ (**b**) based on the Landau free energy Eq. 4.10 and 4.13, with nonzero parameters C_{11} = -0.02, C_{20} = 0.1, C_{22} = -0.02, D_{11} = 0.008, g_1 = 6, α = 0.002, and g_2 = -2.0 for ErMnO$_3$ (**a**), g_2 = 2.0 for YbMnO$_3$ (**b**).

the negative divergence in YbMnO$_3$.

In this Landau theory study, Mn^{3+} and RE^{3+} sublattice contributes differently at different phase regions. The anomalous ME response, in the intermediate region, is due to the non-rigidity of the Mn^{3+} spins during spin reorientation. It tends to diverge when approaching the critical point. In the high field A$_2$ phase, the rare earth contribution dominates because α^{Mn} is small. A microscopic exchange model is proposed by assuming a E-dependent g factor at the RE site, and the rare earth ME susceptibility is found to be proportional to the magnetic susceptibility (Eq. 4.18). The different divergence signs for the two hexagonal manganites are attributed to the relative sign of α at Mn^{3+} and RE^{3+} sites, which can be reproduced by changing the sign of RE-Mn coupling coefficient, implying a strong $3d-4f$ interplay in this system [95]. However, current theory cannot reproduce the quadratic H dependence in the A$_2$ phase in ErMnO$_3$. In addition, first-principles studies are necessary to explain the microscopic mechanism for the different $3d-4f$ coupling in ErMnO$_3$ and YbMnO$_3$.

Chapter 5

Conclusions and discussions

This thesis work presents a systematic study of the multiferroic hexagonal manganites by utilizing a collection of cutting-edge microscopic techniques. To find out the underlying mechanism of the ME coupling, the domain and domain wall structure are investigated to reveal the intrinsic bulk property. The novel MeFM technique, by combining our unique cryogenic MFM and lock-in technique, is developed to visualize the ME domain structure directly. MeFM measurements are performed in different hexagonal manganites systems, including $ErMnO_3$ and $YbMnO_3$, and unprecedented ME susceptibility properties are revealed. The main findings in terms of the ME mechanism in hexagonal manganites are summarized in the following.

For the first time, the uncompensated moments along an antiferromagnetic domain walls were observed in hexagonal $ErMnO_3$. By correlating the ambient PFM and MFM images at the same location, magnetic DWs are found to strongly interlock with ferroelectric one, with alternating up and down net magnetization around the vortex core [78]. The uncompensated magnetization originates from the Ising-like rare earth spins polarized by Mn^{3+} moment through the DM interaction, which is evidenced by the Curie-Weiss like DW behavior at different temperatures. More interestingly, the alternating magnetic pattern is universal and interconnects through the self-organized ferroelectric vortex network, implying a strong non-trivial bulk coupling of lattice, charge, and spin. A more elaborate Landau theory explains the multiferroic character of the topological defects in hexagonal manganites. The rotation of Mn^{3+} spins across the DWs, manifested as uncompensated moment, is correlated with the spin states of neighbouring domains. The Mn^{3+} spins increase by 4π around the vortex
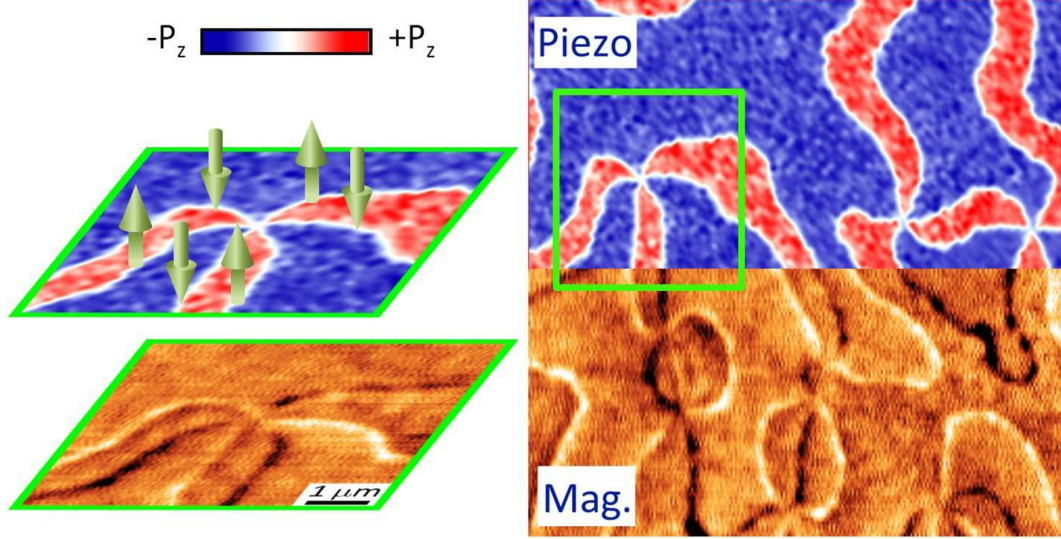
Figure 5.1: The red-blue image represents the electric polarization domain in the (001) surface of hexagonal ErMnO$_3$, the yellowish one shows the magnetic properties. The perspective images characterize the interlocked magnetic and ferroelectric antiphase structural domain boundaries. A large area of vortex network is displayed with top half PFM image and lower half MFM one. [78]

core, suggesting the structural and ferroelectric vortices are also magnetic ones, which is summarized by Fig. 5.1.

The MFM study of DWs at different magnetic fields reveals the evolution of bulk spin state. The $B_2 \rightarrow A_2$ transition is accompanied by a pronounced H-dependent DW moments, specifically, the moment of type I DW gradually changes through the transition, while type II DW shows a sudden moment reversal at certain rotation angle. The DWs magnetism is simulated by assuming the Mn^{3+} spins rotate coherently under external magnetic field, and the results match well with the observation. The magnetic field dependence of DW magnetization demonstrates the feasibility of probing the bulk domain state from the DW magnetism.

The ultimate goal of studying multiferroics is the realization of direct cross coupling between magnetic and electric orders. The lack of direct imaging of ME domain pattern motivates the development of MeFM, which is a local detection of E-induced magnetization [71, 74]. The MeFM technique and the measurement on hexagonal manganites are

Figure 5.2: The figure summarizes the principle of MeFM technique and how it measures the ME domain in hexagonal manganites. The sample is sandwiched by two parallel electrodes to apply high electric field E. The tip is coated with magnetic materials, forming a tiny magnetic dipole. Background PFM image shows the typical ferroelectric domain pattern on (001) surface of hexagonal manganites. When the tip scans over the surface with high E-field applied, the vortex-like ME domain patterns (perspective yellowish image) emerge, which resemble the ferroelectric one.

summarized in Fig. 5.2. The images with blue-white (yellow-red) color correspond to PFM (MeFM) one. Only magnetic signal is detected due to the coated electrodes, and the electric field is confined within the sample. The applied E-field induces the local magnetization, which is sensed by the magnetic tip. The ME domain pattern resembles ferroelectric one because of the lattice-mediated coupling mechanism.
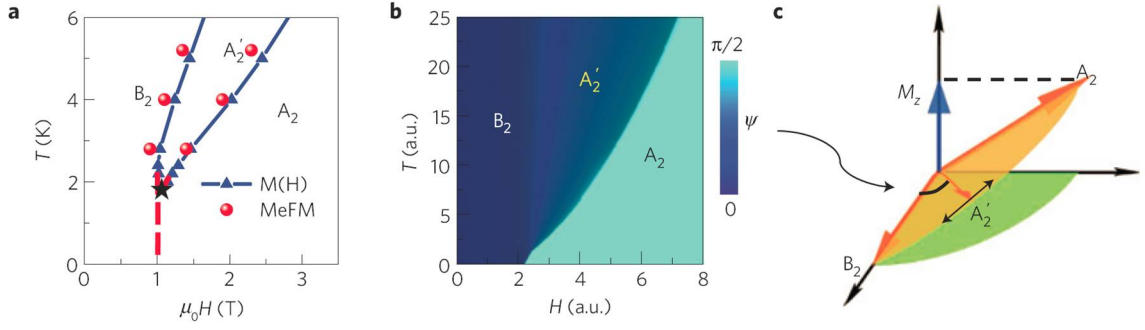
Figure 5.3: **a**, $T - H$ phase diagram of $ErMnO_3$, where the two crossovers converge into a critical point (black star) of a 1st order phase transition below 2 K. **b**, a simulated $T - H$ phase diagram using a Landau theory. **c**, a cartoon illustration of giant response due to critical fluctuations of Mn^{3+} spins in A_2' phase. [74]

Great success has been achieved in the MeFM study of hexagonal manganites [74], including $ErMnO_3$ and $YbMnO_3$. The direct visualization of ME domain pattern in nanometer scale was captured in $ErMnO_3$ for the first time. The ME response changes sign at each structural domain wall, a result that is corroborated by symmetry analysis, phenomenological modelling and first-principles calculations, and provides compelling evidence for a lattice-mediated ME coupling. In other words, the buckling of MnO_5 polyhedral changes, as the applied E field changing the polarization, and results in the changes of the canting moment of Mn^{3+} spins. Moreover, the systematic MeFM studies in the $T - H$ phase space reveal a giant enhancement of the ME effect due to the critical fluctuation. In the intermediate A_2' phase, also known as continuous spin reorientation region, the magnetic state is extremely sensitive to external perturbations, contributing to the anomalous ME response. The Mn^{3+} spin is swung with a large amplitude in approaching the critical point, as shown in Fig. 5.3, where the energy barrier between B_2 and A_2 is diminishing. This results in a divergence of the ME and magnetic susceptibility. Furthermore, similar studies on $YbMnO_3$ provide more insights into the ME coupling mechanism in hexagonal manganites. The critical fluctuation enhanced ME response is confirmed in both systems, and the $T - H$ diagram with two 2nd order spin reorientation merging into one single 1st order line is further supported by the MFM measurements. The discrepancy lies in the sign flip of

the divergence direction in YbMnO$_3$. The full free energy is considered based on Landau theory, by incorporating the rare earth part from a microscopic spin model. Both the ME phase diagrams of ErMnO$_3$ and YbMnO$_3$ can be reproduced with the same theory, but opposite RE-Mn coupling term. This study suggests that the $3d - 4f$ coupling and the Ising anisotropy RE spins are the key to understand the critical fluctuation phenomena and the re-entrant spin reorientation phase boundary.

The MeFM technique provides a route for exploring emergent phenomena at the mesoscopic scale such as magnetoelectric coupling in multiferroic domains and domain walls. More exciting studies can be performed in other correlated systems, including the ME coupling in mutiferroic skyrmions [96] and magnetic topological insulators [91, 92, 97]. The MeFM results in hexagonal manganites reveal a divergent ME susceptibility near the tricritical point, suggesting a possibility to enhance ME effects by harnessing critical fluctuations and phase competition [98, 74, 55, 99, 100, 101], which may lead to the discovery of large ME effects at room temperature.

References

[1] J. C. Maxwell, "A dynamical theory of the electromagnetic field.," *Proceedings of the Royal Society of London*, vol. 13, pp. 531–536, 1863.

[2] S.-W. Cheong and M. Mostovoy, "Multiferroics: a magnetic twist for ferroelectricity," *Nature materials*, vol. 6, no. 1, pp. 13–20, 2007.

[3] W. Eerenstein, N. Mathur, and J. F. Scott, "Multiferroic and magnetoelectric materials," *Nature*, vol. 442, no. 7104, pp. 759–765, 2006.

[4] N. A. Spaldin, S.-W. Cheong, and R. Ramesh, "Multiferroics: past, present, and future," *Phys. Today*, vol. 63, pp. 38–43, 2010.

[5] N. A. Spaldin and M. Fiebig, "The renaissance of magnetoelectric multiferroics," *Science*, vol. 309, no. 5733, pp. 391–392, 2005.

[6] R. Ramesh and N. A. Spaldin, "Multiferroics: progress and prospects in thin films," *Nature materials*, vol. 6, no. 1, pp. 21–29, 2007.

[7] N. A. Hill, "Why are there so few magnetic ferroelectrics?," *The Journal of Physical Chemistry B*, vol. 104, no. 29, pp. 6694–6709, 2000.

[8] D. Khomskii, "Magnetism and ferroelectricity; why do they so seldom coexist?," in *APS Meeting Abstracts*, vol. 1, p. 21002, 2001.

[9] R. Seshadri and N. A. Hill, "Visualizing the role of bi 6s lone pairs in the off-center

distortion in ferromagnetic bimno3," *Chemistry of materials*, vol. 13, no. 9, pp. 2892–2899, 2001.

[10] M. Fiebig, "Revival of the magnetoelectric effect," *Journal of Physics D: Applied Physics*, vol. 38, no. 8, p. R123, 2005.

[11] T. Kimura, T. Goto, H. Shintani, K. Ishizaka, T. Arima, and Y. Tokura, "Magnetic control of ferroelectric polarization," *Nature*, vol. 426, no. 6962, pp. 55–58, 2003.

[12] N. Hur, S. Park, P. Sharma, J. Ahn, S. Guha, and S. Cheong, "Electric polarization reversal and memory in a multiferroic material induced by magnetic fields," *Nature*, vol. 429, no. 6990, pp. 392–395, 2004.

[13] M. Kenzelmann, A. Harris, S. Jonas, C. Broholm, J. Schefer, S. Kim, C. Zhang, S.-W. Cheong, O. Vajk, and J. Lynn, "Magnetic inversion symmetry breaking and ferroelectricity in tbmno 3," *Physical review letters*, vol. 95, no. 8, p. 087206, 2005.

[14] N. Hur, S. Park, P. Sharma, S. Guha, and S. Cheong, "Colossal magnetodielectric effects in dymn2o5," *Physical review letters*, vol. 93, no. 10, p. 107207, 2004.

[15] T. Goto, T. Kimura, G. Lawes, A. Ramirez, and Y. Tokura, "Ferroelectricity and giant magnetocapacitance in perovskite rare-earth manganites," *Physical review letters*, vol. 92, no. 25, p. 257201, 2004.

[16] L. D. Landau, E. M. Lifšic, J. B. Sykes, J. S. Bell, M. Kearsley, and L. P. Pitaevskii, *Electrodynamics of continuous media*, vol. 364. Pergamon press Oxford, 1960.

[17] J.-P. Rivera, "A short review of the magnetoelectric effect and related experimental techniques on single phase (multi-) ferroics," *The European Physical Journal B*, vol. 71, no. 3, pp. 299–313, 2009.

[18] I. E. Dzyaloshinskii, "The magnetoelectric effect in antiferromagnetic materials," *Zh. Eksp. Teor. Fiz*, vol. 37, pp. 881–882, 1959.

[19] D. N. Astrov, "The magnetoelectric effect in antiferromagnetics," *Zh. Eksp. Teor. Fiz*, vol. 38, pp. 984–985, 1960.

[20] V. J. Folen, G. T. Rado, and E. W. Stalder, "Anisotropy of the magnetoelectric effect in cr_2o_3," *Phys. Rev. Lett.*, vol. 6, pp. 607–608, Jun 1961.

[21] H. Schmid, "Some symmetry aspects of ferroics and single phase multiferroics*," *Journal of Physics: Condensed Matter*, vol. 20, no. 43, p. 434201, 2008.

[22] T. H. O'Dell, *The electrodynamics of magneto-electric media*. North-Holland Amsterdam, 1970.

[23] J.-P. Rivera, "On definitions, units, measurements, tensor forms of the linear magneto-electric effect and on a new dynamic method applied to cr-cl boracite," *Ferroelectrics*, vol. 161, no. 1, pp. 165–180, 1994.

[24] E. Ascher and A. Janner, "Upper bounds on the magneto-electric susceptibility," *Physics Letters A*, vol. 29, no. 6, p. 295, 1969.

[25] E. Ascher, "Upper bounds for material coefficients," *Physics Letters A*, vol. 46, no. 2, p. 125, 1973.

[26] P. Borisov, A. Hochstrat, V. Shvartsman, and W. Kleemann, "Superconducting quantum interference device setup for magnetoelectric measurements," *Review of Scientific Instruments*, vol. 78, no. 10, pp. 106105–106105, 2007.

[27] T. Choi, Y. Horibe, H. Yi, Y. Choi, W. Wu, and S.-W. Cheong, "Insulating interlocked

ferroelectric and structural antiphase domain walls in multiferroic ymno3," *Nature materials*, vol. 9, no. 3, pp. 253–258, 2010.

[28] M. Fiebig, D. Fröhlich, K. Kohn, T. Lottermoser, V. Pavlov, R. Pisarev, *et al.*, "Determination of the magnetic symmetry of hexagonal manganites by second harmonic generation," *Physical review letters*, vol. 84, no. 24, p. 5620, 2000.

[29] D. Sa, R. Valenti, and C. Gros, "A generalized ginzburg-landau approach to second harmonic generation," *The European Physical Journal B-Condensed Matter and Complex Systems*, vol. 14, no. 2, pp. 301–305, 2000.

[30] T. Katsufuji, S. Mori, M. Masaki, Y. Moritomo, N. Yamamoto, and H. Takagi, "Dielectric and magnetic anomalies and spin frustration in hexagonal rmno3 (r= y, yb, and lu)," *Physical Review B*, vol. 64, no. 10, p. 104419, 2001.

[31] B. B. Van Aken, T. T. Palstra, A. Filippetti, and N. A. Spaldin, "The origin of ferroelectricity in magnetoelectric ymno3," *Nature materials*, vol. 3, no. 3, pp. 164–170, 2004.

[32] C. J. Fennie and K. M. Rabe, "Ferroelectric transition in ymno_{3} from first principles," *Physical Review B*, vol. 72, no. 10, p. 100103, 2005.

[33] S. Artyukhin, K. T. Delaney, N. A. Spaldin, and M. Mostovoy, "Landau theory of topological defects in multiferroic hexagonal manganites," *Nature Materials*, vol. 13, no. 1, pp. 42–49, 2014.

[34] E. Bertaut and M. Mercier, "Magnetic structure of mnyo$_3$," *Physics Letters*, vol. 5, no. 1, pp. 27–29, 1963.

[35] W. Koehler, H. Yakel, E. Wollan, and J. Cable, "A note on the magnetic structures of rare earth manganese oxides," *Physics Letters*, vol. 9, no. 2, pp. 93–95, 1964.

[36] X. Fabreges, I. Mirebeau, P. Bonville, S. Petit, G. Lebras-Jasmin, A. Forget, G. André, and S. Pailhes, "Magnetic order in ybmno3 studied by neutron diffraction and mössbauer spectroscopy," *Physical Review B*, vol. 78, no. 21, p. 214422, 2008.

[37] S. Nandi, A. Kreyssig, L. Tan, J. Kim, J. Yan, J. Lang, D. Haskel, R. McQueeney, and A. Goldman, "Nature of ho magnetism in multiferroic homno3," *Physical review letters*, vol. 100, no. 21, p. 217201, 2008.

[38] H. A. Salama and G. Stewart, "Exchange-induced tm magnetism in multiferroic h-tmmno3," *Journal of Physics: Condensed Matter*, vol. 21, no. 38, p. 386001, 2009.

[39] N. Fujimura, T. Ishida, T. Yoshimura, and T. Ito, "Epitaxially grown ymno3 film: New candidate for nonvolatile memory devices," *Applied physics letters*, vol. 69, no. 7, pp. 1011–1013, 1996.

[40] R. E. Cohen, "Origin of ferroelectricity in perovskite oxides," *Nature*, vol. 358, no. 6382, pp. 136–138, 1992.

[41] R. E. Cohen and H. Krakauer, "Electronic structure studies of the differences in ferroelectric behavior of batio3 and pbtio3," *Ferroelectrics*, vol. 136, no. 1, pp. 65–83, 1992.

[42] T. Katsufuji, M. Masaki, A. Machida, M. Moritomo, K. Kato, E. Nishibori, M. Takata, M. Sakata, K. Ohoyama, K. Kitazawa, *et al.*, "Crystal structure and magnetic properties of hexagonal rmno3 (r= y, lu, and sc) and the effect of doping," *Physical Review B*, vol. 66, no. 13, p. 134434, 2002.

[43] T. Lonkai, D. Tomuta, U. Amann, J. Ihringer, R. Hendrikx, D. Többens, and J. My-
dosh, "Development of the high-temperature phase of hexagonal manganites," *Phys-
ical Review B*, vol. 69, no. 13, p. 134108, 2004.

[44] K. Łukaszewicz and J. Karut-Kalicińska, "X-ray investigations of the crystal structure
and phase transitions of ymno3," *Ferroelectrics*, vol. 7, no. 1, pp. 81–82, 1974.

[45] M. Fiebig, T. Lottermoser, and R. Pisarev, "Spin-rotation phenomena and magnetic
phase diagrams of hexagonal rmno$_3$," *Journal of applied physics*, vol. 93, no. 10,
pp. 8194–8196, 2003.

[46] R. R. Birss *et al.*, *Symmetry and magnetism*, vol. 3. North-Holland Publishing Com-
pany Amsterdam, 1964.

[47] M. Fiebig, C. Degenhardt, and R. Pisarev, "Interaction of frustrated magnetic sub-
lattices in ermno3," *Physical review letters*, vol. 88, no. 2, p. 027203, 2001.

[48] Y. A. Izyumov, V. E. Naish, and R. P. Ozerov, *Neutron diffraction of magnetic ma-
terials*. Springer, 1991.

[49] F. Yen, C. d. Cruz, B. Lorenz, E. Galstyan, Y. Sun, M. Gospodinov, and C. Chu,
"Magnetic phase diagrams of multiferroic hexagonal rmno$_3$ (r= er, yb, tm, and ho),"
Journal of materials research, vol. 22, no. 8, p. 2163, 2007.

[50] B. Lorenz, A. Litvinchuk, M. Gospodinov, and C. Chu, "Field-induced reentrant novel
phase and a ferroelectric-magnetic order coupling in homno$_3$," *Physical review letters*,
vol. 92, no. 8, p. 087204, 2004.

[51] P. Sharma, J. Ahn, N. Hur, S. Park, S. B. Kim, S. Lee, J.-G. Park, S. Guha, and
S. Cheong, "Thermal conductivity of geometrically frustrated, ferroelectric ymno3:

Extraordinary spin-phonon interactions," *Physical review letters*, vol. 93, no. 17, p. 177202, 2004.

[52] C. Dela Cruz, F. Yen, B. Lorenz, Y. Wang, Y. Sun, M. Gospodinov, and C. Chu, "Strong spin-lattice coupling in multiferroic homno3: Thermal expansion anomalies and pressure effect," *Physical Review B*, vol. 71, no. 6, p. 060407, 2005.

[53] M. Fiebig, T. Lottermoser, D. Fröhlich, A. Goltsev, and R. Pisarev, "Observation of coupled magnetic and electric domains," *Nature*, vol. 419, no. 6909, pp. 818–820, 2002.

[54] N. A. Spaldin, M. Fiebig, and M. Mostovoy, "The toroidal moment in condensed-matter physics and its relation to the magnetoelectric effect," *Journal of Physics: Condensed Matter*, vol. 20, no. 43, p. 434203, 2008.

[55] H. Das, A. L. Wysocki, Y. Geng, W. Wu, and C. J. Fennie, "Bulk magnetoelectricity in the hexagonal manganites and ferrites," *Nature communications*, vol. 5, 2014.

[56] Y. Kumagai and N. A. Spaldin, "Structural domain walls in polar hexagonal manganites," *Nature communications*, vol. 4, p. 1540, 2013.

[57] T. JUNGK, A. HOFFMANN, M. FIEBIG, and E. SOERGEL, "Electrostatic topology of ferroelectric domains in ymno3," *Applied physics letters*, vol. 97, no. 1, 2010.

[58] Y. Yu, X. Zhang, Y. Zhao, N. Jiang, R. Yu, J. Wang, C. Fan, X. Sun, and J. Zhu, "Atomic-scale study of topological vortex-like domain pattern in multiferroic hexagonal manganites," *Applied Physics Letters*, vol. 103, no. 3, p. 032901, 2013.

[59] S. Chae, Y. Horibe, D. Jeong, S. Rodan, N. Lee, and S.-W. Cheong, "Self-organization,

condensation, and annihilation of topological vortices and antivortices in a multiferroic," *Proceedings of the National Academy of Sciences*, vol. 107, no. 50, pp. 21366–21370, 2010.

[60] W. Wu, Y. Horibe, N. Lee, S.-W. Cheong, and J. Guest, "Conduction of topologically protected charged ferroelectric domain walls," *Physical review letters*, vol. 108, no. 7, p. 077203, 2012.

[61] D. Meier, J. Seidel, A. Cano, K. Delaney, Y. Kumagai, M. Mostovoy, N. A. Spaldin, R. Ramesh, and M. Fiebig, "Anisotropic conductance at improper ferroelectric domain walls," *Nature materials*, vol. 11, no. 4, pp. 284–288, 2012.

[62] G. Binnig, H. Rohrer, C. Gerber, and E. Weibel, "Surface studies by scanning tunneling microscopy," *Physical review letters*, vol. 49, no. 1, p. 57, 1982.

[63] G. K. Bennig, "Atomic force microscope and method for imaging surfaces with atomic resolution," Feb. 9 1988. US Patent 4,724,318.

[64] H. Takahashi, K. Ando, and Y. Shirakawabe, "Self-sensing piezoresistive cantilever and its magnetic force microscopy applications," *Ultramicroscopy*, vol. 91, no. 1, pp. 63–72, 2002.

[65] D. Rugar, H. Mamin, P. Guethner, S. Lambert, J. Stern, I. McFadyen, and T. Yogi, "Magnetic force microscopy: General principles and application to longitudinal recording media," *Journal of Applied Physics*, vol. 68, no. 3, pp. 1169–1183, 1990.

[66] A. Wadas and H. Hug, "Models for the stray field from magnetic tips used in magnetic force microscopy," *Journal of applied physics*, vol. 72, no. 1, pp. 203–206, 1992.

[67] H. J. Hug, B. Stiefel, P. Van Schendel, A. Moser, R. Hofer, S. Martin, H.-J. Güntherodt, S. Porthun, L. Abelmann, J. Lodder, *et al.*, "Quantitative magnetic force microscopy on perpendicularly magnetized samples," *Journal of Applied Physics*, vol. 83, no. 11, pp. 5609–5620, 1998.

[68] T. Albrecht, P. Grütter, D. Horne, and D. Rugar, "Frequency modulation detection using high-q cantilevers for enhanced force microscope sensitivity," *Journal of Applied Physics*, vol. 69, no. 2, pp. 668–673, 1991.

[69] A. Volodin, K. Temst, C. Van Haesendonck, and Y. Bruynseraede, "Low temperature magnetic force microscopy with enhanced sensitivity based on piezoresistive detection," *Review of Scientific Instruments*, vol. 71, no. 12, pp. 4468–4473, 2000.

[70] Y. Geng, J. Lee, D. Schlom, J. Freeland, and W. Wu, "Magnetic inhomogeneity in a multiferroic eutio_{3} thin film," *Physical Review B*, vol. 87, no. 12, p. 121109, 2013.

[71] Y. Geng and W. Wu, "Magnetoelectric force microscopy based on magnetic force microscopy with modulated electric field," *Review of Scientific Instruments*, vol. 85, no. 5, p. 053901, 2014.

[72] T.-K. Chung, G. P. Carman, and K. P. Mohanchandra, "Reversible magnetic domain-wall motion under an electric field in a magnetoelectric thin film," *Applied Physics Letters*, vol. 92, no. 11, p. 112509, 2008.

[73] Y. Tokunaga, S. Iguchi, T. Arima, and Y. Tokura, "Magnetic-field-induced ferroelectric state in dyfeo_{3}," *Physical review letters*, vol. 101, no. 9, p. 097205, 2008.

[74] Y. Geng, H. Das, A. L. Wysocki, X. Wang, S. Cheong, M. Mostovoy, C. J. Fennie, and W. Wu, "Direct visualization of magnetoelectric domains," *Nature materials*, 2013.

[75] Y. Obukhov, K. Fong, D. Daughton, and P. Hammel, "Real time cantilever signal frequency determination using digital signal processing," *Journal of applied physics*, vol. 101, no. 3, pp. 034315–034315, 2007.

[76] E. Morosan, H. Zandbergen, L. Li, M. Lee, J. Checkelsky, M. Heinrich, T. Siegrist, N. P. Ong, and R. Cava, "Sharp switching of the magnetization in fe1/4tas2," *Physical Review B*, vol. 75, no. 10, p. 104401, 2007.

[77] Y. Choi, S. Kim, T. Asada, S. Park, W. Wu, Y. Horibe, and S. Cheong, "Giant magnetic coercivity and ionic superlattice nano-domains in fe0.25tas2," *EPL (Europhysics Letters)*, vol. 86, no. 3, p. 37012, 2009.

[78] Y. Geng, N. Lee, Y. Choi, S.-W. Cheong, and W. Wu, "Collective magnetism at multiferroic vortex domain walls," *Nano letters*, vol. 12, no. 12, pp. 6055–6059, 2012.

[79] P. M. Chaikin and T. C. Lubensky, *Principles of condensed matter physics*, vol. 1. Cambridge Univ Press, 2000.

[80] X. Yu, Y. Onose, N. Kanazawa, J. Park, J. Han, Y. Matsui, N. Nagaosa, and Y. Tokura, "Real-space observation of a two-dimensional skyrmion crystal," *Nature*, vol. 465, no. 7300, pp. 901–904, 2010.

[81] Q. Zhang, L. Wang, X. Wei, R. Yu, L. Gu, A. Hirata, M. Chen, C. Jin, Y. Yao, Y. Wang, *et al.*, "Direct observation of interlocked domain walls in hexagonal rmno3 (r= tm, lu)," *Physical Review B*, vol. 85, no. 2, p. 020102, 2012.

[82] A. Scholl, J. Stöhr, J. Lüning, J. W. Seo, J. Fompeyrine, H. Siegwart, J.-P. Locquet, F. Nolting, S. Anders, E. Fullerton, *et al.*, "Observation of antiferromagnetic domains in epitaxial thin films," *Science*, vol. 287, no. 5455, pp. 1014–1016, 2000.

[83] P. G. Evans, E. D. Isaacs, G. Aeppli, Z. Cai, and B. Lai, "X-ray microdiffraction images of antiferromagnetic domain evolution in chromium," *Science*, vol. 295, no. 5557, pp. 1042–1045, 2002.

[84] M. Bode, E. Vedmedenko, K. Von Bergmann, A. Kubetzka, P. Ferriani, S. Heinze, and R. Wiesendanger, "Atomic spin structure of antiferromagnetic domain walls," *Nature materials*, vol. 5, no. 6, pp. 477–481, 2006.

[85] U. Hartmann, "Magnetic force microscopy," *Annual review of materials science*, vol. 29, no. 1, pp. 53–87, 1999.

[86] I. Schmid, M. Marioni, P. Kappenberger, S. Romer, M. Parlinska-Wojtan, H. Hug, O. Hellwig, M. Carey, and E. Fullerton, "Exchange bias and domain evolution at 10 nm scales," *Physical review letters*, vol. 105, no. 19, p. 197201, 2010.

[87] T. Lonkai, D. Hohlwein, J. Ihringer, and W. Prandl, "The magnetic structures of ymno3-δ and homno3," *Applied Physics A*, vol. 74, no. 1, pp. s843–s845, 2002.

[88] I. Dzyaloshinskii, "On the magneto-electrical effect in antiferromagnets," 1960.

[89] T. Moriya, "Anisotropic superexchange interaction and weak ferromagnetism," *Physical Review*, vol. 120, no. 1, p. 91, 1960.

[90] I. Munawar and S. Curnoe, "Theory of magnetic phases of hexagonal rare earth manganites," *Journal of Physics: Condensed Matter*, vol. 18, no. 42, p. 9575, 2006.

[91] A. M. Essin, J. E. Moore, and D. Vanderbilt, "Magnetoelectric polarizability and axion electrodynamics in crystalline insulators," *Physical review letters*, vol. 102, no. 14, p. 146805, 2009.

[92] X.-L. Qi and S.-C. Zhang, "Topological insulators and superconductors," *Reviews of Modern Physics*, vol. 83, no. 4, p. 1057, 2011.

[93] H. Sugie, N. Iwata, and K. Kohn, "Magnetic ordering of rare earth ions and magnetic-electric interaction of hexagonal rmno3 (r= ho, er, yb or lu)," *Journal of the Physical Society of Japan*, vol. 71, no. 6, pp. 1558–1564, 2002.

[94] T. Jungk, Á. Hoffmann, and E. Soergel, "Challenges for the determination of piezo-electric constants with piezoresponse force microscopy," *Applied Physics Letters*, vol. 91, no. 25, p. 253511, 2007.

[95] D. Meier, H. Ryll, K. Kiefer, B. Klemke, J.-U. Hoffmann, R. Ramesh, and M. Fiebig, "Mutual induction of magnetic 3d and 4f order in multiferroic hexagonal ermno3," *Physical Review B*, vol. 86, no. 18, p. 184415, 2012.

[96] S. Seki, S. Ishiwata, and Y. Tokura, "Magnetoelectric nature of skyrmions in a chiral magnetic insulator cu2oseo3," *Physical Review B*, vol. 86, no. 6, p. 060403, 2012.

[97] C.-Z. Chang, J. Zhang, X. Feng, J. Shen, Z. Zhang, M. Guo, K. Li, Y. Ou, P. Wei, L.-L. Wang, *et al.*, "Experimental observation of the quantum anomalous hall effect in a magnetic topological insulator," *Science*, vol. 340, no. 6129, pp. 167–170, 2013.

[98] Y. Tokura, "Multiferroics as quantum electromagnets," *Science*, vol. 5779, p. 1481, 2006.

[99] W. Wang, J. Zhao, W. Wang, Z. Gai, N. Balke, M. Chi, H. N. Lee, W. Tian, L. Zhu, X. Cheng, *et al.*, "Room-temperature multiferroic hexagonal lufeo3 films," *Physical Review Letters*, vol. 110, no. 23, p. 237601, 2013.

[100] J. H. Lee, L. Fang, E. Vlahos, X. Ke, Y. W. Jung, L. F. Kourkoutis, J.-W. Kim, P. J. Ryan, T. Heeg, M. Roeckerath, *et al.*, "A strong ferroelectric ferromagnet created by means of spin-lattice coupling," *Nature*, vol. 466, no. 7309, pp. 954–958, 2010.

[101] J. W. Kim, S. Haam, Y. Oh, S. Park, S.-W. Cheong, P. Sharma, M. Jaime, N. Harrison, J. H. Han, G.-S. Jeon, *et al.*, "Observation of a multiferroic critical end point," *Proceedings of the National Academy of Sciences*, vol. 106, no. 37, pp. 15573–15576, 2009.

Appendix A

Technique details of Landau theory

At low temperature limit, i.e., $T \ll T_\mathrm{N}$. Use rigid spin approximation, i.e., ignore amplitude fluctuation. The Landau free energy of Mn and RE spins is :

$$f = f^\mathrm{Mn} + f^\mathrm{RE} \tag{A.1}$$

Considering the Mn ordering in $P6_3cm$ (polar) structure,

$$f^\mathrm{Mn} = (C_{11}+D_{11}E)LH+(C_{20}+D_{20}E)L^2+(C_{02}+D_{02}E)H^2+(C_{22}+D_{22}E)L^2H^2+C_{40}L^4+... \tag{A.2}$$

Here $L = L_{\mathrm{A}_2} = \sin\psi$ ($L_{\mathrm{B}_2} = \cos\psi$) is the Mn spin orientation order parameter in A_2 (B_2) phase. For RE magnetism, we only consider the 4b sites. The RE spins are Ising-like (anisotropy), with the moment $\mu^\mathrm{RE} = gJ\mu_\mathrm{B}$, where $g = g^0 + g^1 E_z$ is the $g-$factor of RE spins, and g^1 describes the linear electric field dependence of the $g-$factor at the 4b sites of $P6_3cm$ structure. Therefore the Zeeman energy of RE moment is

$$\varepsilon^\mathrm{RE} = -\mu^\mathrm{RE}H_z = -(g^0 + g^1 E_z)J\mu_\mathrm{B}H_z = -(\mu + \alpha E_z)H_z \tag{A.3}$$

where $\mu = g^0 J\mu_B$ is the RE moment and $\alpha = g^1 J\mu_B$ is the electric field dependence of RE moments due to E_z dependence $g-$factor, which leads to macroscopic magnetoelectric effect α^RE.

The Hamiltonian of RE spins at 4b sites $(\sigma_1, \sigma_2, \sigma_3, \sigma_4)$ in the exchange field of Mn^{3+} order is:

$$\mathcal{H}^\mathrm{RE} = -g_1 \cos\psi(\sigma_1 - \sigma_2 + \sigma_3 - \sigma_4) - g_2 \sin\psi(\sigma_1 + \sigma_2 + \sigma_3 + \sigma_4)-$$

$$(\mu + \alpha E_z)H_z(\sigma_1 + \sigma_2 + \sigma_3 + \sigma_4) \tag{A.4}$$

Here σ_i is Ising spins with values ± 1. The g_1 (g_2) term describes the RE-Mn coupling in B_2 (A_2) phase. The last term is the Zeeman coupling with magnetic moment dependent on E_z. Here the Hamiltonian can be expressed as a sum of those of individual spins $\mathcal{H}^{\mathrm{RE}} = \sum_i \mathcal{H}_i^{\mathrm{RE}}$.

The partition function of RE moments (at 4b sites) is:

$$\mathcal{Z}^{\mathrm{RE}} \;=\; e^{-\beta f^{\mathrm{RE}}} = \sum_{\{\sigma_i\}} e^{-\beta \mathcal{H}^{\mathrm{RE}}} = \prod_i \sum_{\sigma_i} e^{-\beta \mathcal{H}_i^{\mathrm{RE}}} = \prod_i \cosh(\beta h_i)$$

Note that spin 1 and 3 (2 and 4) are identical, so their partition functions is identical. Therefore,

$$\mathcal{Z}^{\mathrm{RE}} = 16[\cosh^2(\beta h_1) \cdot \cosh^2(\beta h_2)] \tag{A.5}$$

Here

$$\begin{cases} h_1 & = g_1 \cos\psi + g_2 \sin\psi + (\mu + \alpha E_z)H_z = g\sin(\psi + \delta) + (\mu + \alpha E_z)H_z \\[2mm] h_2 & = -g_1 \cos\psi + g_2 \sin\psi + (\mu + \alpha E_z)H_z = g\sin(\psi - \delta) + (\mu + \alpha E_z)H_z \end{cases}$$

with $g = \sqrt{g_1^2 + g_2^2}$ and $\tan\delta = g_1/g_2$ to simplify the notation. $g_1 = g\sin\delta$, $g_2 = g\cos\delta$. Therefore, the free energy of RE moments is

$$f^{\mathrm{RE}} = -\frac{1}{\beta}\ln Z^{\mathrm{RE}} = -\frac{2}{\beta}[\ln\cosh(\beta h_1) + \ln\cosh(\beta h_2)] - \frac{4\ln 2}{\beta} \tag{A.6}$$

Combining Eq. A.2 and A.6, the full Landau free energy expansion can be obtained.

The total magnetoelectric effect:

$$\alpha_{zz} = \frac{\partial M_z}{\partial E_z} = \alpha_{zz}^{\mathrm{Mn}} + \alpha_{zz}^{\mathrm{RE}} \tag{A.7}$$

$$\alpha_{zz}^{\mathrm{Mn}} = \frac{\partial M_z^{\mathrm{Mn}}}{\partial H_z} = -\frac{\partial^2 f^{\mathrm{Mn}}}{\partial E_z \partial H_z} - \frac{\partial^2 f^{\mathrm{Mn}}}{\partial E_z \partial \psi} \cdot \frac{d\psi}{dH_z} \tag{A.8}$$

in which, the second term considers nonrigid Mn^{3+} spin rotations, and from Eq. A.2

$$\begin{aligned} \frac{\partial^2 f^{\mathrm{Mn}}}{\partial E_z \partial H_z} &= D_{11}L + 2D_{20}H + 2D_{22}EL^2H \\[2mm] \frac{\partial^2 f^{\mathrm{Mn}}}{\partial E_z \partial \psi} &= -\frac{\partial^2 f^{\mathrm{Mn}}}{\partial E_z \partial L} \cdot \frac{dL}{d\psi} = (D_{11}H + 2D_{22}LH^2)\cos\psi \end{aligned}$$

use the chain rule to evaluate $d\psi/dH_z$

$$\frac{d\psi}{dH_z} = -\frac{\dfrac{\partial^2 f}{\partial \psi \partial H_z}}{\dfrac{\partial^2 f}{\partial \psi^2}} = -\frac{\dfrac{\partial^2 (f^{\mathrm{RE}} + f^{\mathrm{Mn}})}{\partial \psi \partial H_z}}{\dfrac{\partial^2 (f^{\mathrm{RE}} + f^{\mathrm{Mn}})}{\partial \psi^2}} \tag{A.9}$$

explicitly,

$$\frac{\partial^2 f^{\text{Mn}}}{\partial H_z \partial \psi} = -\frac{\partial^2 f^{\text{Mn}}}{\partial H_z \partial L} \cdot \frac{dL}{d\psi} = [C_{11} + D_{11}E + 4(C_{22} + D_{22}E)LH]\cos\psi \tag{A.10}$$

$$\begin{aligned}
\frac{\partial^2 f^{\text{Mn}}}{\partial \psi^2} &= \frac{\partial^2 f^{\text{Mn}}}{\partial L^2}(1 - L^2) - \frac{\partial f^{\text{Mn}}}{\partial L}\cos\psi \\
&= [2(C_{20} + D_{20}E) + 2(C_{22} + D_{22}E)H^2 + 12C_{40}L^2](1 - L^2) \\
&\quad - [(C_{11} + D_{11}E) + 2(C_{20} + D_{20}E)L + 2(C_{22} + D_{22}E)LH^2 + 4C_{40}L^3]\cos\psi
\end{aligned}$$

and,

$$\frac{\partial f^{\text{RE}}}{\partial \psi} = -2g[\tanh(\beta h_1)\cos(\psi + \delta) + \tanh(\beta h_2)\cos(\psi - \delta)] \tag{A.11}$$

$$\frac{\partial^2 f^{\text{RE}}}{\partial \psi^2} = 2g\{[\tanh(\beta h_1)\sin(\psi + \delta) + \tanh(\beta h_2)\sin(\psi - \delta)]-$$

$$\beta g[\text{sech}^2(\beta h_1)\cos^2(\psi + \delta) + \text{sech}^2(\beta h_2)\cos^2(\psi - \delta)]\} \tag{A.12}$$

$$\frac{\partial^2 f^{\text{RE}}}{\partial H_z \partial \psi} = -\frac{\partial M_z^{\text{RE}}}{\partial \psi} = -2(\mu + \alpha E)^2\beta g[\text{sech}^2(\beta h_1)\cos(\psi + \delta) + \text{sech}^2(\beta h_2)\cos(\psi - \delta)] \tag{A.13}$$

The second term in Eq. A.8 is responsible for the anomalous ME responsible, which is discussed in Sec. 4.3.3 as well. Apparently, the denominator of Eq. A.9 approaches to zero as the spin rotation angle $\psi \to 90^{\text{o}}$, causing the divergence of α_{zz}^{Mn}.

To evaluate α_{zz}^{RE}, the RE magnetic moment and polarization are calculated based on the RE free energy Eq. A.6:

$$M_z^{\text{RE}} = -\frac{\partial f^{\text{RE}}}{\partial H_z} = 2(\mu + \alpha E_z)[\tanh(\beta h_1) + \tanh(\beta h_2)] = \frac{\mu + \alpha E_z}{\alpha H_z}P_z^{\text{RE}} \tag{A.14}$$

$$P_z^{\text{RE}} = -\frac{\partial f^{\text{RE}}}{\partial E_z} = 2\alpha H_z[\tanh(\beta h_1) + \tanh(\beta h_2)] = \frac{\alpha}{\mu + \alpha E_z}M_z^{\text{RE}}H_z \tag{A.15}$$

Note that this value has to be divided by 4 to get the proper magnetization (in the unit of μ_{B}/f.u.). Therefore, the magnetoelectric effects due to RE moments:

$$\alpha_{zz}^{\text{RE}} = \frac{dP_z^{\text{RE}}}{dH_z} = \frac{\alpha}{\mu + \alpha E_z} \cdot \left(M_z^{\text{RE}} + H_z\frac{dM_z^{\text{RE}}}{dH_z}\right) \tag{A.16}$$

The susceptibility of RE moments is:

$$\frac{dM^{\mathrm{RE}}}{dH_z} = \frac{\partial M^{\mathrm{RE}}}{\partial H_z} + \frac{\partial M^{\mathrm{RE}}}{\partial \psi} \cdot \frac{d\psi}{dH_z} \tag{A.17}$$

$$\frac{\partial M^{\mathrm{RE}}}{\partial H_z} = 2(\mu + \alpha E)^2 \beta [\mathrm{sech}^2(\beta h_1) + \mathrm{sech}^2(\beta h_2)] \tag{A.18}$$